Advanced Germanium Devices for Optical Interconnects

Geavanceerde componenten in germanium voor optische interconnecties

Srinivasan Ashwyn Srinivasan

Promotoren: prof. dr. ir. D. Van Thourhout, dr. ir. J. Van Campenhout
Proefschrift ingediend tot het behalen van de graad van
Doctor in de ingenieurswetenschappen: fotonica

Vakgroep Informatietechnologie
Voorzitter: prof. dr. ir. B. Dhoedt
Faculteit Ingenieurswetenschappen en Architectuur
Academiejaar 2017 - 2018

UNIVERSITEIT
GENT

ISBN 978-94-6355-103-8
NUR 926, 965
Wettelijk depot: D/2018/10.500/21

UNIVERSITEIT
GENT

Promotoren:
Prof. Dr. Ir. Dries Van Thourhout
Dr. Ir. Joris Van Campenhout

Examencommissie:

Em. Prof. Dr. Ir. Daniel De Zutter (Voorzitter)	Universiteit Gent
Prof. Dr. Ir. Dries Van Thourhout (Promoter)	Universiteit Gent
Dr. Ir. Joris Van Campenhout (Promoter)	imec
Dr. Hans Sigg	Paul Scherrer Institut
Prof. Dr. Delphine Marris-Morini	University of Paris-Sud
Prof. Dr. Ir. Günther Roelkens	Universiteit Gent
Prof. Dr. Ir. Geert Morthier	Universiteit Gent
Prof. Dr. Ir. Henk Vrielinck	Universiteit Gent
Dr. Ir. Pieter Geiregat	Universiteit Gent

Universiteit Gent
Faculteit Ingenieurswetenschappen en Architectuur

Vakgroep Informatietechnologie
Technologiepark-Zwijnaarde 15 iGent, B-9052 Gent, Belgium

Tel.: +32-9-264.33.16
Fax.: +32-9-264.35.93

Acknowledgements

"A well formed mind; one that reacts to unfamiliar facts, situations and details, which could actually process information that it hasn't studied or heard of before. A mind in other words that can react to the bigger examination called life which doesn't exactly give you things you prepared for. We need to think out of the box, think of familiar objects in ways we haven't before and that's the only way we can move forward in the world." - Dr. Shashi Tharoor

Since my childhood days up until my master thesis, my academic journey had taught me that the ideal environment where a student can be transformed into a researcher is where there is a confluence of access to knowledge, state of the art resources and the support to experiment with them both. I am happy to have had access to such a playground during the course of my PhD and this would not have been possible without my supervisor: Dries Van Thourhout and my daily advisor: Joris Van Campenhout. They have taught me how to identify the subtle line that separates a pragmatic (more industrial) and a theoretical (more academic) way of working and to balance my work ethic without compromising on either of the two. I would also like to thank Marianna Pantouvaki from imec who has followed my work closely and has always supported me throughout my PhD. At this point, I would also like to mention all my colleagues at the Photonics Research Group, at the ID labs from University of Ghent and at imec's Optical IO, Group IV Epitaxy, System and REMO team. Their depth of knowledge, skill set and the multidisciplinary mind set in its true form has been truly inspiring. But among them, special thanks goes to Clement Porret, Pieter Geiregat, Yosuke Shimura, Guy Lepage, Peter Verheyen, Yoojin, Peter De Heyn, Jochem Verbist, Ewoud Vissers, Daire Cott, Roger Loo, Ashwini Prabhulinga, Rajrupa Paul and Sakshi Anand, with whom I have worked closely. Without any of their expertise, support and critical discussions, none of the work presented in this thesis would have materialized. Brad Snyder, Nivesh Mangal, Chiara Alessandri, Irina Kulkova, Sadhish Balakrishnan, Samiul Hasan, Sebatien Lardenois, Jeroen De Coster, Sofie Jansen, Yuting Shi, Zhechao Wang, Bart Kuyken, Bin Tian, Raphael Van Laer, Michal Rakowski, Aditya Malik, Utsav Dave and Yunpeng Zhu have all also been been great coworkers and always been helpful in the clean room, at OIO or UGent labs or with imecinone.

This now brings me to everyone who have been an integral part of my personal life during my stay in Belgium. Without them my life would not have been enjoyable as it is now. The list of people is definitely enormously long, this might be because 4 years and 5 months has been the longest time that I have stayed in one place for the past 11 years, and it happens that they all belong to certain groups of my PhD/Belgium life. So I will start with the groups from imec/UGent and continue with groups that have no connections with imec/UGent.

- *Sunday fun-day* - Alicja, Rafal, Shruti, Vito, Ketty, Sid, Shreya, Attilio, Ferenc: The main activity of this group was to go for long hikes/walks (basically any form of exercises) that we can do in the Heverlee forest every Sunday (hence the name Sunday fun day). But we end up doing everything but walks and hikes. That includes Catan, Pieroggi, and a number of dinners and travels around Belgium/Europe. This is also the group that has been able to tolerate all my Indian-French and lately my Indian-Dutch as well.

- *AruQ* - Attilio, Gabriele, Sarah, Vito, Davide, Oreste, Alessandro, Marcello: The group with whom I lunched at imec cafeteria, played squash and soccer. They have taught me how to complain like an Italian, how to loose bets in soccer and most importantly - never miss an espresso after lunch (even though I could never find my Ristretto Indiano). In return I managed to teach them some of my Indian-Italian and I promise at some point we will end up conversing in our Indian-Italian (Ofo-courseo).

- *Ssup* - Sid, Shreya, Adil, Rahila, Abhinav, Ankit, Poulomi, Yashwanth, Vignesh: Also known as *MWC (mid week chill).* That's right: we meet up mid-week in the evening and enjoy some great Indian food and talk about Global and Indian politics. Well it is never boring since they always end up adding some form of humor in the discussion such that our curiosity never slips off.

- *AA club* - Chiara, Sofie, Vamsi, Bart, Waldo: Game of thrones, Harry Potter, Star Wars, Lord of the rings? Am I still missing anything? Name it and you can have unlimited discussions here. I have gathered fond memories with them including the failed ski-trip.

- *Look at the sky* - Marcello, Marieke, Alessandro, Wouter, Sabrina, Christina, Mark, Johnathan, Salvo, Marjolein, Laura: A group formed from a BDay trip to Madrid, it was initially called *Look at the guy* - but *Look at the sky* makes it more gender neutral. Most of the times our conversations revolve around football - specifically to tease Arsenal: Wouter and Inter-Milan: Ale, but we basically do every social activity you can think of except having Fondue.

- *Slok* - An, Federica, Bruno, Bram, Dries, Sofie, Sarah, Jef: A healthy mind needs a healthy body. For a healthy body, I need *Slok* for our every Tuesday runs at Heverleebos. Best way to burst your stress bubble with some good Belgian company and Belgian woods.

- *Tamil club* - Prashant, Anitha, Sadhish, Divya: I have enjoyed watching Tamil movies and having proper South Indian food with them. Their company always remind me of my roots.

- *Marathon group* - Ken, Pete: My half and full marathon running mates from London. I happened to meet them in a running event at Copenhagen, 2015 and since then, we have done Lisbon, Munich, Berlin, Palma de Mallorca and Athens half marathon/full marathon that I have enjoyed a lot with their company.

The list can never end without thanking the people closest to me in my life. I have always received unconditional support in every ups and downs moment of my PhD life, for which, I am extremely thankful to Eva. Hari and Perima have been extremely supportive in Leuven for the first 3 years of my PhD, and I have missed our long chats ever since they left Belgium. I have always considered them as my second family. But most importantly, I would like to thank Mom, Dad and Hanu for everything they have given me right from my childhood up until the completion of my student life with this PhD. This journey would not have been possible without them.

Gent and Leuven, November 2013 - April 2018
Srinivasan Ashwyn Srinivasan

Table of Contents

List of Figures

List of Tables

List of Acronyms

A

Al	Aluminium
AOC	Active Optical Cables
As	Arsenic

C

CMP	Chemical Mechanical Polishing
CW	Continuous Wave
CMOS	Complementary Metal Oxide Semiconductor
CWDM	Coarse Wavelength Division Multiplexing

D

DAC	Digital to Analog Converter
DUT	Device Under Test
DWDM	Dense Wavelength Division Multiplexing

E

EAM	Electro Absorption Modulator
ECCI	Electron Channeling Contrast Imaging
ER	Extinction Ratio
E-Field	Electric Field

F

FKE	Franz Keldysh Effect
FOM	Figure of Merit
FEM	Finite Element Method
FWHM	Full Width of Half Maxima
FFE	Feed forward equalization

G

Ge	Germanium
Ga	Ga
GIB	Ge ion bombardment

H

HD-FEC	Hard Decision Forward Error Correction

I

IC	Integrated Circuit
In	Indium
I/O	Input Output
IL	Insertion Loss
IV	Current Voltage
IHP	Innovation for High Performance Microelectronics
IRF	Instrument Response Function

J

JDOS	Joint Density of States

M

MHE	Micro Hall Experiment
MMI	Multi Mode Fiber
MQW	Multi Quantum Well
MIT	Massachusetts Institute of Technology
MZI	Mach Zehnder interferometer
MCF	Multi Core Fiber

N

NRZ	Non Return to Zero

O

OOK	On Off Keying

P

ppPH3	partial pressure of PH_3 gas
ppGe2H6	partial pressure of Ge_2H_6 gas
PAM	Pulse Amplitude Modulation
P	Phosphorus
PL	Photoluminescence
PPS	Pump Probe Spectroscopy
PD	Photodiode
PRBS	Pseudorandom Binary Sequence
PSM	Parallel Single Mode Fiber

Q

Q	Quality factor
QW	Quantum Well
QCSE	Quantum Confined Stark Effect
QSFP	Quad Small Form factor Pluggable

R

RC	Resistance Capacitance
RBS	Rutherfold Back Scattering
RTA	Rapid Thermal Anneal
RSM	Reciprocal Space Map
RF	Radio Frequency
RX	Receiver

S

Sb	Antimony
Si	Silicon
SEM	Scanning Electron Microscopy
SMF	Single Mode Fiber
SIMS	Secondary Ion Mass Spectroscopy
SOI	Silicon on Insulator
SDM	Space Division Multiplexing

T

TAS	Transient Absorption Spectroscopy
TEM	Transmission Electron Microscopy
TCAD	Technology Computer Aided Design
TDD	Threading Dislocation Density
TOR	Top of the Rack
TRPL	Time Resolved Photoluminescence
TX	Transmitter

U

UK	United Kingdom

V

Vpp	Volt peak to peak
VCSEL	Vertical-Cavity Surface-Emitting Laser

W

WG	Waveguide
WDM	Wavelength Division Multiplexing

X

XRD	X-Ray Diffraction

Z

ZB	Zetabyte

Nederlandse samenvatting –Summary in Dutch–

“Wetenschap is het geloof in de onwetendheid van experts ..... Het is onze verantwoordelijkheid als wetenschappers, die de grote vooruitgang en grote waarde kennen van een bevredigende filosofie van onwetendheid, de grote vooruitgang die de vrucht is van de vrijheid van denken, om de waarde van deze vrijheid, om te leren hoe twijfel niet moet worden gevreesd maar verwelkomd en besproken, en om deze vrijheid te eisen als onze plicht tegenover alle komende generaties.” - Richard P. Feynman

De moderne levensstijl is sterk afhankelijk van het internet. Het vormt de ruggengraat voor videotoepassingen, spraakherkenning, dataverwerking, zoekmachines, sociale netwerken en cloud computing . Al deze toepassingen zijn erg reken- en data-intensief en gebruiken het internet als centrale opslag- en verwerkingseenheid. In zijn Global Cloud Index Forecast and Methodology Report voor 2015-2020 voorspelt Cisco dat dit zal resulteren in een wereldwijde toename van het IP-verkeer van 4,7 ZB in 2015 naar 15,3 ZB tegen het einde van 2020, waarbij 92% van het totale verkeer zal worden afgehandeld door datacentra gefocusseerd op cloud computing. Om dit ecosysteem economisch en ecologisch in stand te kunnen houden, moeten de interconnecties tussen de servers van het datacenter schaling van de communicatiebandbreedte mogelijk maken, zonder het vermogenverbruik te laten exploderen. Problematisch daarbij is dat het aantal pinnen op de processoren die instaan voor de dataverwerking niet aan dezelfde snelheid schaalt als de globale I/O eisen. Dit resulteert in de noodzaak om de datasnelheid in elk kanaal (elke I/O-pen) te verhogen, maar vanwege fundamentele fysieke beperkingen zijn elektrische interconnecties beperkt in bandbreedte. Optische interconnecties worden sinds lang beschouwd als een alternatief voor deze elektrische interconnecties. Silicium fotonica krijgt daarbij steeds meer belang voor de realisatie van de benodigde zender en ontvanger systemen, de zogenaamde tranceivers. Een van de uitdagingen is echter het gebrek aan monolithisch geïntegreerde lasers in dit platform. Inspanningen om lichtbronnen en andere componenten zoals elektro-absorptiemodulatoren te realiseren binnen dit platform vereisen ofwel de monolithische groei van nieuwe materialen op silicium, ofwel heterogene integratie van III-V-lagen door waferbonding of zelfs extern geïntegreerde componenten. Maar hier zijn verschillende uitdagingen aan verbonden: een complexe processing, een hoge integratiekost, gebrek aan schaalbaarheid en/of een gebrekkige koppeling naar silicium golfgeleiders. Germanium (Ge) aan de andere kant kan eenvoudig worden gentegreerd in een bestaand silicium platform, zoals uitgebreid werd aangetoond voor de realisatie van fotodetectoren. Gezien de aanwezigheid van een directe bandgap bij 0,8 eV (1550 nm) is Ge bovendien een goede kandidaat om laserbronnen en elektroabsorptiemodulatoren te realiseren in golflengtegebieden die relevant zijn voor datacom- en telecomtoepassingen. Daarom wordt in dit proefschrift een uitgebreide studie gepresenteerd waarin we evalueren of Ge-gebaseerde lasers en elektroabsorptiemodulatoren technologisch compatibel kunnen zijn met toekomstige optische interconnectietoepassingen.

Net als Si is Ge intrinsiek een materiaal met een indirecte bandgap en dus een inefficiënte lichtbron. De mate van indirectheid in Ge is echter veel kleiner dan bij Si. Als gevolg daarvan kan de bandgap van Germanium pseudo direct of zelfs volledig direct worden gemaakt, hetzij door het toevoegen van n-type dopanten (om een pseudo directe bandgap te creren), hetzij door het introduceren van uniaxiale/biaxiale trekspanning, of het te legeren met tin (Sn) (om het een materiaal met een directe band gap te maken). Introduceren van trekspanning of legeren met Sn resulteert echter in lichtgeneratie met een golflengte groter dan 2000 nm. Dergelijke golflengtes hebben last van grote chromatische dispersie in conventionele glasvezelkabels en ondersteunen daarom geen signalen met hoge snelheid over afstanden die relevant zijn in een datacenter. Creatie van een pseudo directe band gap in Ge door n-type dopering daarentegen maakt lichtemissie bij golflengtes kleiner dan 1700 nm mogelijk en is als dusdanig relevanter voor optisch interconnecties. Daarom werd in dit proefschrift n-type gedoteerd Ge geïdentificeerd als de meest relevante route voor de realisatie van een elektrisch gepompte laser die opereert bij een golflengte $<$ 1700 nm. We stelden daarbij initieel een drempelstroom van 10 kA/cm^2 als doelstelling. Dit is een verbetering met een factor 30 in vergelijking met eerder gedemonstreerde elektrisch gepompte Ge lasers, maar nog steeds aanzienlijk groter dan voor huidige III-V quantum dot lasers. Doel van dit onderzoek is daarbij een volledig inzicht te verwerven in het potentieel van Ge gebaseerde lasers en te evalueren of deze route compatibel is met optische interconnectietoepassingen. Op basis van een standaard laser model werden de initiele vereisten om deze doelstelling te behalen als volgt bepaald:

- Het bereiken van een doperingsniveau van 1×10^{20} cm^{-3} in 400 nm dikke Ge lagen.
- Het bereiken van een niet-radiatieve levensduur van meer dan 10 ns in P-gedopeerde Ge lagen gegroeid op Silicium.

Om een eerste zicht te krijgen op de relevante recombinatie mechanismes in Ge, werden pomp-probe-spectroscopie metingen uitgevoerd op geïntegreerde Ge golfgeleiders (WG) in een silicium fotonicaplatform. Een levensduur van 1.2 ns voor 1.0 μm brede en 0.375 μm dikke golfgeleiders werd opgemeten. Deze levensduur is beperkt door recombinatie aan de zijwanden van deze golfgeleiders. De hoge recombinatiesnelheid voor de Ge/SiO$_2$ interface kan worden verbeterd met verschillende passiveringsschema's, zoals het groeien van een Si capping laag of een dikke GeO$_\text{x}$ laag. Deze opties werden uitgetest op dunne Ge-lagen met dikte 0,6 μm, gegroeid op Si. De hoogste levensduur, voor het optimale passivatieproces was 4.3 ns, waarbij de recombinatie dominant op de Ge/Si-interface plaatsvind. Uit deze resultaten blijkt dat het bereiken van een levensduur van minstens 10 ns in gedoteerd Ge een zeer agressief doel is, zelfs zonder rekening te houden met de impact van dopanten in de Ge-laag.

Parallel aan de levensduur studies, werd het epitaxy proces om sterk gedoteerde Ge lagen te groeien verder ontwikkeld. Initieel werden deze sterk gedoteerde Ge lagen gegroeid op 1 μm dikke virtuele Ge-substraten gegroeid op 300 mm Si wafers (001). De intensiteit van fotoluminescentie (PL) signaal opgemeten voor deze lagen nam toe met stijgend doperingsniveau, op voorwaarde dat de dopanten volledig geactiveerd werden. Deze stijging kan in verband gebracht worden met het pseudo direct band gap gedrag van hoog gedopeerd Ge, waardoor het een efficiëntere lichtbron wordt. Het snel verhitten van deze lagen op 700°C voor 30 seconden in N_2 helpt om het aantal puntdefecten in de gedopeerde Ge-lagen te reduceren en leidt dan ook tot een toename van het PL signaal. Het hoogste actieve doperingsniveau dat op deze manier kon worden bereikt is 5×10^{19} cm^{-3}.

Volgend op de ontwikkeling van het epitaxieproces, werden P-gedopeerde Ge-lagen met een uniform doperingniveau over de hele dikte gegroeid op Si. Een doperingniveau van maximaal $5{,}35\times10^{19}$ cm^{-3} werd bereikt in deze lagen, na een snelle annealstap. De breedte op halve hoogte (FWHM) van de PL spectra voor deze lagen bleek echter aanzienlijk groter te zijn dan deze voor niet gedopeerde lagen. Deze verbreding werd ook waargenomen voor de P-gedopeerde Ge lagen gegroeid op de 1 μm dikke virtuele Ge substraten. Figuur 1 toont de contour van de PL spectra gemeten voor alle gedoteerd gegroeide Ge-lagen. Een duidelijke verbreding van de PL spectra met verhoogde actieve P-concentratie is zichtbaar. Aangenomen wordt dat deze lijnverbreding het gevolg is van de aanwezigheid van geoniseerde P dopanten in de Ge-lagen. Deze geïoniseerde P dopanten veroorzaken verstrooiing door Coulomb interacties. Deze verbreding kan ook worden bestudeerd door de absorptiedynamiek van deze lagen te meten via transient absorptiespectroscopie. Ook de optische absorptie spectra verkregen met behulp van deze methode voor gedoteerde Ge-lagen zijn verbreed en verlaagd vergeleken met die van ongedopeerd Ge. De omvang van deze verbreding werd gekwantificeerd door de spectra te fitten met een verbeterd density of states model, dat de fysica van de verbredingseffecten meeneemt. Door de verbreding van de PL spectra en de transient absorptie spectra onafhankelijk van elkaar te fitten, bekomen we een verbredingsparameter $\Gamma_{\rm opt} > 45$ meV en $\Gamma_{\rm opt} = 8$ meV voor respectievelijk gedoteerd en niet gedoteerd Ge. Ook een daling van de niet-radiatieve levensduur van 3 ns voor niet gedopeerd Ge tot <0,3 ns voor P-gedopeerd Ge werd opgemeten. Dit geeft aan dat de levensduur in gedopeerd Ge beperkt wordt door puntdefecten en niet door defecten aan de Ge/Si-overgang. De resultaten van deze analyse worden weergegeven in Figuur 3. Deze experimentele resultaten tonen aan dat alhoewel P dopanten noodzakelijk zijn om Ge een efficiënte lichtbron te maken, de daarbij behorende verstrooiingseffecten en verkorting van de niet-radiatieve levensduur het bereiken van lage drempelstromen bijna onmogelijk maken. Daarom zijn we nu van mening dat Ge niet kan worden beschouwd als een potentiële route voor het

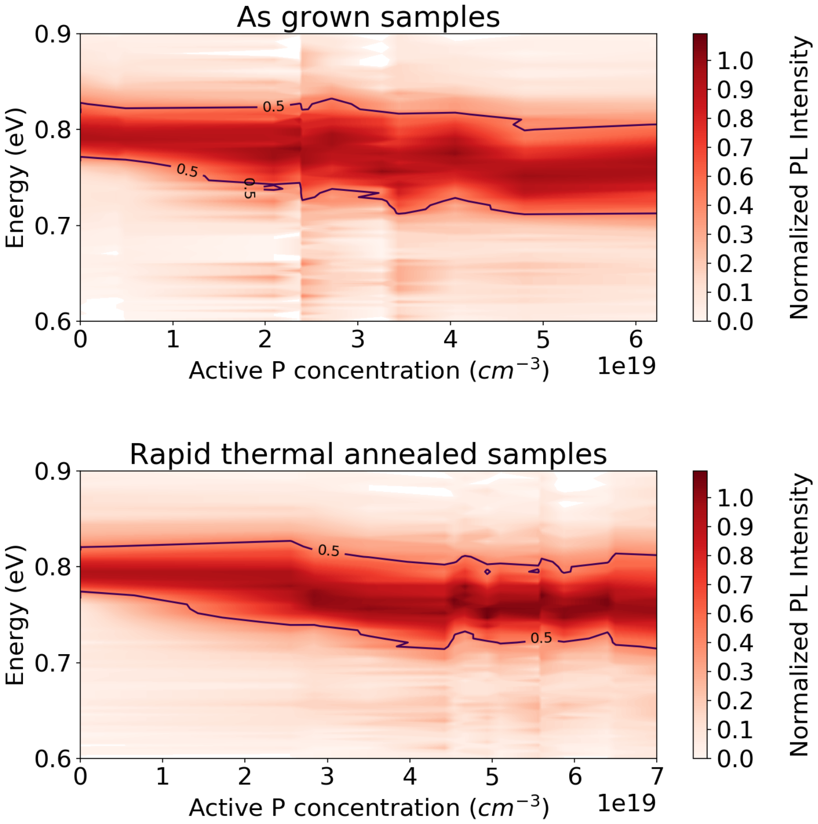

Figuur 1: Genormaliseerd fotoluminescentiespectrum van alle gedoteerde en niet-gedoteerde Ge-lagen gegroeid op 1 µm dik Ge virtuele substraten.

realiseren van efficiënte bronnen voor optische interconnectietoepassingen, aangezien dit zou leiden tot een onaanvaardbaar hoog stroomverbruik.

In parallel met het Ge laserwerk onderzochten we ook de mogelijkheid om Ge te gebruiken voor het realiseren van absorptiemodulatoren, gebruikmakend van het

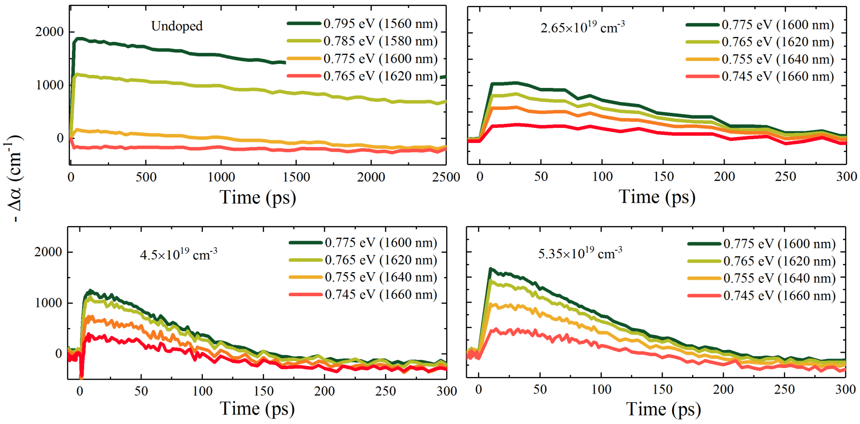

Figuur 2: Tijdsafhankelijke reductie in absorptiecoëfficiëntcontouren van niet-gedoteerde Ge en gedoteerde Ge, geëxtraheerd voor een vaste, door een pomp geïnduceerde fotogeëxciteerde dragerconcentratie bij verschillende golflengte om de vermindering in levensduur van de drager als gevolg van doping aan te tonen.

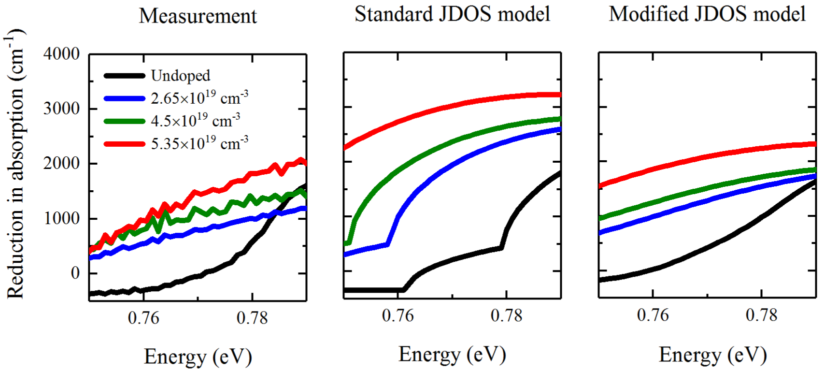

Figuur 3: Samenvatting van pump-probe spectroscopie voor alle gedopeerde monsters om de aanwezigheid van lijnbreedteverbreding te verifiëren en ze te fitten met een standaard en gemodificeerde toestandichtheidsmodel.

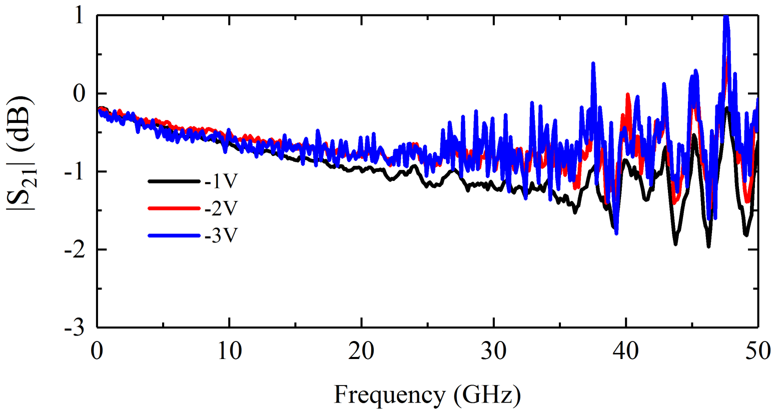

Figuur 4: RF S_{21} metingen van GeSi FKE EAM bij -1 V, -2 V en -3 V.

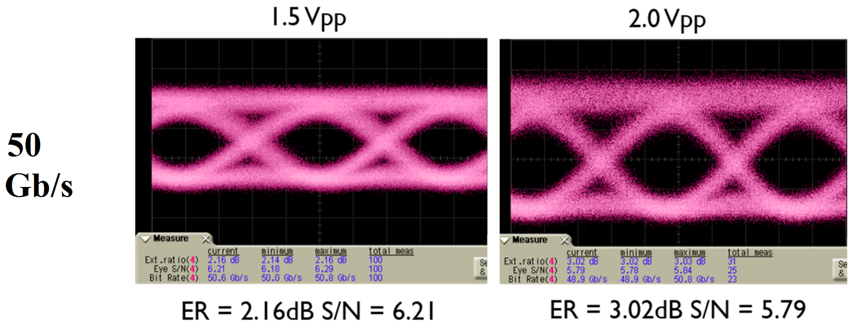

Figuur 5: Oogdiagrammen van GeSi FKE EAM met een aangelegde spanning van 1,5 V en 2,0 V, en met datasnelheden van 50 Gb/s.

Franz-Keldysh effect. In zo'n modulator wordt de absorptiecoëfficiënt van het materiaal gewijzigd door het aanleggen van een extern elektrisch veld. Ge gebaseerde golfgeleiders met afmetingen van 0.6 μm breed, 0.375 μm dik en 40 μm lang werden vervaardigd en gedoteerd om p-i-n diodes te vormen. Het doperingsprofiel werd geoptimaliseerd om het hoogste absorptiecontrast bij een spanningsvariatie van 2 V te bereiken. Een EAM met een extinctieverhouding van 4,2 dB voor een spanningsvariatie van 2 V en een verlies van 5,9 dB bij 0 V bias werd gemeten, op 1615 nm golflengte. De directe band gap van Ge is echter verschoven naar langere golflengtes als gevolg van de aanwezigheid van 0,16% biaxiale trekspanning wanneer het gegroeid wordt op Si. Om de operationele golflengte naar de C-band te verschuiven, werd 0,8% Si toegevoegd aan Ge om een GeSi FKE EAM te vormen. De statische prestaties bleven onveranderd, maar de operationele golflengte verschoof zoals gewenst naar 1560 nm. Deze modulatoren vertonen een minimum link power penalty van 9 dB, 6 dB meer dan die van een ideale modulator, en hebben een optische bandbreedte van $\sim$30 nm. Door hun compacte geometrie en het geoptimaliseerde dopingprofiel hebben deze modulatoren een 1 dB bandbreedte groter dan 50 GHz. Dit maakt NRZ-OOK modulatie mogelijk met een datasnelheid van 50 Gbps, zoals in Figuur 4 en Figuur 5 wordt getoond, met een dynamisch stroomverbruik van slechts 12,8 fJ/bit en een statisch stroomverbruik van 1,2 mW. De hoge bandbreedte, compacte voetafdruk en het extreem laag vermogenverbruik van deze modulatoren maken geavanceerde modulatieschemas mogelijk.

Ten slotte kan de hoge *link power penalty* van de Ge EAMs gebaseerd op het Franz-Keldysh effect worden verlaagd door het gebruik te maken van het quantum confined stark effect (QCSE). QCSE gebaseerde EAM's maken gebruik van de sterke excitonresonantie van SiGe/Ge quantum well lagen. Bovendien kan de materiaalsamenstelling van de stack in principe worden afgestemd op gebruik bij een golflengte van 1310 nm, waardoor ze ook geschikt zijn voor interconnectietoepassingen in en tussen datacenters.

Samenvattend kunnen we stellen dat Ge-gebaseerde elektroabsorptiemodulatoren veelbelovend zijn als oplossing voor het schalen van de bandbreedte van optische links binnen en tussen datacenters. Het gebruik van Ge als versterkingsmedium voor de realisatie van geïntegreerde lasers, is echter minder veelbelovend, en alternatieve oplossingen zoals monolithische III-V lasers moeten worden overwogen voor toekomstige optische transceivers.

English summary

"Science is the belief in the ignorance of experts.... It is our responsibility as scientists, knowing the great progress and great value of a satisfactory philosophy of ignorance, the great progress that is the fruit of freedom of thought, to proclaim the value of this freedom, to teach how doubt is not to be feared but welcomed and discussed, and to demand this freedom as our duty to all coming generations." - Richard P. Feynman

Modern day lifestyle is heavily dependent on the internet through video and speech recognition/processing applications, search engines, social networking, cloud computing and many internet of things applications. All of these applications are computation and data intensive and use the internet as the central hard drive and processing unit. In its Global Cloud Index Forecast and Methodology report for 2015-2020, Cisco predicts that this will result in a global IP traffic growing from 4.7 ZB in 2015 to 15.3 ZB by the end of 2020, with 92% of the total traffic to be handled by cloud computing based data centers. To be able to sustain this ecosystem economically and environmentally, the interconnections between the servers of the data centers must enable scaling of the communication bandwidth, with low latency and low power consumption.

In conventional electrical interconnects, scaling the number of pins in a package has lagged the I/O bandwidth demands of the processing nodes. This resulted in the need for increasing the data rate in each channel (each I/O pin). However, due to fundamental physical limitations associated with losses in the metal, electrical interconnects are faced with a bandwidth versus power consumption bottleneck that limits their scaling. Optical interconnects are considered as an alternative for electrical interconnects and both multi mode and single mode fibers have be adapted. In this field, optical transceivers that use silicon photonics can allow dense intra and inter chip communication, at high bandwidths, low power communication and small footprint have gained quick traction. A typical silicon photonics platform uses silicon-on-insulator (SOI) wafers and can include various components like (de)multiplexers, filters, fiber grating couplers and electro-optic modulators have been developed within this platform. Nevertheless, one of the biggest challenges it faces is the lack of monolithically integrated laser sources. Efforts to integrate light sources and other devices such as electro absorption modulators exploiting III-V materials include monolithic growth of these materials on silicon, heterogeneous integration of III-V layers through wafer bonding or even externally coupled devices. But these approaches face several challenges, including processing complexity, processing cost, the need to scale the number of channels without compromising on the power consumption and/or coupling light to the SOI waveguides. Ge on the other hand can be easily integrated in an existing silicon photonics platform, as it was demonstrated extensively with the realisation of high speed Ge photodetectors. Given the presence of a direct band gap at 0.8 eV (1550 nm), Ge is a good candidate to realize laser sources and electro absorption modulators operating in wavelength ranges that are relevant for datacom and telecom applications. Therefore, in this thesis, a comprehensive study evaluating the performance of Ge based laser sources and electro absorption modulators can be technologically compatible with future optical interconnect applications is presented.

As it is the case for Si, Ge is intrinsically an indirect band gap material and hence an inefficient light emitter. However, the degree of indirectness in Ge is much smaller than for Si. As a consequence, Ge can be made a pseudo direct band gap material or even a direct band gap material, either by adding n-type dopants (to make it pseudo direct band gap), or by introducing uniaxial/biaxial tensile strain or via alloys with Sn (to make it a direct band gap material). When Ge is converted to a direct band gap material using the latter two approaches, the light emitted has a wavelength of > 2000 nm. Such wavelengths suffer large chromatic dispersion in conventional fiber optic cables and hence cannot support high speed bandwidth signals for distances relevant in a data center. On the other hand, a pseudo direct band gap Ge obtained through n-type doping enables light emission at wavelengths < 1700 nm, which are affect much less by chromatic dispersion. Therefore, in this thesis, highly n-type doped Ge was identified as the most relevant route towards an electrically pumped laser emitting at a wavelengths < 1700 nm. We thereby set an initial threshold current density target of 10 kA/cm^2. This is a 30-fold improvement from previously demonstrated electrically pumped Ge lasers but also still considerably larger than the current state of the art III-V based quantum dot lasers. During the course of trying to reach this target, we aim to establish a complete understanding of the potential of Ge based lasers and to evaluate if this route is compatible with optical interconnect applications. A standard joint density of states model was developed to identify the device requirements. Preliminary results from a standard joint density of state model from which we identify the following requirements to obtain a $\mathrm{J_{th}}$ $<$10 kA/cm^2 Ge laser:

- Reaching Ge layers with doping level of 1×10^{20} cm^{-3} is essential.
- Retaining a Shockley Read Hall recombination mediated carrier lifetime $>$ 10 ns in P-doped Ge with a thickness of 0.4 μm grown on Si is essential.

To gain some initial understanding of the relevant recombination mechanisms in Ge, carrier lifetime measurements were performed, using pump-probe spectroscopy, on undoped Ge waveguides (WG) integrated in a silicon photonics platform. A carrier lifetime of < 1.2 ns was extracted for a 1.0 μm wide and 0.375 μm thick Ge WG. This lifetime is limited by the defects at the sides of the WG, where an interface recombination velocities of 0.975×10^4 cm/s and 1.45×10^4 cm/s for Ge/Si and Ge/SiO$_2$ interface were extracted respectively. The high recombination velocity for the Ge/SiO_2 interface can be improved through various passivation schemes, such as a Si cap or a thick GeO_x layer. We implemented such schemes on thin Ge films with a thickness of 0.6 μm grown on Si to simplify the study. The highest carrier lifetime extracted from these films was of 4.3 ns, with the dominant recombination occurring at the Ge/Si interface. These results shows that obtaining a lifetime of at least 10 ns in doped Ge as set forward in chapter 2 is a very aggressive target, even without considering the impact of dopants in the Ge layer.

In parallel to the carrier lifetime studies, the epitaxy process through which we can grow highly n-type doped Ge layers was further developed by the epitaxy team at imec with my role covering the optical characterization, device and material physics modeling. Highly doped Ge was grown on 1 μm thick Ge virtual substrates which were grown on 300 mm Si wafers (001). In-situ doping with Phosphorus was performed in an ASM-Intrepid XP^{TM} epi tool with Ge_2H_6 and PH_3 used as precursor gases. P atoms up to a concentration of 4×10^{20} cm^{-3} were incorporated in Ge, but the surface of the layers became rougher as the concentration exceeded 7×10^{19} cm^{-3}. A maximum active P concentration of 6.2×10^{19} cm^{-3} was extracted for unannealed layers. The photoluminescence (PL) intensity from these layers increased as the doping level increased, provided the dopants were fully activated. This increase can be related to the pseudo direct band gap behaviour of heavily doped Ge, which renders it a more efficient light emitter. Rapid thermal annealing at 700°C for 30 seconds in N_2 helped to reduce point defects in the doped Ge layers and consequently increased the PL intensity further. Nevertheless, the highest active doping level that could be obtained after annealing was around 5×10^{19} cm^{-3}.

Having developed and analyzed the details of the epitaxy process, P-doped Ge layers with uniform doping level across the entire Ge thickness were grown on Si. However, the full width at half maximum (FWHM) of the PL spectra obtained for these layers was found to be significantly larger ($\sim 1.5\times$) than those extracted from undoped Ge. This broadening was also observed for all P-doped Ge layers grown on 1 μm thick Ge virtual substrates. Fig. 6 shows the contour of the PL spectra measured for all doped Ge and undoped Ge layers measured. A clear broadening of the PL spectra with increased active P concentration is measured from the as grown and the annealed Ge layers. This is believed to originate from carrier scattering induced linewidth broadening effects related to ionised P dopants present in the Ge layers. These ionised P dopants are the source of Coulomb scattering events that broadens the recombination and absorption/gain spectrum of the material. This broadening was further investigated by studying the absorption dynamics of these layers using transient absorption spectroscopy. The optical bleaching spectra obtained using this method from doped Ge-layers were broadened and suppressed compared to those of undoped Ge. The extent of this broadening was quantified by fitting them with a modified joint density of states model that includes the carrier scattering physics. By independently fitting the broadening of the PL spectra and optical bleaching spectra, we could extract a broadening parameter $\Gamma_{opt} > 45$ meV and $\Gamma_{opt} = 8$ meV for doped and undoped Ge. A drop in carrier lifetime from 3 ns in undoped Ge (unpassivated) to <0.3 ns for P-doped Ge

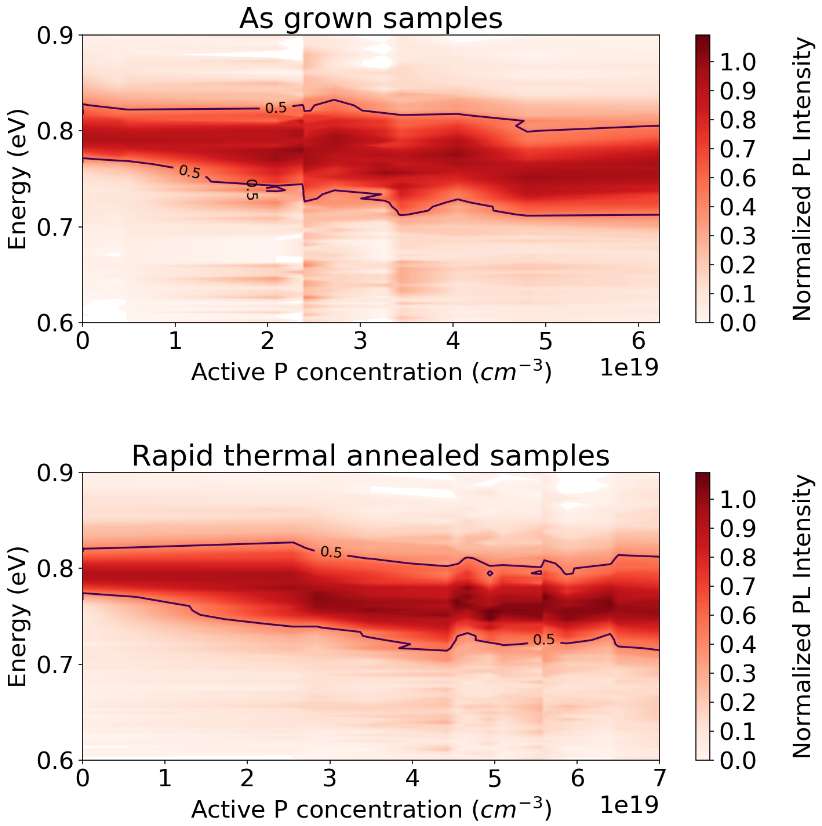

Figure 6: Normalized photoluminescence spectra from doped and undoped Ge layers grown on 1 μm thick Ge virtual substrates.

was also observed in the transient absorption measurements. This indicates that the lifetimes in doped Ge are limited by point defects and not by the defective Ge/Si interface. The results of this analysis are shown in Fig.8. All these experimental results show that even though P dopants are necessary to make Ge an efficient light source, the associated carrier scattering effects and reduction in carrier lifetime are detrimental for low threshold laser operation. They increase the expected thresh-

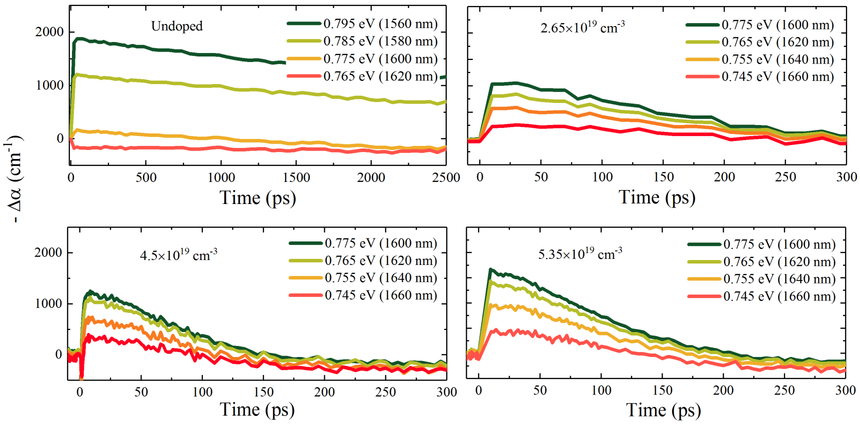

Figure 7: Time resolved reduction in absorption coefficient of undoped Ge and doped Ge extracted at different wavelengths to demonstrate the reduction in carrier lifetime in doped Ge.

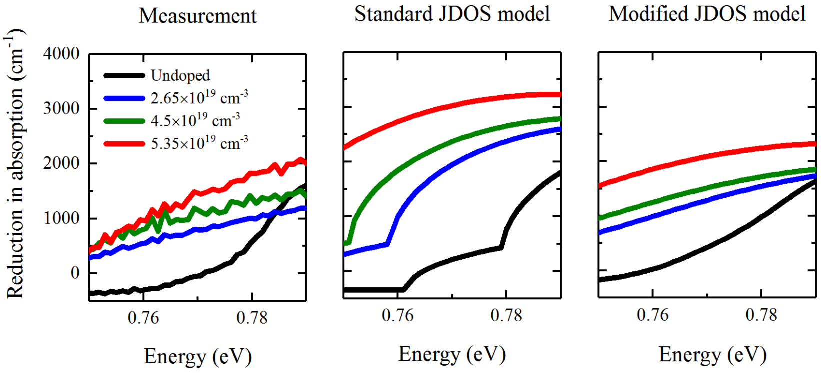

Figure 8: Summary of Pump-probe spectroscopy for all doped samples verifying the presence of line-width broadening.

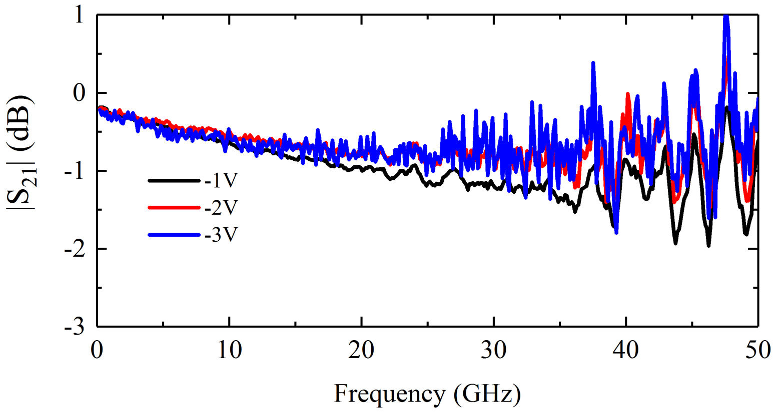

Figure 9: RF S_{21} measurements of Ge EAM at -1 V, -2 V and -3 V.

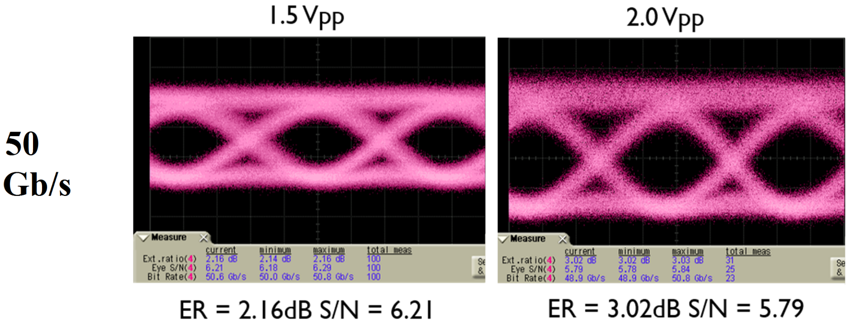

```
        current   minimum   maximum   total meas
Ext.ratio(4)  2.16 dB   2.14 dB   2.16 dB   100
  Eye S/N(4)  6.21      6.18      6.29      100
 Bit Rate(4)  50.6 Gb/s 50.0 Gb/s 50.8 Gb/s 100
```

ER = 2.16dB S/N = 6.21

```
        current   minimum   maximum   total meas
Ext.ratio(4)  3.02 dB   3.02 dB   3.03 dB   31
  Eye S/N(4)  5.79      5.78      5.84      25
 Bit Rate(4)  48.9 Gb/s 48.9 Gb/s 50.8 Gb/s 23
```

ER = 3.02dB S/N = 5.79

Figure 10: Measured eye diagrams from GeSi FKE EAM with 1.5 Vpp and 2.0 Vpp voltage swing and with data rates of 50 Gb/s.

old current density by a factor > 40 and make it extremely difficult to achieve a laser operating with $J_{\mathrm{th}} < 10$ kA/cm^2. Therefore, we now believe Ge cannot be considered as a potential gain material for optical interconnect applications as it would lead to an unacceptably high power consumption.

In parallel to the Ge laser work, we also investigated the potential of using Ge for realizing absorption modulators, exploiting the Franz-Keldysh effect. In such a modulator, the absorption coefficient of the material is modified at photon energies below the band gap through the application of an external electrical field. Ge based WG with dimensions of 0.6 μm wide, 0.375 μm thick and 40 μm long were fabricated and doped to form p-i-n diodes. The doping profile was optimised to provide the highest contrast in absorption for a voltage swing of 2 V. An EAM with an extinction ratio (ER) of 4.2 dB for a voltage swing of 2 V and an insertion loss (IL) of 5.9 dB at 0 V bias was measured at 1615 nm wavelength. The figure of merit defined as ER/IL for such a device was <1 for a voltage swing from 0 to -2 V (2 Vpp). However, the direct band gap of Ge is red shifted due to the presence of 0.16% of biaxial tensile strain when grown on Si, away from the wavelength region relevant for telecom applications. To shift the operating wavelength to the C band, 0.8% Si was added to Ge to form a GeSi FKE EAM. The static performance remained unchanged but the operating wavelength shifted to 1560 nm. These devices were shown to allow for a minimum link power penalty of 9 dB, 6 dB more than that of an ideal modulator, and have an optical bandwidth of $\sim$30 nm. The compact geometry and optimized doping profile of these diodes make it a high speed modulator whose 1 dB S_{21} bandwidth is $>$50 GHz. This enables NRZ-OOK modulation at a data rate of 50 Gbps, as seen in Fig. 9 and Fig. 10, with dynamic power consumption of 12.8 fJ/bit and static power consumption of 1.2 mW for 2 Vpp swing. The high bandwidth, compact footprint and extremely low power consumption of these modulators enable advanced modulation schemes such as space division multiplexing and PAM-4.

The high link power penalty of the Ge EAM exploiting the FKE can be reduced by expoiting the quantum confined stark effect (QCSE). These QCSE EAMs use the sharp exciton resonance enhanced absorption features of SiGe/Ge quantum wells. An applied bias modulates the spectral position of this resonance and results in high figure of merits. A FOM of up to 1.75 was extracted from initial demonstrations for 1 Vpp swing at 1520 nm wavelength when heated to 75°C, which is 3× better than what measured for Ge based FKE EAM. Moreover, the material composition of the stack can in principle be tuned to operate at 1310 nm, making the device potentially suitable for intra data center interconnect applications.

In conclusion, Ge based electro absorption modulators, exploiting the Franz Keldysh effect and the quantum confined stark effect, can provide a solution for bandwidth scaling and with low power consumption for intra and inter data center optical links. However, using Ge as a gain medium will result in high power consumption and alternative solutions such as monolithic III-V lasers must be considered for future optical transceivers.

1
Introduction

1.1 Optical Interconnects

The current information technology ecosystem is strongly driven by the growing need for multimedia services and video on demand services, internet of things applications, social networking and cloud computing that requires significant bandwidth to transport and store data. These compute-intensive and data-intensive applications use the internet as the central hard drive and processor unit and have created the need for increasingly powerful data centers [1]. These applications require complex and frequent communication between the servers. Such a high level of interaction creates the need for energy efficient interconnection schemes with high bandwidth and reduced latency even though the size of the data center increases. To elaborate further, the annual global data center IP traffic is predicted to reach 15.3 zetabytes (ZB) by the end of 2020 from 4.7 zetabytes (ZB) in 2015 as reported in Cisco Global Cloud Index: Forecast and Methodology report for 2015-2020 [2]. By 2020, 92% of this workload will be located in cloud computing oriented data centers. For such a high volume of traffic within a data-center, fast processing speeds at low latency communication play a vital role in big data and cloud computing applications. For example, a latency of 0.5 s when loading a search page reduces Google's search traffic by 20% and a latency of 0.1 s while loading a page in Amazon's website decreases the sale by 1% [3]. In addition to this, power consumption management is a challenging issue in the design of data centers. It is estimated that in 2015, 3% of the global electricity supply (higher than UK's annual power consumption) and 2% of the total greenhouse gap emissions (same carbon footprint as the airline industry) had their origins from data centers [4]. Such high power consumption adds pressure to the economics of maintaining and scaling the size of data centers as the majority of the cost is not spent in the computing, switching and routing equipment, but on powering, operating, maintaining and administrating the data centers [1, 5]. As a consequence, there is a need for interconnection schemes that address high bandwidth with low latency and low power consumption.

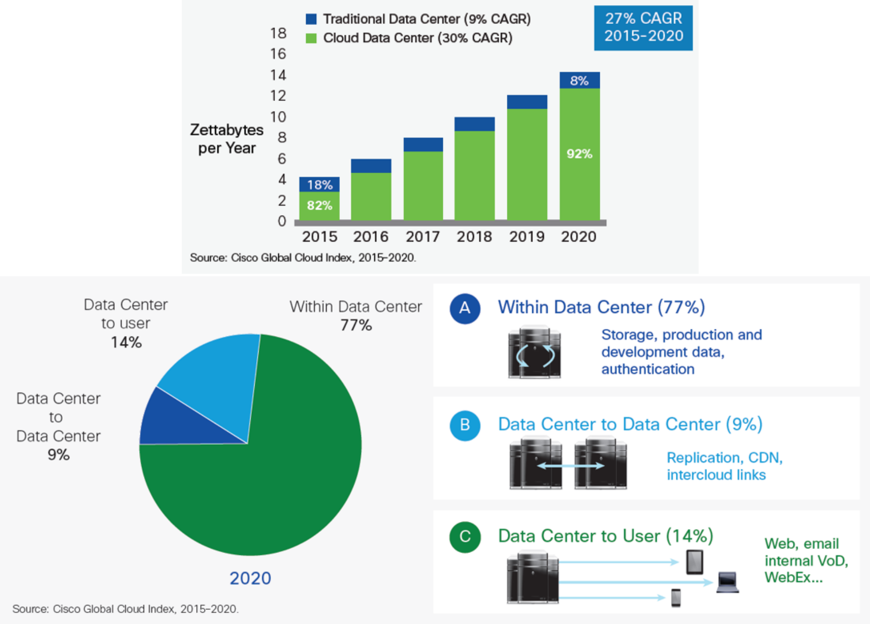

Figure 1.1: Global data center traffic in 2020 predicted in Cisco Global Cloud Index: Forecast and Methodology report for 2015-2020 [2].

Modern hyperscale data centers and high performance computing systems consist of high volumes of compute nodes with local main memory and are interconnected using high speed interconnect networks [8]. In such ecosystems, computation or memory intensive applications are decomposed into many smaller tasks and are executed in parallel. Interconnection demands between the processing nodes therefore scales with the I/O bandwidth requirements of each node. High end processing nodes with multiple Tbps I/O bandwidth needs are already commercially available as shown in Fig. 1.2 [6, 7]. These I/O bandwidth requirement double every 3-4 years with the need for 20 Tb/s bandwidth looming around in the coming few years [9]. However, the number of I/O pins per package, for electrical inter-

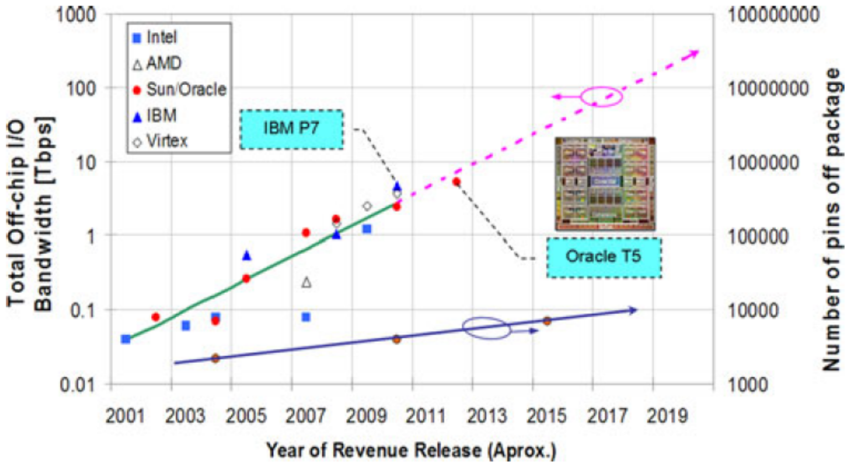

Figure 1.2: I/O bandwidth requirements of commercially available FPGA chips and processors taken from [6, 7].

connection, dedicated to address these I/O demands have scaled slowly with the number doubling every 6 years. Since the number of I/O pins lagged the processor I/O needs, bandwidth scaling in electrical connections was achieved by increasing the data rate in each channel (each I/O pin). However, these electrical interconnects suffer from fundamental physical loss mechanisms due to dielectric loss and skin effect losses that scale as a function of distance and bandwidth. In an effort to increase the transmission data rate, the industry pursued higher order modulation schemes that required equalization and noise cancellation circuits, which increased the power consumption without a substantial increase in the distance reach. For example, the power consumption from a commercially available switch chip is 20-40 pJ/bit where the dominant energy consumption is from the electrical I/Os of the chip as the switching circuits are implemented with $<$ 1 pJ/bit [5]. Moreover, industries move towards the Shannon's capacity limit for communication through channels in a typical electrical interconnection [10]. Therefore, for cloud data centers where the communication distance spans from 300 m to 2 km, the interconnect scaling and performance are severely limited by the interconnect frequency. In order to address this ever increasing demand of bandwidth and the long distance reaches in a data center while operating at low power consumption of 1 pJ/b, multimode and single mode optical interconnects have been adopted [7]. In the current cloud based data centers, optical interconnects have been deployed between servers and Top of the Rack switches (TOR) illustrated in Fig. 1.3 and

Table 1.1. Low cost VCSEL based transceivers with multi-mode fiber (MMF) operating at 850 nm wavelength are the preferred choice of optics that are currently being deployed in the data center. But they will soon be replaced with single mode fiber (SMF) based transceivers that support data rates up to and beyond 100 Gb/s with reach that can support the expanding size of data center for intra data center links and inter data center links [11]. The typical choice of wavelength for these SMF based transceivers are O- band for intra data center optical links and C- band for inter data center optical links.

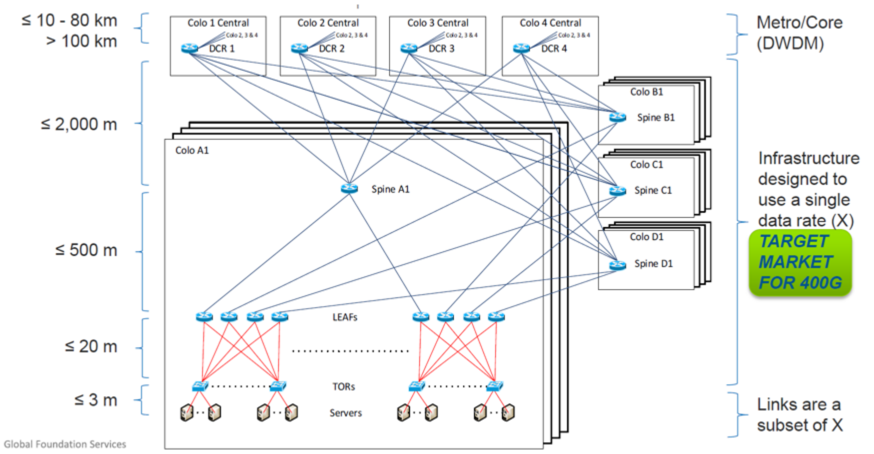

Figure 1.3: Schematic illustrating the interconnection in a cloud data center campus taken from [12].

Within the framework of optical interconnects, silicon photonics has emerged as an energy-efficient solution that can allow high bandwidth intra chip and inter chip communication while maintaining a low power consumption and small footprint [9]. Silicon photonics transceiver with 4-channel space division multiplexed (eg: 100G-PSM4-QSFP28 form factor from Mellonox, Luxtera and Intel) and 4-channel coarse wavelength division multiplexed (eg: 100G-CWDM4-QSFP28 form factor from Intel) to meet 100 GbE Ethernet application are already commercially available [14–16]. These solutions can modulate data at a speed of >25 Gbps per channel without the need for any equalization and consume very low power (the silicon photonic optical transceivers from Intel and Mellanox consume 3.3-3.5 W or >30 pJ/bit) [9, 17]. Moreover, the CMOS foundry manufacturing promises high yield, high reproducibility and reliable production of transceivers at very low cost due to the exploits of economies of scale. Therefore, silicon photonics solutions with the objective of developing high density of integrated optical I/O bandwidth density of 100 Gbps/mm^2, power consumption of <10 pJ/bit, capable

A end	Z end	Volume per colo	Reach (max)	Deployed today (40GbE)	Being Upgraded (100GbE)	Planned for future (400GbE)	Cost sensitivity
Server	TOR	10000s	3 m	10G copper or AOC	25G cooper or AOC	50/100G copper or AOC or 100G SMF	Extreme
TOR	LEAF	1000s	20 m	40G MMF or SMF	100G SMF	400G SMF	High
LEAF	Spine	100s	400-2000 m	40G MMF or SMF	100G SMF	400G SMF	Medium/ High
Spine	Core	100s	500-2000 m	40G SMF	100G SMF	400G SMF	Medium
Core	Metro	100s	10 km-metro	10G/40G/100G DWDM	100/200/400G DWDM	100/150/200/400G FlexEthernet	Low

Table 1.1: Details about the interconnect medium in a cloud data center compus [11–13].

of operating at temperatures >100°C and at a cost of <1 $/Gbps have been the main industrial focus for future optical interconnects [11].

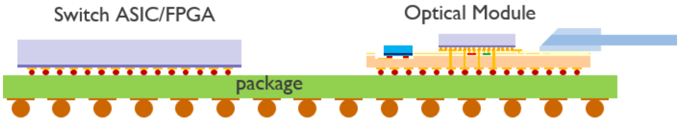

Figure 1.4: Schematic of electrical channel between the payload IC and optical engine [18].

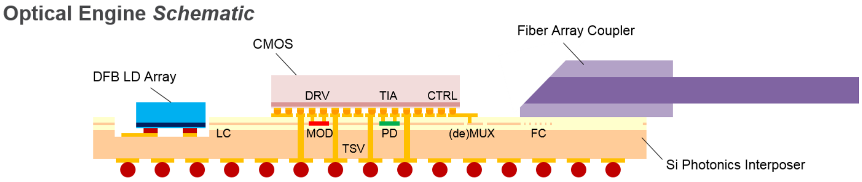

Figure 1.5: Schematic cross-section of an optical engine in Fig. 1.4 consisting of a Silicon photonic interposer and a CMOS IC to drive the photonics circuit taken from [18]. The components of this optical engine are listed in Table 1.2.

1.2 Silicon Photonics

Example of a communication channel between the payload IC and the optical engine that can be implemented in an energy-efficient way is shown in Fig. 1.4 [18]. Here, the optical engine consisted of a CMOS chip with drivers used for modulators, trans-impedance amplifiers for the photodetectors and some control circuitry, but also a photonics IC with active components such as laser diodes, modulators, photodetectors and passive components such as multiplexers/demultiplexers, light couplers and fiber couplers as summarized in Table 1.2. These photonic ICs have been demonstrated on a number of different platforms based on III-V materials, silicon nitride or silicon-on-insulator [19–23]. Each platform has its distinct properties but due to low cost fabrication and high refractive index contrast between the waveguide core and surrounding (Δn $\approx$ 2 at λ=1550 nm) leading to highly confined waveguide modes and tight device integration, the silicon-on-insulator platform is becoming a main stream option.

The silicon photonics platform from imec uses 200 mm or 300 mm diameter silicon-on-insulator wafers with 220 nm of top crystalline silicon and 2 μm of buried oxide (BOX) [17, 23]. This platform exploits the benefit of using high-volume, high-yield tools and technological processes used to develop and fabri-

Module	Abbreviation	Name
CMOS	DRV	Driver
CMOS	TIA	Trans-impedance amplifier
CMOS	CTRL	Control circuitry
CMOS and Photonics	TSV	Through Silicon Via
Photonics	LC	Light coupler
Photonics	(de)MUX	Multiplexer and Demultiplexer
Photonics	FC	Fiber coupler
Photonics	DFB LD	Distributed feebback laser diode
Photonics	MOD	Modulator
Photonics	PD	Photodetector

Table 1.2: Components part of the optical engine in Fig. 1.5.

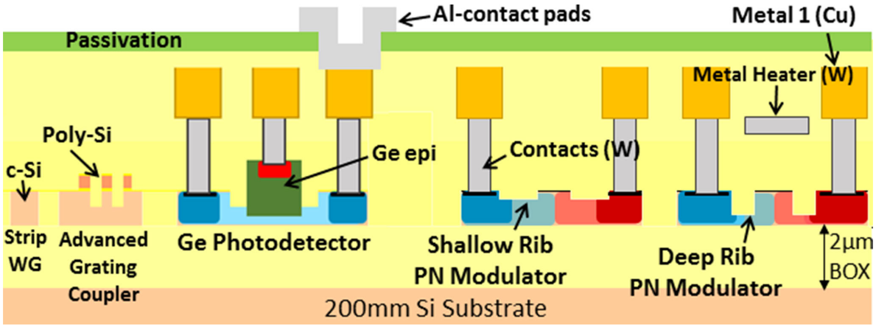

Figure 1.6: Schematic cross-section of imec's silicon photonics, capable of handling 50 Gb/s NRZ-OOK modulation, showing basic active and passive devices taken from [17].

cate CMOS electronic chips [17, 23]. The waveguides are patterned using 193 nm lithography. The 300 mm platform has an additional benefit of using 193 nm immersion lithography that can be used for the realization of advanced devices. The top 220 nm of crystalline Si, along with patterning steps that enable etch depths of 220 nm, 150 nm and 70 nm, and an additional deposition of a 160 nm thick polysilicon layer on top of the crystalline Si are used to realize passive components like waveguides, multiplexers/demultiplexer and fiber-grating couplers [24–27]. The Si can be doped with n-type or p-type dopants using 3 implantation steps in order to tailor the doping level to form different flavours of p-i-n diodes. These diodes are used as electro-optic modulators in Micro Ring Resonator or Mach Zehnder configurations [17, 28]. Ge mesas, to enable photodetectors in the platform, are selectively grown in oxide trenches formed on top of the 220 nm Si layer. After a Ge chemical mechanical polishing (CMP) step to planarize the top surface, a threading dislocation anneal to reduce bulk defects, n-type and p-type implants in Ge followed by a 550°C anneal to activate the dopants are performed. The above mentioned active and passive components enable scaling of optical channel bandwidths by employing wavelength division multiplexing (coarse WDM or dense WDM) and space division multiplexing in PSM4 configuration as shown in Fig. 1.7 [18, 29, 30]. However, a key component missing in the platform shown in Fig. 1.7 is a monolithic light source.

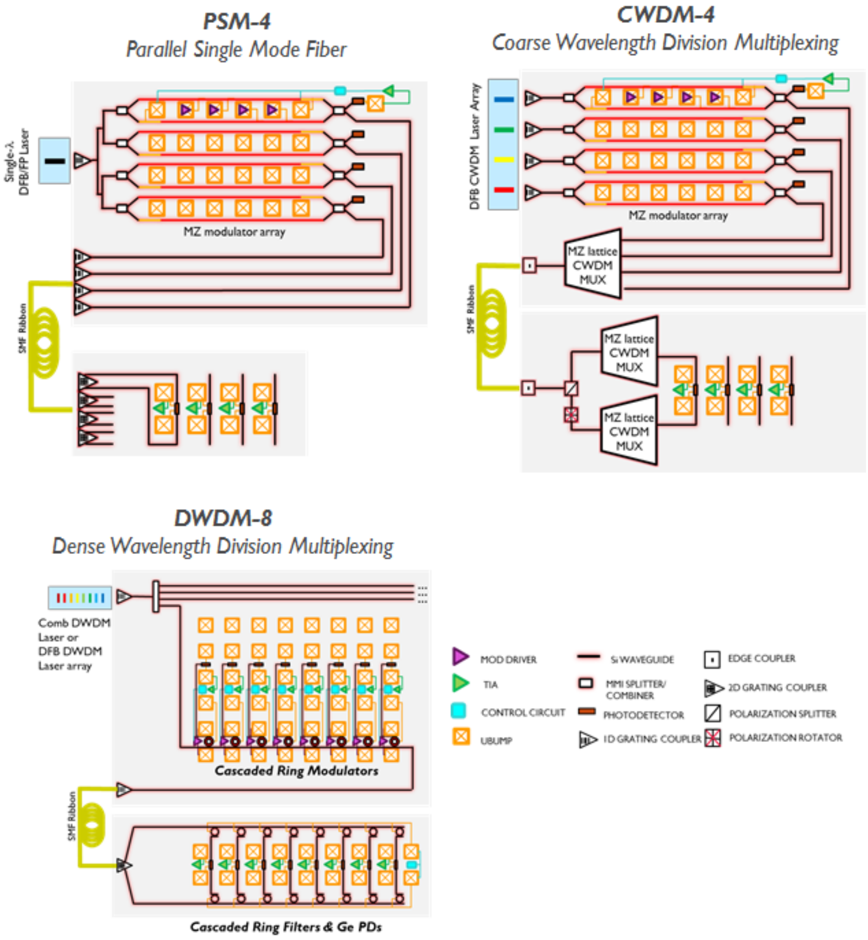

Figure 1.7: Schematic showing possibilities of scaling the number of optical channels using Si photonic devices in Fig. 1.6 by exploiting the spatial and frequency dimensions of the channel [18, 29, 30].

1.2.1 Lasers for Silicon photonics

A laser typically comprises of a cavity and a gain medium. The device is operated when the active medium is populated with electrons and holes, either electrically or optically pumped, that modifies the absorption spectrum/coefficient of the material. Beyond a critical injection point called the transparency condition, the injected carriers make the material act as a gain medium through the process of stimulated emission. When the net active gain matches the optical losses in the cavity, the device begins to lase (this operating point is called the laser threshold). As simple as this explanation may look, factors such as heat generated due to electrical or optical pumping and a reduced carrier lifetime associated with Shockley-Read-Hall recombination effects, to name a few, play a crucial role in the efficiency of the device. As a result, over the years many approaches were considered to bring coherent light on to the silicon photonics platform [31–33]. Below is a summary of the different types of coherent light sources that have been proposed to be integrated on a silicon photonics platform:

1. **Si Raman laser**: When optically pumped, Si enables light generation and amplification due to the Raman effect, whereby the raman gain coefficient in Silicon is $10^4\times$ higher than the gain coefficient in fiber. On pumping Si waveguides at 1540 nm wavelength using a pulsed laser, stimulated amplification and hence lasing was observed at 1675 nm (Stoke's wavelength) [34–36]. Even though this was the first laser demonstration on Si, the devices need an additional external laser to optically pump the waveguide, making it impractical for optical interconnect applications.

2. **Er-doped laser on SiN**: The success of Erbium doped fiber amplifiers led to the exploration of similar type of light sources on Si. These devices use Er as an atomic light emitting center in SiO_x:Er, SiN_x:Er, Al_2O_3:Er^{3+} and Er silicates [31, 37, 38] and have led to demonstration of optically pumped C and L band waveguide lasers with SiN core waveguides. However, a low concentration of active Er atom was reported, resulting in low net gain ($\sim$7 cm^{-1}) and cavity length up to 20 mm. Moreover, the presence of dielectrics hinders the transmission of electrical current making it a highly inefficient light source, when electrically pumped [31].

3. **Colloidal QD based laser**: Colloidal quantum dots are inorganic semiconductor materials that are dispersed in a solution and have strong quantum confinement properties due to their nanometer size geometries. The strong quantum effect provide attractive optical and electrical properties that have been exploited to form SiN based lasers with QDs comprising of CdSe/CdS core/shell as the gain medium. Initial optically pumped microdisk and distributed feedback lasers at visible wavelength show very promising

results [39, 40]. However, achieving uniform distribution of QDs across large area of active medium, extending the wavelength to support datacom communication and realizing an electrically pumped laser are some of the challenges the research community have to tackle before they can become a mature source for optical interconnects.

4. **External cavity laser**: Here, an external gain medium or SOA is coupled to a SOI circuit containing with a cavity design using a grating coupler or a SiN spot size converter [41, 42]. This approach shows an easy way to integrate a gain medium with an existing Si photonics platform, however, dense integration to scale the number of optical channels would be technologically challenging. Moreover, the coupling losses from the gain medium or SOA to the silicon photonics chip is a source of optical power loss that affects the link power consumption and can be reduced with other laser integration approaches.

5. **Heterogeneously integrated III-V on Si**: In this approach, a pre-fabricated III-V stack or laser is integrated on a Si photonics chip using flip-chip technology, pick-and-place technology or using transfer printing techniques. They can be integrated through either direct integration or using wafer bonding techniques. In direct integration, individual laser diodes are integrated on a SOI wafer using soldering bumps. This allows for pre-selection of functional lasers but comes at the expense of increased assembly cost due to the need for sub-micron precision alignment [43]. Luxtera has pioneered this approach where they use a ball lens to overcome alignment constraints [32]. In general however, this approach becomes complicated while scaling the number of channels. On the other hand, wafer bonding techniques can be performed using direct bonding or indirect bonding that use metal or polymers (DVS-BCB or BCB) act as adhesive layers. A detailed process flow can be found in [32, 33, 44, 45]. Devices fabricated with metal bonding provide low contact resistance and excellent thermal dissipation properties, but suffer from high absorption from the bonding metal and increased processing complexity to selectively remove the metal from the region critical for light coupling. On the other hand, adhesive bonding results in less fabrication complexity, but at the cost of poor thermal conductivity. The poor conductivity of the polymers can lead to laser performance degradation with time and therefore asks for optimization around the polymer thickness. On the other hand, direct bonding involves molecular bonding between the surface of the III-V die and the SOI wafer. This technique needs ultra clean and atom-scale smooth surfaces resulting in a complex fabrication process that can result in low yield, but provides high quantum efficiency and decent thermal conductivity. The Si photonics products from Intel includes hybrid

lasers that are based on bonding technique [11]. Fig. 1.8 shows some examples of hybrid Si lasers [46–48]. These hybrid Si lasers can use III-V QDs as their active medium resulting in extremely low threshold current density (205 A/cm^2) and increased device reliability, making it a strong candidate for short-reach interconnects [49]. Integration of additional III-V devices like an electro absorption modulator (EAM) with 12 dB of extinction ratio for 0 to -2.5 V swing (2.5 Vpp) and the insertion loss of 1.2-5 dB are also feasible [45]. As a result, the heterogeneous integration of III-V on Si is a promising technology for future short-reach optical interconnect but it suffers from processing complexity and additional associated cost, which point towards the need for monolithically integrated solutions that can be useful for scaling the number of optical channels.

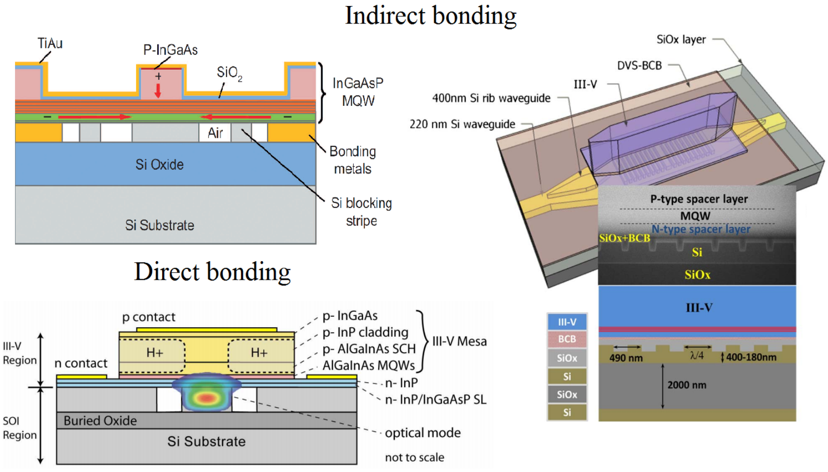

Figure 1.8: Cross-sectional schematic of Hybrid Si laser formed by using direct and indirect bonding techniques [46–48].

6. **Monolithic III-V on Si**: Monolithically integrated laser diodes on Si can fully exploit the economics of scale silicon photonics promises. But the growth of III-V materials on Si faces challenges such as large lattice constant mismatch (8% for InP/Si and 4% for GaAs/Si) and the polarity mismatch between Si and III-V materials. Growing III-V materials directly on Si results in huge density of threading dislocation defects that are detrimental for laser operation and the device reliability over time [33]. To tackle this, strained layer superlattices (SLSs) as a dislocation filter layer or using quantum dots (QD) as defect filters that bend the threading dislocations have been adopted but they all require very thick buffer layers. Electrically

pumped QD III-V lasers with very low threshold current and long mean time to failure (MTTF) have been demonstrated [50–53]. New materials beyond the conventional InP and GaAs such as GaP based GaNAsP and GaSb have been explored to reduce the buffer thickness. Alternate buffer-less epitaxial strategy exploiting shallow trench isolation process and aspect ratio trapping have enabled an optically pumped O-band laser and can enable coupling of light to silicon waveguides. However, efficient electrical injection and coupling to Si WGs still remains as a challenge [54–58].

7. **Ge based laser on Si**: Inspite of having 4% lattice mismatch with Si, Ge is a CMOS compatible material with much less processing complexity [59, 60]. The high refractive index of Ge (4.2 in Ge as compared to 3.4 in Si at 1550 nm) allows for easy and efficient coupling of light from the silicon waveguide to the Ge waveguide, with good confinement. As a result, the active medium can be located in close proximity to Si WG and allows for the realization of efficient photodetectors, electro-absorption modulators and possibly laser sources. However, undoped Ge is an indirect band gap material and the gain coefficient from such a material is unacceptably low. High n-type doping, biaxial/uniaxial tensile strain or Sn alloying can increase the quantum efficiency for light emission of Ge by making it a pseudo direct band gap or direct band gap material [61, 62]. Optically and electrically pumped lasers on Si operating at 1550-1700 nm (for the n-type doping case, at room temperature), at 1550 nm (for tensile strained Ge but at cryogenic temperatures) and at $>$ 2000 nm (for GeSn also at cryogenic temperatures) wavelengths have been demonstrated [63–72]. But, the threshold current density of these demonstrated devices are very high, leaving significant room for improvement. This observation serves as the main motivation for this thesis and will be elaborated in Chapter 2.

1.2.2 Modulators for Silicon photonics

Another device that is currently not fully satisfactory is the modulators. Externally modulated devices typically help in relaxing the frequency limits bandwidth of directly modulated laser diodes and allow the laser to operate in CW mode. Over the years, many approaches have been considered to realize Si based modulators that can be monolithically integrated in a Si photonics platform. They exploit the plasma dispersion phenomena in Si as a phase shifting element in the form of metal-oxide-semiconductor (MOS) capacitor, pin diode and pn diode [17, 28, 73]. Using these phase shifting elements, electro-optic modulators in micro ring resonator (MRR) and Mach Zehnder interferometer (MZI) configurations were demonstrated. MZI modulators typically exhibit large optical bandwidth, but they suffer from a large footprint and high power consumption for high speed

Modulator configuration	Footprint (μm$\times$$\mu$m)	Optical Range	ER (dB)	IL (dB)	Speed	Power consumption
MZI	∼2000 ×500	>80 nm	2.3	5.6	56 Gb/s	720 fJ/bit
MRR - Low Q	∼10×10	∼300 pm	6.1	8.4	50 Gb/s	12.8 fJ/bit
MRR - High Q	∼10×10	∼50 pm	6.6	1.8	16 GHz	-

Table 1.3: Summary of high speed Si modulators [17].

modulations. On the other hand, MRR modulators have small footprint and low power consumption, but the devices have small optical bandwidth and are very sensitive to process and thermal variations. The performance of the MRR modulators strongly depend on the quality factor (Q) of the device. High Q devices have very low link power penalty, small optical bandwidth and can allow for high device figure of merit (FOM is the ratio of extinction ratio with device insertion loss). But they suffer from low 3dB small signal bandwidth as the modulator is limited by the photon lifetime in the device. On the other hand, low Q device have high link power penalty, larger optical bandwidth (still significantly lower than MZI modulators) and lower FOM as compared to the high Q devices, but can be operated at high speeds. Therefore, MRR modulator has to compromise between low link power penalty and modulation speed. To illustrate this clearly, we summarize the key performance of MZI and MRR modulators in Table 1.3. Electro-absorption modulators (EAMs) exploiting the Franz-Keldysh effect (FKE) or quantum confined stark effect (QCSE) have been identified as possible candidates to bridge this gap between MZI and MRR modulator and to enable broad optical bandwidth and low power consumption in a single device. Due to the presence of a direct band gap at photon energies of 0.8 eV for undoped and unstrained Ge, it is an attractive material to realize EAMs. Such devices were alreade demonstrated in [74], but have significant room for improvement to enable 400 Gb/s Ethernet optical links. This will be elaborately motivated in Chapter 2.

1.3 Thesis motivation

In this thesis, we will address the following questions in an effort to realize advanced active-photonic devices based on Ge that can complement the existing Ge-photodetectors:

- Can Ge based devices such as Ge electro-absorption modulators and Ge laser diodes on Si get close enough to the performance of III-V based devices to become a viable replacement for the latter?

- Can the Ge platform be a technologically profitable platform for enabling future optical interconnect applications?

1.4 Awards and Publications

1.4.1 Awards

1. Best student paper award (Runner's up) at IEEE 12^{th} International Conference on Group IV Photonics (GFP) for the paper "Carrier Lifetime Assessment in Integrated Ge Waveguide Devices", Vancouver, Canada, 2015.

1.4.2 Patents Applications

1. C. Merckling, **S. A. Srinivasan**, J. Van Campenhout, M. Pantouvaki, I. Kulkova, *EP 16206840.7*, 2016, Patent Filed.

2. C. Merckling, **S. A. Srinivasan**, J. Van Campenhout, M. Pantouvaki, I. Kulkova, *US 15840779*, 2017, Patent Filed.

3. **S. A. Srinivasan**, J. Van Campenhout, *EP 17210498.6*, 2017, Patent Filed.

4. J. Van Campenhout, **S. A. Srinivasan**, Y. Shi, D. Van Thourhout, M. Pantouvaki, B. Kunert, *EP 17211015.7*, 2017, Patent Filed.

1.4.3 Publications in journals

1. **S. A. Srinivasan**, C. Porret, M. Pantouvaki, Y. Shimura, P. Geiregat, R. Loo, J. Van Campenhout, D. Van Thourhout, "Carrier scattering effects induced linewidth broadening in in-situ P-doped Ge layers on Si", *In review*.

2. J. Verbist, J. Lambrecht, M. Verplaetse, J. Van Kerrebrouck, **S. A. Srinivasan**, P. De Heyn, T. De Keulenaer, X. Yin, G. Torfs, J. Van Campenhout, G. Roelkens, J. Bauwelinck, "DAC-less and DSP-free 112 Gb/s PAM-4 Transmitter using Two Parallel Electro-Absorption Modulators", accepted for publication in *Journal of Lightwave Technology*, 2018.

3. J. Verbist, M. Verplaetse, **S. A. Srinivasan**, J. Van Kerrebrouck, P. De Heyn, P. Absil, T. De Keulenaer, R. Pierco, G. Torfs, X. Yin, J. Van Campenhout, G. Roelkens, J. Bauwelinck, "Real-Time 100-Gb/s NRZ and EDB Transmission with a GeSi Electro-Absorption Modulator for Short-Reach Optical Interconnects", accepted for publication in *Journal of Lightwave Technology*, 2017.

4. Y. Yamamoto, L. W. Nien, G. Capellini, I. Costina, M. A. Schubert, W. Seifert, **S. A. Srinivasn**, R. Loo, G. Scappucci, D. Sabbagh , A. Hesse, J. Murota, T. Schroeder, B. Tillack, “Photoluminescence of phosphorus atomic layer doped Ge grown on Si”, *IOP Semiconductor Science and Technology*, vol. 32, no. 10, 2017.

5. M. Pantouvaki, **S. A. Srinivasan**, Y. Ban, P. De Heyn, P. Verheyen, B. Snyder, M. Rakowski, J. De Coster, G. Lepage, H. Chen, N. Golshani, P. Absil, J. Van Campenhout, “Active Components for 50 Gb/s NRZ-OOK Optical Interconnects in a Silicon Photonics Platform”, *IEEE Journal of Lightwave Technology*, vol. 35, no. 4, 2017, **Invited**.

6. **S. A. Srinivasan**, M. Pantouvaki, P. Verheyen, G. Lepage, P. Absil, J. Van Campenhout, D. Van Thourhout, “Extraction of carrier lifetime in Ge waveguides using pump probe spectroscopy”, *Applied Physics Letters*, vol. 108, no. 21, 2016.

7. Y. Shimura, **S. A. Srinivasan**, R. Loo, “Design requirements for group-IV laser based on fully strained Ge1-xSnx embedded in partially relaxed Si1-y-zGeySnz buffer layers”, *ECS Journal of Solid State Science and Technology*, vol. 5, no. 5, 2016.

8. Y. Shimura, **S. A. Srinivasan**, D. Van Thourhout, R. Van Deun, M. Pantouvaki, J. Van Campenhout, R. Loo,“Enhanced active P doping by using high order Ge precursors leading to intense photoluminescence”, *Thin Solid Films*,vol. 602, 2016.

9. **S. A. Srinivasan**, M. Pantouvaki, S. Gupta, H. Chen, P. Verheyen, G. lepage, G. Roelkens, K. Saraswat, D. Van Thourhout, P. Absil, J. Van Campenhout,“56 Gb/s Germanium Waveguide Electro-Absorption Modulator”, *Journal of Lightwave Technology*, vol. 34, no. 2,2016.

1.4.4 Publications in conferences

1. **S. A. Srinivasan**, C. Porret, E. Vissers, P. Geiregat, D. Van Thourhout, R. Loo, M. Pantouvaki, J. Van Campenhout, “High-contrast quantum-confined Stark effect in Ge/SiGe quantum well stacks on Si with ultra-thin buffer layers”, submitted to *CLEO Pacific Rim*, Hong Kong, 2018.

2. J. Van Campenhout, Y. Ban, P. De Heyn, **S. A. Srinivasan**, J. De Coster, S. lardenois, B. Snyder, S. Balakrishnan, G. Lepage, N. Golshani, S. Janssen, A. Lesniewska, K. Croes, A. Miller, P. Verheyen, M. Pantouvaki, P. Absil, “Silicon Photonics for 56G NRZ Optical Interconnects”, *Optical Fiber Communication Conference*, United States of America, 2018, **Invited**.

3. J. Verbist, M. Verplaetse, J. Lambrecht, **S. A. Srinivasan**, P. De Heyn, T. De Keulenaer, R. Pierco, A. Vyncke, P. Absil, X. Yin, G. Torfs, J. Van Campenhout, G. Roelkens, J. Bauwelinck, “100 Gb/s DAC-less and DSP-free Transmitters using GeSi EAMs for Short-Reach Optical Interconnects”, *Optical Fiber Communication Conference*, United States of America, 2018, **Invited**.
4. E. Elfiky, P. D. Heyn, M. Morsy-Osman, **S. A. Srinivasan**, A. Samani, M. Pantouvaki, M. Sowailem, J. Van Campenhout, D. Plant, “112 Gb/s PAM4 Transmission over 2 km SMF Using a C-band GeSi Electro-Absorption Modulator ”, accepted for *Optical Fiber Communication Conference*, United States of America, 2018.
5. P. Absil, K. Croes, A. Lesniewska, P. De Heyn, Y. Ban, B. Snyder, J. De Coster, F. Fodor, V. Simons, S. Balakrishnan, G. Lepage, N. Golshani, S. Lardenois, **S. A. Srinivasan**, H. Chen, W. Vanherle, R. Loo, R. Boufadil, M. Detalle, A. Miller, P. Verheyen, M. Pantouvaki, J. Van Campenhout, “Reliable 50Gb/s Silicon Photonics Platform for Next-Generation Data Center Optical Interconnects”, *63rd International Electron Devices Meeting*, United States, 2017, **Invited**.
6. J. Verbist, J. Lambrecht, M. Verplaetse, J. Van Kerrebrouck, **S. A. Srinivasan**, P. De Heyn, T. De Keulenaer, X. Yin, J. Van Campenhout, G. Roelkens, J. Bauwelinck, “DAC-less and DSP-free PAM-4 Transmitter at 112 Gb/s with Two Parallel GeSi Electro-Absorption Modulators”, *European Conference on Optical Communication*, Sweden, 2017, **Post Deadline Paper**.
7. **S. A. Srinivasan**, C. Porret, M. Pantouvaki, Y. Shimura, P. Geiregat, R. Loo, J. Van Campenhout, D. Van Thourhout, “Analysis of Homogeneous Broadening in n-type doped Ge layers on Si for laser applications”, *IEEE Photonics Conference*, Florida, United States of America, 2017.
8. **S. A. Srinivasan**, C. Porret, M. Pantouvaki, Y. Shimura, P. Geiregat, R. Loo, J. Van Campenhout, D. Van Thourhout, “Reduction of Optical Bleaching in Phosphorus doped Ge layer on Si”, *IEEE Group IV Photonics Conference*, Berlin, Germany, 2017.
9. J. Verbist, M. Verplaetse, **S. A. Srinivasan**, P. De Heyn, T. De Keulenaer, R. Vaernewyck, R. Pierco, A. Vyncke, P. Verheyen, S. Balakrishnan, G. Lepage, M. Pantouvaki, P. Absil, X. Yin, G. Roelkens, G. Torfs, J. Van Campenhout, J. Bauwelinck, “Real-Time 100 Gb/s NRZ-OOK Transmission with a Silicon Photonics GeSi Electro-Absorption Modulator”, *IEEE Optical Interconnects Conference*, Santa Fe, United States of America,2017.
10. J. Verbist, M. Verplaetse, **S. A. Srinivasan**, P. De Heyn, T. De Keulenaer, R. Pierco, R. Vaernewyck, A. Vyncke, P. Absil, G. Torfs, X. Yin, G. Roelkens,

J. Van Campenhout, J. Bauwelinck, “First Real-Time 100-Gb/s NRZ-OOK Transmission over 2 km with a Silicon Photonic Electro-Absorption Modulator”,*Optical Fiber Communication Conference*, Los Angeles, United States of America,2017, **Post Deadline Paper**.

11. P. De Heyn, V. Kopp, **S. A. Srinivasan**, P. Verheyen, J. Park, M. S. Wlodawski, J. Singer, D. Neugroschl, B. Snyder, S. Balakrishnan, G. Lepage, M. Pantouvaki, P. Absil, J. Van Campenhout, “Ultra-Dense 16x56 Gb/s NRZ GeSi EAM-PD Arrays Coupled to Multicore Fiber for Short-Reach 896 Gb/s Optical Links”,*Optical Fiber Communication Conference*, Los Angeles, United States of America, 2017, **Top Scoring Paper**.

12. P. De Heyn, **S. A. Srinivasan**, P. Verheyen, R. Loo, I. De Wolf, S. Balakrishnan, G. Lepage, D. Van Thourhout, M. Pantouvaki, P. Absil, J. Van Campenhout, “High-Speed Germanium-Based Waveguide Electro-Absorption Modulator”, *21st Optoelectronics and Communications Conference/International Conference on Photonics in Switching*, Nigata, Japan,2016, **Invited**.

13. **S. A. Srinivasan**, M. Pantouvaki, Y. Shimura, C. Porret, R. Van Deun, R. Loo, D. Van Thourhout, J. Van Campenhout, “Laser Annealed in-situ P-doped Ge for on-chip laser source applications”, *SPIE Photonics Europe*, Brussels, Belgium,2016.

14. **S. A. Srinivasan**, P. Verheyen, R. Loo, I. De Wolf, M. Pantouvaki, G. Lepage, S. Balakrishnan, W. Vanherle, P. Absil, J. Van Campenhout, “50 Gb/s C-band GeSi Waveguide Electro-Absorption Modulator”, *Optical Fiber Communication Conference*, Anaheim, United States of America,2016.

15. M. Pantouvaki, P. De Heyn, M. Rakowski, P. Verheyen, B. Snyder, **S. A. Srinivasan**, H. Chen, J. De Coster, G. Lepage, P. Absil, J. Van Campenhout, “50 Gb/s Silicon Photonics Platform for Short-Reach Optical Interconnects”, *Optical Fiber Communication Conference*, Anaheim, United States of America, 2016, **Invited**.

16. P. Absil, P. De Heyn, H. Chen, **S. A. Srinivasan**, P. Verheyen, S. Balakrishnan, G. Lepage, M. Pantouvaki, J. De Coster, G. Roelkens, D. Van Thourhout, J. Van Campenhout, “Isipp-200: a silicon photonics platform supporting optical data rates beyond 50 Gb/s”, *SPIE Photonics West*, San Francisco, United States of America,2016, **Invited**.

17. Y Shimura, **S. A. Srinivasan**, D. Van Thourhout, R. Van Deun, M. Pantouvaki, J. Van Campenhout, R. Loo, “Enhanced Ge Photoluminescence by increasing the active P doping using high order Ge precursors at lower growth temperatuers”, *E-MRS Fall Meeting and Exhibit*, Warsaw, Poland, 2015.

18. **S. A. Srinivasan**, M. Pantouvaki, P. Verheyen, G. Lepage, P. Absil, J. Van Campenhout, D. Van Thourhout, "Carrier Lifetime Assessment in Integrated Ge Waveguide Devices", *12th International Conference on Group IV Photonics (GFP)*, Vancouver, Canada, 2015.

19. Y. Shimura, **S. A. Srinivasan**, D. Van Thourhout, R. Van Deun, M. Pantouvaki, J. Van Campenhout, R. Loo, "Low temperature in-situ P-doped Ge epitaxy using Ge2H6 in view of optical applications", *9th International Conference On Silicon Epitaxy And Heterostructures*, Montréal, Canada, 2015.

20. S. Gupta, **S. A. Srinivasan**, M. Pantouvaki, H. Chen, P. Verheyen, G. Lepage, D. Van Thourhout, G. Roelkens, K. Saraswat, P. Absil, J. Van Campenhout, "50 GHz Ge Waveguide Electro-Absorption Modulator Integrated in a 220nm SOI Photonics Platform", *Optical Fiber Communication Conference*, Los Angeles, United States of America, 2015, **Top Scoring Paper**.

References

[1] Christoforos Kachris and Ioannis Tomkos. *A survey on optical interconnects for data centers*. IEEE Communications Surveys & Tutorials, 14(4):1021–1036, 2012.

[2] Cisco Global Cloud Index. *Forecast and Methodology, 2015-2020 White Paper*, 2016.

[3] Mehdi Asghari and Ashok V Krishnamoorthy. *Silicon photonics: Energy-efficient communication*. Nature photonics, 5(5):268–270, 2011.

[4] The Independent. *Global warming: Data centres to consume three times as much energy in next decade, experts warn*, 2016. Accessed: 2016-01-23.

[5] Ashok V Krishnamoorthy, Keith W Goossen, William Jan, Xuezhe Zheng, Ron Ho, Guoliang Li, Richard Rozier, Frankie Liu, Dinesh Patil, Jon Lexau, et al. *Progress in low-power switched optical interconnects*. IEEE Journal of selected topics in quantum electronics, 17(2):357–376, 2011.

[6] Xuezhe Zheng, Shiyun Lin, Ying Luo, Jin Yao, Guoliang Li, Stevan S Djordjevic, Jin-Hyoung Lee, Hiren D Thacker, Ivan Shubin, Kannan Raj, et al. *Efficient WDM laser sources towards terabyte/s silicon photonic interconnects*. Journal of Lightwave Technology, 31(24):4142–4154, 2013.

[7] Ashok V Krishnamoorthy, Hiren D Thacker, Ola Torudbakken, Shimon Müller, Arvind Srinivasan, Patrick J Decker, Hans Opheim, John E Cunningham, Ivan Shubin, Xuezhe Zheng, et al. *From Chip to Cloud: Opti-*

cal Interconnects in Engineered Systems. Journal of Lightwave Technology, 35(15):3103–3115, 2017.

[8] Herb Schwetman, Avadh Patel, Leick Robinson, Xuezhe Zheng, Alan Wood, and Ashok V Krishnamoorthy. *An Energy-Efficient Optical Interconnect Architecture for Bandwidth-Balanced Systems*. Journal of Lightwave Technology, 34(12):2905–2919, 2016.

[9] Jun Li, Xuezhe Zheng, Ashok V Krishnamoorthy, and James F Buckwalter. *Scaling trends for picojoule-per-bit WDM photonic interconnects in CMOS SOI and FinFET processes*. Journal of Lightwave Technology, 34(11):2730–2742, 2016.

[10] Silicon Microphotonics. *Microphotonics: Hardware for the Information Age*. 2005.

[11] Robert Blum. *Silicon photonics and the future of optical connectivity in the data center*. In ECOC Market Focus, 2016.

[12] Brad Booth and Tom Issenhuth. *Global Networking Services: Objectives to Support Cloud Scale Data Center Design*, 2013.

[13] Thomas Liljeberg. *Silicon photonics and the future of optical connectivity in the data center*. In IEEE Optical Interconnects Conference (OI), 2017, pages 1–2. IEEE, 2017.

[14] `http://www.luxtera.com/luxtera/products`.

[15] `http://www.mellanox.com/products/interconnect/ethernet-optical-transceivers.php`.

[16] `https://www.intel.com/content/www/us/en/architecture-and-technology/silicon-photonics/silicon-photonics-overview.html`.

[17] M Pantouvaki, SA Srinivasan, Y Ban, P De Heyn, P Verheyen, G Lepage, H Chen, J De Coster, N Golshani, S Balakrishnan, et al. *Active Components for 50 Gb/s NRZ-OOK Optical Interconnects in a Silicon Photonics Platform*. Journal of Lightwave Technology, 35(4):631–638, 2017.

[18] Michal Rakowski. *Silicon Photonics Platform for 50G Optical Interconnects*. In Photonics Summit and Workshop 2017, 2017.

[19] X Leijtens. *JePPIX: the platform for Indium Phosphide-based photonics*. IET optoelectronics, 5(5):202–206, 2011.

[20] Kerstin Wörhoff, René G Heideman, Arne Leinse, and Marcel Hoekman. *TriPleX: a versatile dielectric photonic platform*. Advanced Optical Technologies, 4(2):189–207, 2015.

[21] Roel Baets, Ananth Z Subramanian, Stéphane Clemmen, Bart Kuyken, Peter Bienstman, Nicolas Le Thomas, Günther Roelkens, Dries Van Thourhout, Philippe Helin, and Simone Severi. *Silicon Photonics: silicon nitride versus silicon-on-insulator*. In Optical Fiber Communications Conference and Exhibition (OFC), 2016, pages 1–3. IEEE, 2016.

[22] Abdul Rahim, Eva Ryckeboer, Ananth Z Subramanian, Stéphane Clemmen, Bart Kuyken, Ashim Dhakal, Ali Raza, Artur Hermans, Muhammad Muneeb, Sören Dhoore, et al. *Expanding the Silicon Photonics Portfolio With Silicon Nitride Photonic Integrated Circuits*. Journal of Lightwave Technology, 35(4):639–649, 2017.

[23] Philippe P Absil, Peter Verheyen, Peter De Heyn, Marianna Pantouvaki, Guy Lepage, Jeroen De Coster, and Joris Van Campenhout. *Silicon photonics integrated circuits: a manufacturing platform for high density, low power optical I/Os*. Optics express, 23(7):9369–9378, 2015.

[24] Dirk Taillaert, Frederik Van Laere, Melanie Ayre, Wim Bogaerts, Dries Van Thourhout, Peter Bienstman, and Roel Baets. *Grating couplers for coupling between optical fibers and nanophotonic waveguides*. Japanese Journal of Applied Physics, 45(8R):6071, 2006.

[25] Peter De Heyn, Jeroen De Coster, Peter Verheyen, Guy Lepage, Marianna Pantouvaki, Philippe Absil, Wim Bogaerts, Joris Van Campenhout, and Dries Van Thourhout. *Fabrication-tolerant four-channel wavelength-division-multiplexing filter based on collectively tuned Si microrings*. Journal of Lightwave Technology, 31(16):3085–3092, 2013.

[26] Peter De Heyn, Jeroen De Coster, Peter Verheyen, Guy Lepage, Marianna Pantouvaki, Philippe Absil, Wim Bogaerts, Dries Van Thourhout, and Joris Van Campenhout. *Polarization-insensitive 5× 20Gb/s WDM Ge receiver using compact Si ring filters with collective thermal tuning*. In Optical Fiber Communications Conference and Exhibition (OFC), 2014, pages 1–3. IEEE, 2014.

[27] Bradley W Snyder and Peter A O'Brien. *Developments in packaging and integration for silicon photonics*. In Reliability, Packaging, Testing, and Characterization of MOEMS/MEMS and Nanodevices XII, volume 8614, page 86140D. International Society for Optics and Photonics, 2013.

[28] M Pantouvaki, P Verheyen, J De Coster, G Lepage, P Absil, and J Van Campenhout. *56Gb/s ring modulator on a 300mm silicon photonics platform*. In Optical Communication (ECOC), 2015 European Conference on, pages 1–3. IEEE, 2015.

[29] Peter J Winzer. *Scaling optical fiber networks: Challenges and solutions*. Optics and Photonics News, 26(3):28–35, 2015.

[30] Michal Rakowski, Marianna Pantouvaki, Peter De Heyn, Peter Verheyen, Mark Ingels, Hongtao Chen, Jeroen De Coster, Guy Lepage, Brad Snyder, Kristin De Meyer, et al. *A 4x20Gb/s WDM ring-based hybrid CMOS silicon photonics transceiver*. In 2015 IEEE International Solid-State Circuits Conference (ISSCC 2015), pages 408–410, 2015.

[31] Di Liang and John E Bowers. *Recent progress in lasers on silicon*. Nature photonics, 4(8):511–517, 2010.

[32] Zhiping Zhou, Bing Yin, and Jurgen Michel. *On-chip light sources for silicon photonics*. Light: Science & Applications, 4(11):e358, 2015.

[33] Zhechao Wang, Amin Abbasi, Utsav Dave, Andreas Groote, Sulakshna Kumari, Bernadette Kunert, Clement Merckling, Marianna Pantouvaki, Yuting Shi, Bin Tian, et al. *Novel light source integration approaches for silicon photonics*. Laser & Photonics Reviews, 11(4), 2017.

[34] Ozdal Boyraz and Bahram Jalali. *Demonstration of a silicon Raman laser*. Optics express, 12(21):5269–5273, 2004.

[35] Haisheng Rong, Ansheng Liu, Richard Jones, Oded Cohen, Dani Hak, Remus Nicolaescu, Alexander Fang, and Mario Paniccia. *An all-silicon Raman laser*. Nature, 433(7023):292–294, 2005.

[36] Haisheng Rong, Shengbo Xu, Ying-Hao Kuo, Vanessa Sih, Oded Cohen, Omri Raday, and Mario Paniccia. *Low-threshold continuous-wave Raman silicon laser*. Nature Photonics, 1(4):232–237, 2007.

[37] J Sun, Thomas N Adam, Gerald Leake, Douglas Coolbaugh, Jonathon DB Bradley, E Shah Hosseini, Michael R Watts, et al. *C-and L-band erbium-doped waveguide lasers with wafer-scale silicon nitride cavities*. Optics letters, 38(11):1760–1762, 2013.

[38] Ehsan Shah Hosseini, Jonathan DB Bradley, Jie Sun, Gerald Leake, Thomas N Adam, Douglas D Coolbaugh, Michael R Watts, et al. *CMOS-compatible 75 mW erbium-doped distributed feedback laser*. Optics letters, 39(11):3106–3109, 2014.

[39] Weiqiang Xie, Thilo Stöferle, Gabriele Rainò, Tangi Aubert, Suzanne Bisschop, Yunpeng Zhu, Rainer F Mahrt, Pieter Geiregat, Edouard Brainis, Zeger Hens, et al. *On-Chip Integrated Quantum-Dot–Silicon-Nitride Microdisk Lasers*. Advanced Materials, 29(16), 2017.

[40] Yunpeng Zhu, Weiqiang Xie, Suzanne Bisschop, Tangi Aubert, Edouard Brainis, Pieter Geiregat, Zeger Hens, and Dries Van Thourhout. *On-chip single-mode distributed feedback colloidal quantum dot laser under nanosecond pumping*. ACS Photonics, 4(10):2446–2452, 2017.

[41] Jin Hyoung Lee, Ivan Shubin, Jin Yao, Justin Bickford, Ying Luo, Shiyun Lin, Stevan S Djordjevic, Hiren D Thacker, John E Cunningham, Kannan Raj, et al. *High power and widely tunable Si hybrid external-cavity laser for power efficient Si photonics WDM links*. Optics express, 22(7):7678–7685, 2014.

[42] Jock Bovington, Xuezhe Zheng, Stevan S Djordjevic, Ivan Shubin, Jin-Hyoung Lee, Shiyun Lin, Ying Luo, Jin Yao, Daniel Y Lee, Kannan Raj, et al. *III–V/Si Vernier-Ring Comb Lasers (VRCLs)*. IEEE Journal of Selected Topics in Quantum Electronics, 23(3):1–8, 2017.

[43] Bradley Snyder, Brian Corbett, and Peter OBrien. *Hybrid integration of the wavelength-tunable laser with a silicon photonic integrated circuit*. Journal of Lightwave Technology, 31(24):3934–3942, 2013.

[44] Günther Roelkens, Liu Liu, Di Liang, Richard Jones, Alexander Fang, Brian Koch, and John Bowers. *III-V/silicon photonics for on-chip and intra-chip optical interconnects*. Laser & Photonics Reviews, 4(6):751–779, 2010.

[45] Gunther Roelkens, Amin Abassi, Paolo Cardile, Utsav Dave, Andreas De Groote, Yannick De Koninck, Sören Dhoore, Xin Fu, Alban Gassenq, Nannicha Hattasan, et al. *III-V-on-silicon photonic devices for optical communication and sensing*. In Photonics, volume 2, pages 969–1004. Multidisciplinary Digital Publishing Institute, 2015.

[46] Tao Hong, Guang-Zhao Ran, Ting Chen, Jiao-Qing Pan, Wei-Xi Chen, Yang Wang, Yuan-Bing Cheng, Song Liang, Ling-Juan Zhao, Lu-Qiao Yin, et al. *A selective-area metal bonding InGaAsP–Si laser*. IEEE Photonics Technology Letters, 22(15):1141–1143, 2010.

[47] Alexander W Fang, Hyundai Park, Oded Cohen, Richard Jones, Mario J Paniccia, and John E Bowers. *Electrically pumped hybrid AlGaInAs-silicon evanescent laser*. Optics express, 14(20):9203–9210, 2006.

[48] Shahram Keyvaninia, Steven Verstuyft, Liesbet Van Landschoot, F Lelarge, G-H Duan, S Messaoudene, JM Fedeli, T De Vries, B Smalbrugge, EJ Geluk, et al. *Heterogeneously integrated III-V/silicon distributed feedback lasers*. Optics letters, 38(24):5434–5437, 2013.

[49] Alan Y Liu, Sudharsanan Srinivasan, Justin Norman, Arthur C Gossard, and John E Bowers. *Quantum dot lasers for silicon photonics*. Photonics Research, 3(5):B1–B9, 2015.

[50] Daehwan Jung, Justin Norman, MJ Kennedy, Chen Shang, Bongki Shin, Yating Wan, Arthur C Gossard, and John E Bowers. *High efficiency low threshold current 1.3 μ m InAs quantum dot lasers on on-axis (001) GaP/Si*. Applied Physics Letters, 111(12):122107, 2017.

[51] Yating Wan, Justin Norman, Qiang Li, MJ Kennedy, Di Liang, Chong Zhang, Duanni Huang, Zeyu Zhang, Alan Y Liu, Alfredo Torres, et al. *1.3 μm submilliamp threshold quantum dot micro-lasers on Si*. Optica, 4(8):940–944, 2017.

[52] Siming Chen, Wei Li, Jiang Wu, Qi Jiang, Mingchu Tang, Samuel Shutts, Stella N Elliott, Angela Sobiesierski, Alwyn J Seeds, Ian Ross, et al. *Electrically pumped continuous-wave III–V quantum dot lasers on silicon*. Nature Photonics, 10(5):307–311, 2016.

[53] Daehwan Jung, Zeyu Zhang, Justin Norman, Robert Herrick, MJ Kennedy, Pari Patel, Katherine Turnlund, Catherine Jan, Yating Wan, Arthur Gossard, et al. *Highly reliable low threshold InAs quantum dot lasers on on-axis (001) Si with 87% injection efficiency*. ACS Photonics, 2017.

[54] Clement Merckling, Ziyang Liu, Mark Hsu, Samiul Hasan, Sijia Jiang, Salim El Kazzi, Guillaume Boccardi, Niamh Waldron, Zhechao Wang, Bin Tian, et al. *III-V Selective Area Growth and Epitaxial Functional Oxides on Si: From Electronic to Photonic Devices*. ECS Transactions, 72(2):59–69, 2016.

[55] Yuting Shi, Zhechao Wang, Joris Van Campenhout, Marianna Pantouvaki, Weiming Guo, Bernardette Kunert, and Dries Van Thourhout. *Optical pumped InGaAs/GaAs nano-ridge laser epitaxially grown on a standard 300-mm Si wafer*. Optica, 4(12):1468–1473, 2017.

[56] Zhechao Wang, Bin Tian, Marianna Pantouvaki, Weiming Guo, Philippe Absil, Joris Van Campenhout, Clement Merckling, and Dries Van Thourhout. *Room-temperature InP distributed feedback laser array directly grown on silicon*. Nature Photonics, 9(12):837–842, 2015.

[57] B Kunert, W Guo, Y Mols, Bin Tian, Zhechao Wang, Yuting Shi, Dries Van Thourhout, M Pantouvaki, J Van Campenhout, R Langer, et al. *III/V nano ridge structures for optical applications on patterned 300 mm silicon substrate*. Applied Physics Letters, 109(9):091101, 2016.

[58] Bin Tian, Zhechao Wang, Marianna Pantouvaki, Philippe Absil, Joris Van Campenhout, Clement Merckling, and Dries Van Thourhout. *Room Temperature O-band DFB Laser Array Directly Grown on (001) Silicon*. Nano letters, 17(1):559–564, 2016.

[59] Gang Wang, Frederik E Leys, Laurent Souriau, Roger Loo, Matty Caymax, David P Brunco, Jef Geypen, Hugo Bender, Marc Meuris, Wilfried Vandervorst, et al. *Selective epitaxial growth of germanium on Si wafers with shallow trench isolation: an approach for Ge virtual substrates*. ECS Transactions, 16(10):829–836, 2008.

[60] Roger Loo, Andriy Yakovitch Hikavyy, Liesbeth Witters, Andreas Schulze, Hiroaki Arimura, Daire Cott, Jerome Mitard, Clement Porret, Hans Mertens, Paul Ryan, et al. *Processing Technologies for Advanced Ge Devices*. ECS Journal of Solid State Science and Technology, 6(1):P14–P20, 2017.

[61] Richard Geiger, Thomas Zabel, and Hans Sigg. *Group IV direct band gap photonics: methods, challenges, and opportunities*. Photonic Integration and Photonics-Electronics Convergence on Silicon Platform, page 81, 2015.

[62] Richard Geiger. *Direct Band Gap Germanium for Si-compatible Lasing*. PhD thesis, 2016.

[63] Jifeng Liu, Xiaochen Sun, Rodolfo Camacho-Aguilera, Lionel C Kimerling, and Jurgen Michel. *Ge-on-Si laser operating at room temperature*. Optics letters, 35(5):679–681, 2010.

[64] Rodolfo E Camacho-Aguilera, Yan Cai, Neil Patel, Jonathan T Bessette, Marco Romagnoli, Lionel C Kimerling, and Jurgen Michel. *An electrically pumped germanium laser*. Optics express, 20(10):11316–11320, 2012.

[65] Roman Koerner, Michael Oehme, Martin Gollhofer, Marc Schmid, Konrad Kostecki, Stefan Bechler, Daniel Widmann, Erich Kasper, and Joerg Schulze. *Electrically pumped lasing from Ge Fabry-Perot resonators on Si*. Optics express, 23(11):14815–14822, 2015.

[66] Sattar Al-Kabi, Seyed Amir Ghetmiri, Joe Margetis, Thach Pham, Yiyin Zhou, Wei Dou, Bria Collier, Randy Quinde, Wei Du, Aboozar Mosleh, et al. *An optically pumped 2.5 μ m GeSn laser on Si operating at 110 K*. Applied Physics Letters, 109(17):171105, 2016.

[67] Stephan Wirths, Richard Geiger, N Von Den Driesch, G Mussler, T Stoica, S Mantl, Z Ikonic, Ml Luysberg, S Chiussi, JM Hartmann, et al. *Lasing in direct-bandgap GeSn alloy grown on Si.* Nature photonics, 9(2):88, 2015.

[68] Daniela Stange, Stephan Wirths, Richard Geiger, Christian Schulte-Braucks, Bahareh Marzban, Nils von den Driesch, Gregor Mussler, Thomas Zabel, Toma Stoica, Jean-Michel Hartmann, et al. *Optically pumped GeSn microdisk lasers on Si.* ACS Photonics, 3(7):1279–1285, 2016.

[69] Shuyu Bao, Daeik Kim, Chibuzo Onwukaeme, Shashank Gupta, Krishna Saraswat, Kwang Hong Lee, Yeji Kim, Dabin Min, Yongduck Jung, Haodong Qiu, et al. *Low-threshold optically pumped lasing in highly strained germanium nanowires.* Nature communications, 8(1):1845, 2017.

[70] V. Reboud, A. Gassenq, N. Pauc, J. Aubin, L. Milord, Q. M. Thai, M. Bertrand, K. Guilloy, D. Rouchon, J. Rothman, T. Zabel, F. Armand Pilon, H. Sigg, A. Chelnokov, J. M. Hartmann, and V. Calvo. *Optically pumped GeSn micro-disks with 16% Sn lasing at 3.1 m up to 180K.* Applied Physics Letters, 111(9):092101, 2017.

[71] Joe Margetis, Sattar Al-Kabi, Wei Du, Wei Dou, Yiyin Zhou, Thach Pham, Perry Grant, Seyed Ghetmiri, Aboozar Mosleh, Baohua Li, et al. *Si-based GeSn lasers with wavelength coverage of 2 to 3* μ*m and operating temperatures up to 180 K.* ACS Photonics, 2017.

[72] Martyna Grydlik, Florian Hackl, Heiko Groiss, Martin Glaser, Alma Halilovic, Thomas Fromherz, Wolfgang Jantsch, Friedrich Schaffler, and Moritz Brehm. *Lasing from glassy Ge quantum dots in crystalline Si.* ACS photonics, 3(2):298–303, 2016.

[73] Ling Liao, Dean Samara-Rubio, Michael Morse, Ansheng Liu, Dexter Hodge, Doron Rubin, Ulrich D Keil, and Thorkild Franck. *High speed silicon Mach-Zehnder modulator.* Optics Express, 13(8):3129–3135, 2005.

[74] Papichaya Chaisakul, Delphine Marris-Morini, Mohamed-Said Rouifed, Jacopo Frigerio, Daniel Chrastina, Jean-René Coudevylle, Xavier Le Roux, Samson Edmond, Giovanni Isella, and Laurent Vivien. *Recent progress in GeSi electro-absorption modulators.* Science and technology of advanced materials, 15(1):014601, 2013.

2

Prior art in Germanium Photonics

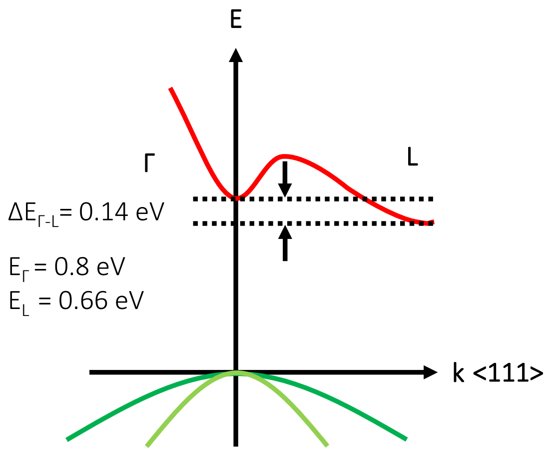

Figure 2.1: Schematic representation of the band structure of undoped Ge

Germanium is an attractive material for the electronics industry due to its low electron transverse effective mass and hole effective mass, making it an attractive alternative for future high performance nanoscale Metal-Oxide Semiconductor

Field-Effect Transistors (MOSFETs) [1]. Inspite of the lattice mismatch between Ge and Si, significant progress has been made to grow Ge on Si with low threading dislocation densities [2, 3]. Fig. 2.1 shows the band structure of undoped and unstrained Ge where the direct band gap is located at 0.8 eV. This allows the material to interact with light around 1550 nm, which is compatible with the C- band of fiber optic communication wavelength, to realize devices such as light sources and electro-absorption modulators for the transmitter module and photodetectors for the receiver module in an optical communication link. In this chapter, we will review the current state of the art with respect to Ge based light sources and electro absorption modulators and present an outline for this thesis.

2.1 Germanium on Silicon light emitter

2.1.1 Requirements for efficient light emission from Ge

Even though Ge has a direct band gap at 0.8 eV, it is intrinsically an indirect band gap material due to the presence of a L conduction band valley located $\sim$0.14 eV below the Γ conduction band valley. This energy difference of 0.14 eV makes it an inefficient light emitter as a majority of externally injected electrons will occupy the lower energy L conduction valley. Electrons located at the L conduction valley can recombine only with a hole with the assistance of a phonon, where the recombination rate to emit a photon is very low. On the other hand, electrons located at the Γ conduction valley can recombine at higher recombination rate with a hole. Therefore, by making Ge a direct or pseudo direct band gap material, we increase the carrier recombination rate from the Γ conduction valley and make an energy efficient light emitter.

Converting from a fundamentally indirect band gap material to a direct band gap material is possible by introducing tensile strain (uniaxial strain along the [100] crystal orientation or biaxial tensile strain in the (001) plane) or alloying Ge with Sn [4, 5]. Both approaches reduce the band gap in Ge, whereby the band gap at the direct Γ valley reduces at a higher rate than at the indirect L valley. Beyond a certain critical point, where the Γ valley surpasses the indirect band to become the lowest conduction band energy in highly strained Ge or GeSn. This phenomena is schematically shown in Fig. 2.2. The impact of strain and Sn concentration on the band structure are typically modelled using model-solid theory where the deformation potentials, Vergard's law and bowing parameters used are validated with experimental results [6–9]. For example, Ge$_{1-x}$Sn$_x$ with a hydro-static strain of ϵ_{xx}, ϵ_{yy} and ϵ_{zz} will have an energy shift of:

$$\Delta E_{ci} = \alpha_{ci}\big(\epsilon_{xx} + \epsilon_{yy} + \epsilon_{zz}\big) \tag{2.1}$$

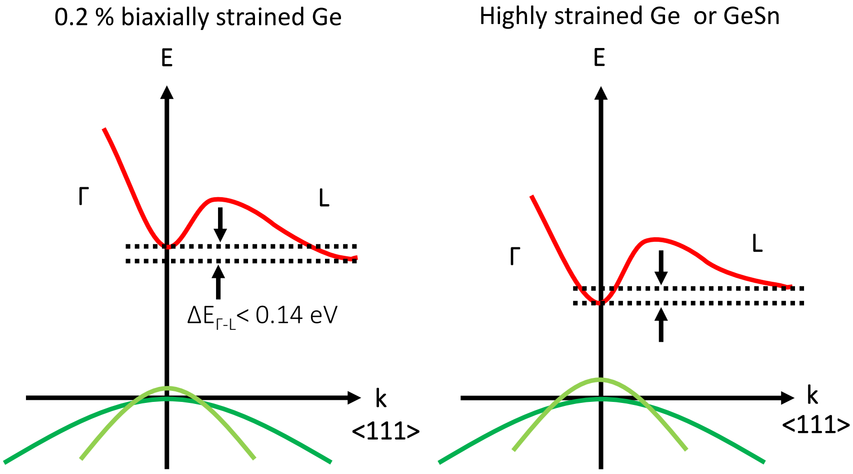

Figure 2.2: Schematic representation of the band structure of strained Ge and GeSn. Introducing tensile strain in Ge or alloying it with Sn modifies the band structure such that the band gap associated with the Γ conduction valley reduces at a faster rate compared to the indirect L conduction valley, as schematically shown here when compared to undoped and unstrained Ge in Fig. 2.1.

$$\Delta E_v = \alpha_v\left(\epsilon_{xx} + \epsilon_{yy} + \epsilon_{zz}\right) \tag{2.2}$$

In the above 2 equations, α_{ci} and α_v represent the hydro-static deformation potential and the subscript i denotes either the conduction band Γ or L valley. When the strain is applied along the [100] or [111] directions, then the valence band ends up splitting as represented in Eq. 2.2.

$$\Delta E_{v,lh} = -\frac{1}{6}\Delta_\circ + \frac{1}{4}\delta E + \frac{1}{2}\sqrt{\Delta_\circ^2 + \Delta_\circ \delta E + \frac{9}{4}\left(\delta E\right)^2} \tag{2.3}$$

$$\Delta E_{v,hh} = \frac{1}{3}\Delta_\circ - \frac{1}{2}\delta E \tag{2.4}$$

$$\Delta E_{v,so} = -\frac{1}{6}\Delta_\circ - \frac{1}{4}\delta E + \frac{1}{2}\sqrt{\Delta_\circ^2 + \Delta_\circ \delta E + \frac{9}{4}\left(\delta E\right)^2} \tag{2.5}$$

where $\Delta_\circ$ denotes spin-orbit splitting and δE is $2b_s\left(\epsilon_\perp - \epsilon_\parallel\right)$ for strain along the directions [001], with b_s denoting the shear deformation potential. These coefficients used in Eq. 2.1 to Eq. 2.5 depend on the amount of Sn present in the alloy and are typically obtained by linear interpolation as in [6]. Using this method, $\sim$4.5% of uniaxial tensile strain along the [100] crystal orientation, $\sim$1.6-2% biaxial tensile strain (001) or a Sn concentration of $\sim 9\%$ in an unstrained layer will result in a direct band gap material, as obtained using multi-band $k.p$ theory [6, 10, 11]. These critical points were experimentally validated in [12] and [13] with the help of temperature dependent photoluminescence (PL) spectroscopy, where at low temperatures, the majority of photo-excited carriers occupy the low lying Γ conduction valley of direct band gap Ge/GeSn, resulting in higher PL intensity due to Fermi-Dirac statistics. Using this approach, several research groups around the world have demonstrated an optically pumped GeSn laser at wavelengths > 2 μm [13–16].

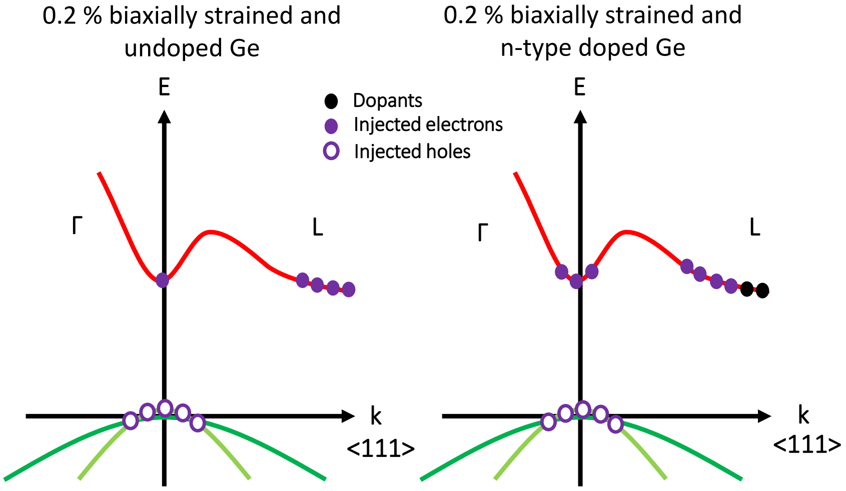

Figure 2.3: Schematic representation of the carrier statistics in undoped and n-type doped Ge.

Direct band gap Ge or GeSn have peak PL emission at wavelengths > 2 μm and are therefore not compatible with conventional fiber optic communication wavelengths. An alternatively way is to make Ge a pseudo direct band gap material by doping it with n-type dopants. The majority of dopant associated electrons will occupy the indirect L conduction valley shifting the Fermi level closer to the conduction band. As a result, the Γ conduction valley will have a higher concentration of excess injected electrons, schematically shown in Fig. 2.3. In order to illustrate this more accurately, the carrier statistics are modelled using Eq. 2.6 and Eq. 2.7 which estimates the location of the Fermi level as a function of the carrier

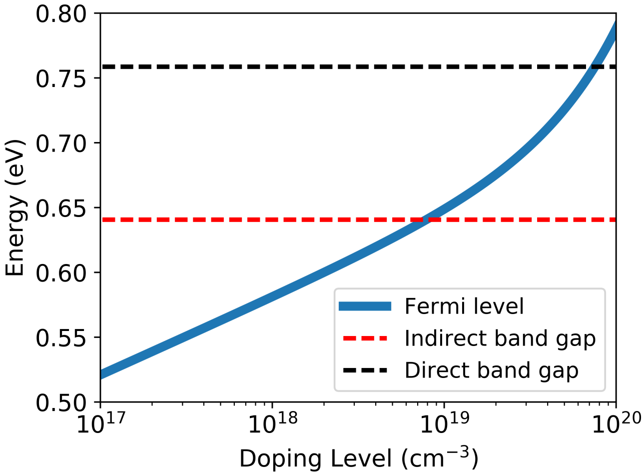

Figure 2.4: Calculations of the Fermi level as a function of doping level in 0.2 % biaxial tensile strained Ge. With a doping level of 7.5×10^{19} cm^{-3}, the Fermi level crosses the Γ conduction valley. The energies are referred with respect to the top of the valence band.

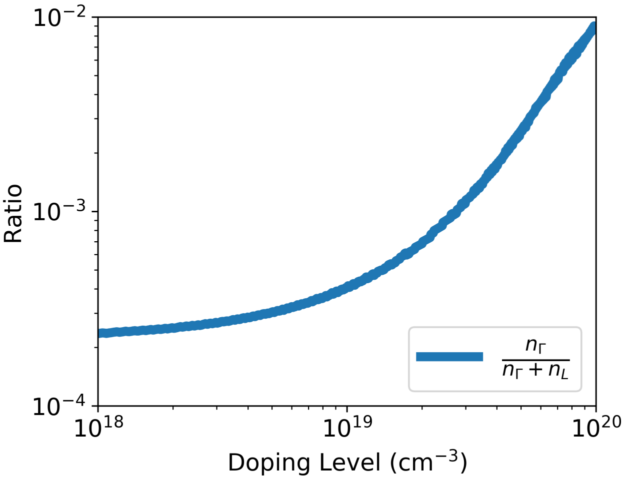

Figure 2.5: Fraction of electrons occupying in the Γ conduction valley as a function of n-type doping concentration in Ge. In this simulation, we inject excess carriers with a concentration of 5×10^{18} cm^{-3}.

concentration for degenerate semiconductors [17].

$$E_{fn} - E_{ci} \approx k_B T \left[ln\left(\frac{n_{ci}}{N_{ci}}\right) + 2^{-\frac{3}{2}} \left(\frac{n_{ci}}{N_{ci}}\right) \right] \tag{2.6}$$

$$E_{vj} - E_{fp} \approx k_B T \Big[ln \Big(\frac{n_{vj}}{N_{vj}} \Big) + 2^{-\frac{3}{2}} \Big(\frac{n_{vj}}{N_{vj}} \Big) \Big] \tag{2.7}$$

In the above equation, i and j represent the conduction (i= Γ or L) and valence bands (j=lh or hh) respectively. N_{ci} and N_{vj} are the effective density of states in the conduction and valence bands and are related to the density of state effective masses ($m_{dos,e}$ and $m_{dos,h}$ for electrons and holes respectively) as shown in Eq. 2.8 and Eq. 2.9. In Eq. 2.8, M_{ci} represents the number of equivalent minima in the conduction band and is equal to 4 for L valley and 1 for Γ valley.

$$N_{ci} = 2 \Big(\frac{2\pi m_{dos,e} k_B T}{h^2} \Big)^{\frac{3}{2}} M_{ci} \tag{2.8}$$

$$N_{vj} = 2 \Big(\frac{2\pi m_{dos,h} k_B T}{h^2} \Big)^{\frac{3}{2}} \tag{2.9}$$

For a fixed electron (or hole) concentration, we can have just one quasi Fermi energy level for each carrier. Therefore, the electron concentration in the Γ or L valleys and the hole concentration in the lh or hh valleys must be self-consistently solved such that the E_{fn} and E_{fp} satisfies Eq. 2.6 and Eq. 2.7 for all the valleys. Fig. 2.4 and Fig. 2.5 shows the fraction of 5×10^{18} cm^{-3} injected electrons that occupy the Γ conduction valley. In this simulation, Ge is 0.2$\%$ biaxially tensile strained, as is typical in Ge-on-Si layers due to mismatch in thermal expansion coefficient between Ge and Si [18]. The figure shows that with an increase in the doping concentration, a substantial fraction of the injected electrons occupies the Γ valley. This approach makes the material a pseudo direct band gap material and can be experimentally verified with PL spectroscopy where the PL signal from the direct valley increases with an increase in the n-type doping level [19–22]. This has propelled research efforts towards the demonstration of an optically pumped and electrically pumped laser using high Phosphorus (P) or Antimony (Sb) doped Ge on Si [23–25]. Even though these devices had a doping level of up to 4×10^{19} cm^{-3}, they operated at very high threshold current densities (J_{th}) of 280-500 kA/cm^2, 3 orders of magnitude higher than typical III-V lasers. Table 2.1 summarizes all Ge based lasers demonstrated over the past decade.

2.1.2 Gain calculations for n-type doped Ge

In this section, we will lay down the requirements to achieve a sub 10 kA/cm^2 laser using highly doped Ge as the active medium. A laser consists of 3 key elements: an active medium to amplify light through stimulated emission, an optical cavity to provide feedback and an electrical or optical pumping scheme to inject carriers into the active medium to reach transparency and further population inversion conditions. Therefore, to have a Ge laser operating at J_{th} <10 kA/cm^2, we will

Active medium	Ref.	Excitation mechanism	Operating T	Threshold pump power	Emission Wavelength
P-doped Ge	[23]	Optically pumped	300 K	30 kW/cm^2	1593 nm
P-doped Ge	[24]	Electrically pumped	300 K	280 kA/cm^2	1576-1656 nm
GeSn	[13]	Optically pumped	20 K	325 kW/cm^2	$\sim$2254 nm
P-doped Ge	[25]	Electrically pumped	300 K	510 kW/cm^2	1682 nm
GIB Ge QDs	[26]	Optically pumped	10 K	3.9 kW/cm^2	1323 nm
GeSn	[14]	Optically pumped	50 K	125 kW/cm^2	$\sim$2066 nm
GeSn	[15]	Optically pumped	10 K	68 kW/cm^2	2400-2500 nm
GeSn	[16]	Optically pumped	110 K	396 kW/cm^2	2400-2500 nm
GeSn	[16]	Optically pumped	180 K	377 kW/cm^2	3110 nm
Strained Ge	[27]	Optically pumped	83 K	3.0 kW/cm^2	1530 nm
GeSn	[28]	Optically pumped	180K	920 kW/cm^2	2945 nm

Table 2.1: Review of Ge based laser reported over the past decade.

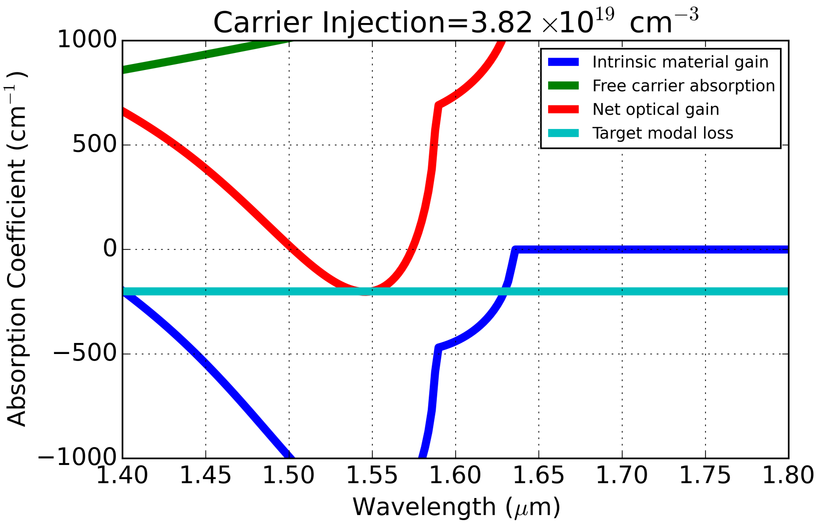

Figure 2.6: Absorption coefficient spectra calculated for Ge doped with n-type dopants with a concentration of 4×10^{19} *cm*$^{-3}$ *and injected with a carrier concentration of 3.82×10*^{19} *cm*$^{-3}$*. The net optical gain is estimated by subtracting free carrier absorption induced by dopants and injected carriers from the intrinsic material gain. This simulation was performed to match a target material gain of 200 cm*$^{-1}$*.*

need to identify the key requirements to obtain net gain in the active medium that can overcome all optical losses in the cavity by assuming 100% carrier injection efficiency.

The interband absorption coefficient of a semiconductor for a transition from the valence to the conduction band is given by Fermi's golden rule [29]:

$$\alpha(\hbar\omega) = \alpha_\circ(\hbar\omega)\Big[f_v(k_\circ) - f_c(k_\circ)\Big] \tag{2.10}$$

$$f_c(k_\circ) = \frac{1}{1+e^{(E_c(k)-E_{fn})/k_BT}} \qquad f_v(k_\circ) = \frac{1}{1+e^{(E_v(k)-E_{fp})/k_BT}} \tag{2.11}$$

$$\alpha_\circ(\hbar\omega) = C_\circ|\widehat{e}.\rho_{cv}|^2\rho_r(\hbar\omega), \quad \rho_r(\hbar\omega) = \frac{1}{2\pi}\left(\frac{2m_r^*}{\hbar^2}\right)^{\frac{3}{2}}(\hbar\omega - E_g)^{\frac{1}{2}} \tag{2.12}$$

$$E_c(k) = E_g + \frac{\hbar^2\mathrm{k}^2}{2m_e^*} \qquad E_v(k) = -\frac{\hbar^2\mathrm{k}^2}{2m_h^*} \tag{2.13}$$

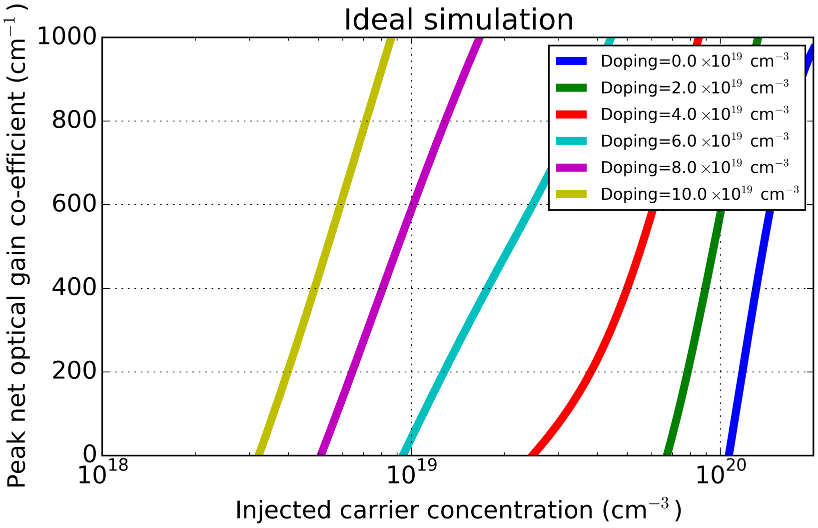

Figure 2.7: Estimated peak optical gain for Ge as function of injected carrier concentration, for varying doping levels. Due to the dependence of the pseudo direct band gap on the doping level, optical transparency and population inversion can be achieved for lower injection levels when Ge is highly doped.

$$\frac{1}{m_r^*} = \frac{1}{m_e^*} + \frac{1}{m_h^*} \tag{2.14}$$

where the Fermi-Dirac distribution for the electron and holes depends on the quasi-Fermi levels obtained using Eq. 2.6 and Eq. 2.7. In these equations m_r^* represents the reduced effective mass and $|\widehat{e}.\rho_{cv}|$ is the momentum matrix element or the transition probability between the conduction and valence band. As the absorption coefficient depends on the momentum matrix element and the joint density of states (JDOS), the modelling framework is called the JDOS model. By fitting the absorption spectrum of Eq. 2.10 with the experimentally derived values, we obtain $C_\circ|\widehat{e}.\rho_{cv}|^2$ = 2×10^4 eV$^{1/2}$/cm [30].

Reaching optical gain requires $\alpha(\hbar\omega)$ <0, which leads, with Eq. 2.10, to the condition of transparency where $f_v(k_\circ) - f_c(k_\circ) < 0$ or $E_{fn} - E_{fp} > E_{g,\Gamma}$. For the device to reach lasing, the gain in the active medium must overcome all cavity losses in the device $\Rightarrow \Gamma G_{th}$=$\alpha_{Cavity}$. where, a material gain (G_{th}) of 200 cm^{-1} from the active region is targetted for. We assume the mirror losses and scattering losses in the cavity to be the main contributors to a cavity loss of 150 cm^{-1} and modal confinement factor of $\Gamma = 0.75$. Fig. 2.6 shows the absorption spectrum for Ge with a doping level of 4×10^{19} cm^{-3} and an injected carrier concentration

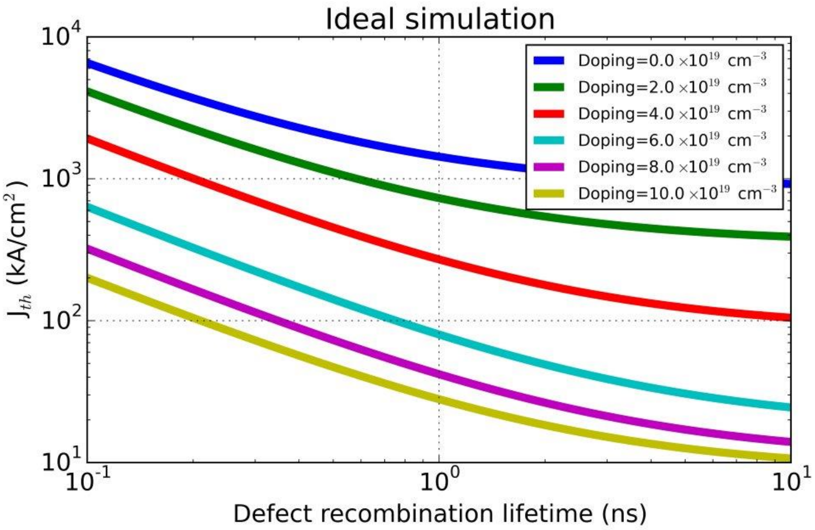

Figure 2.8: Threshold current density estimated for a target modal gain of 200 cm^{-1} using Eq. 2.15 and Fig. 2.7.

of 3.82×10^{19} cm^{-3}. The net optical gain from the material overcomes the free carrier absorption due to dopants and injected excess carriers to match the targeted material gain. The free carrier absorption coefficient was taken from [30]. On comparing the peak net optical gain across a wide range of doping levels and injected carrier densities in Fig. 2.7, it is evident that a target material gain of 200 cm^{-1} can be achieved easily for highly doped Ge material systems, at least in this ideal JDOS model. This is because the pseudo direct band gap behavior of Ge is dependent on the doping level as established in Fig. 2.3. Assuming a typical Ge layer thickness (D) of 0.4 μm embedded in a typical double heterostructure laser, the threshold current density to reach population inversion can be calculated using Eq. 2.15 and Eq. 2.17:

$$J_{th} = \frac{n_{inj} \times D \times e}{\tau_{eff}} \tag{2.15}$$

$$\frac{1}{\tau_{eff}} = \frac{1}{\tau_{defect}} + Bn_{total} + C_n n_{total}^2 + C_p n_{total} \times n_{inj} \tag{2.16}$$

$$n_{total} = n_{inj} + n_{doping} \tag{2.17}$$

where n_{inj} is the required injected carrier concentration to reach population inversion, e is the charge of an electron, τ_{defect} is the carrier lifetime associated with Shockley-Rheed-Hall recombination, and B and C (C_n and C_p) are the radiative and Auger recombination rate coefficients taken from [30]. Using the Eq. 2.15 and Eq. 2.17, we plot J_{th} as a function of carrier lifetime for different doping levels in Fig. 2.8. From this result, the requirements to achieve an n-type doped Ge laser with $J_{th} < 10$ kA/cm^2 can be identified as follows:

- The Shockley Read Hall recombination process mediated carrier lifetime should exceed 10 ns.
- A doping level of 1×10^{20} cm^{-3} is required.

2.1.3 Thesis overview: Ge laser on Si

In Chapter 3, we first study the carrier lifetimes in undoped Ge waveguides with dimensions similar to the targeted DH laser design, integrated in imec's 200mm silicon photonics platform. Carrier lifetimes <1.3 ns, an order of magnitude lower than the initially design goals, are extracted with the help of fiber based pump-probe spectroscopy. Poor Ge/SiO$_2$ and Ge/Si interfaces in these integrated devices are identified to be the root cause for such low carrier lifetimes. In order to improve the lifetimes, we present a comprehensive passivation study with simplified blanket undoped Ge films of thickness 0.6 μm grown on Si, based on time resolved photoluminescence (TRPL) spectroscopy. A maximum carrier lifetime of 4.3 ns in undoped Ge layers is extracted with the best passivation layer. However, dopants will introduce point defects and shorten the carrier lifetime with 4.3 ns being the longest achievable lifetime for Ge-on-Si material systems for a Ge thickness of 0.6 μm.

In Chapter 4, an overview of the epitaxial growth process used to obtain highly n-type doped Ge (Phosphorus dopants are used for this study) is presented. The epitaxy process uses Ge$_2$H$_6$ and PH$_3$ precursors that allow for a low temperature growth and high incorporation of P dopants in Ge. Rapid thermal annealing is performed on these layers to improve the crystallinity and the results are promising. However, with these annealed doped Ge layers, a maximum doping level of 5.35×10^{19} cm^3 could be achieved with a carrier lifetime of <0.4 ns measured using TRPL.

In Chapter 5, we try to understand the impact of many-body effects in any doped Ge material systems by performing photoluminescence spectroscopy and transient absorption spectroscopy. Due to the presence of a high concentration of active phosphorus dopants, carrier scattering induced linewidth broadening affects the recombination and absorption physics in Ge by broadening the corresponding spectrum. To understand these effects better, we modified the standard JDOS model presented in Eq. 2.12 to include many-body effects such as dopant induced band-gap narrowing and dopant dependent linewidth broadening effects. As a result of this, the efficiency with which we can reach transparency and population inversion is dramatically reduced by a factor >4. In addition, carrier lifetimes of <0.3 ns are observed in doped Ge as compared to <3 ns in undoped and unpassivated Ge. Based on the results in this chapter, we will argue that obtaining an energy efficient double heterostructure laser using doped Ge is extremely difficult and at this point cannot be considered as an alternative to existing III-V based laser devices for optical interconnect applications.

2.2 Germanium based electro absorption modulators

Si based modulators use electro-optical phenomena by exploiting the free carrier dispersion effect to modify the effective refractive of light in Si WGs. This phenomena is implemented in the form Mach Zhender interferometer (MZI) and ring resonator configurations to realize electro-optic modulators [31, 32]. MZI modulators typically exhibit large optical bandwidth, but they suffer from a large footprint and high power consumption at high speed. Ring resonator modulators, on the other hand, have small footprint and low power consumption, but suffer from small optical bandwidth and are sensitive to process and thermal variations. Electro absorption modulators (EAM) exploiting the Franz-Keldysh effect or the quantum confined stark effect (QCSE) on the other hand, operate by tuning the absorption coefficient of the material within a specific spectral regime under the influence of an applied electric field [29]. The change in absorption coefficient from *ON* to *OFF* state ranges from 100-5000 cm^{-1}, resulting in devices that are significantly shorter than typical MZI modulators and have a power consumption comparable to that of ring modulators. The intrinsic switching time response of the EA-effect is sub-picosecond. Therefore, these modulators are usually limited by the RC time constant of the device [33]. Their optical bandwidth lies in between that of ring resonator based modulators and MZI based modulators. Moreover, EAMs are promising devices that operate at the trade off between speed and power consumption [34].

2.2.1 Ge based FKE EAM vs QCSE EAM

The Franz-Keldysh effect refers to a change in the absorption of a bulk semiconductor when applying an electrical field. The applied field results in tilting of the energy band profile as illustrated in Fig 2.9 [29]. The band tilting allows for the electron wavefunction from the conduction band and the hole wavefunction from the valence band to penetrate in to the band gap. This introduces an absorption tail for photon energies $h\nu < E_g$, which can be modulated by the electric field.

The presence of a direct band gap at photon energies of 0.8 eV for undoped and unstrained Ge allows for modulation of light at wavelengths >1550 nm. Due to the presence of 0.2$\%$ biaxial tensile in Ge-on-Si material systems, this direct

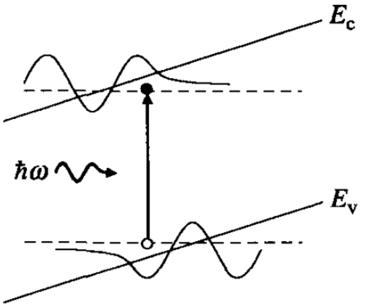

Figure 2.9: Franz Keldysh effect: tilting of the bands in bulk semiconductors under an applied field allows for penetration of the wavefunctions in the band gap. This results in absorption of light with photon energy below the band gap [29].

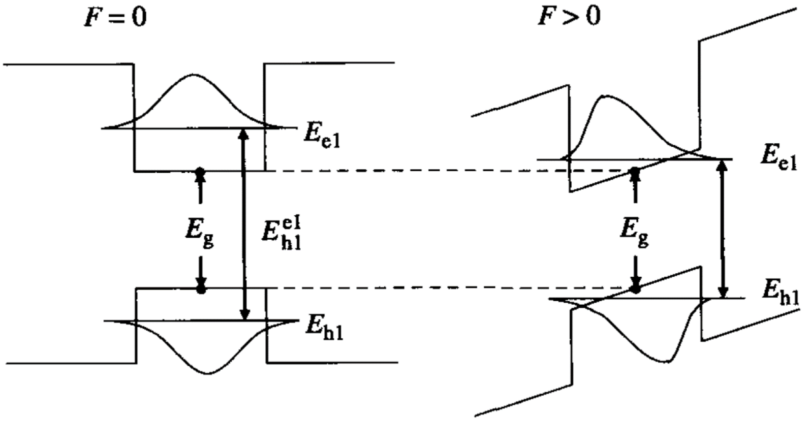

Figure 2.10: Quantum Confined Stark Effect: Quantum well wavefunctions and energy subbands in the absence and presence of an electric field. With an applied electric field, the transition wavelength between the subbands redshifts allowing for absorption of light at photon energies below the band gap [29].

band gap shifts to $\approx$0.78 eV resulting in modulation at wavelengths $>$ 1600nm. The operating wavelength can be shifted back to 1550 nm with the addition of Si ($<1\%$) to form $\mathrm{Ge}_{1-x}\mathrm{Si}_x$. However, in these Ge based FKE devices, the modulation contrast or the figure of merit (FOM) determined by the equation $\Delta\alpha/\alpha = (\alpha(E_{on}) - \alpha(E_{off}))/\alpha(E_{off}))$ is relatively low due to the presence of the indirect band gap absorption. This requests for high E_{on}-E_{off} contrasting resulting in high operating voltages for a desired FOM.

On the other hand, the quantum confined stark effect (QCSE) that occurs in

		FKE EAM	**QCSE EAM**
Processing complexity		**Easy** due to bulk semiconductor	Difficult due to strain balance constraint in type-I MQW stack
Absorption	Modal confinement	**High**	Low
	Insertion Loss	Moderate indirect absorption	Moderate indirect absorption
	$\Delta\alpha/\alpha$	Moderate	**High** due to excitonic resonances
	Operating V swing	High	Low
Wavelength	Operating Wavelength	1520-1630 nm Depending on Si content in $\text{Ge}_{1-x}\text{Si}_x$	**1270-1570 nm** Depending on stack
	Optical Bandwidth	$\approx$ 35nm: 1dB transmitter penalty	<20nm, but can cover ~**100nm** if bias voltage is tuned
Speed		**RC limited**	**RC limited**
Power Consumption	Static	**Moderate** due to photocurrent	**Moderate** due to photocurrent
	Dynamic	**Low** due to small footprint	**Low** due to small footprint

Table 2.2: Ge based FKE EAM vs QCSE EAM.

Type-I quantum wells allows for a high FOM at low operating voltages. This is related to the presence of a strong exciton absorption peak. The exciton binding energy is typically large in quantum well systems as compared to bulk materials due to quantum confinement. The exciton absorption peaks along with the discrete subband absorption spectrum from the quantum wells redshift with increasing reverse bias as illustrated in Fig. 2.10. However, the absorption coefficient also decreases with increase in electric field, due to the reduction in overlap integral between the electron and hole wavefunction. Inspite of this, GeSi based QCSE EAMs have been demonstrated to have a higher FOM than GeSi based FKE EAMs [35]. The only drawback of QCSE EAM based devices is their increased processing complexity as compared to FKE EAM. Maintaining Type-I band alignment and the appropriate strain balance in the quantum well stack is a challenging task that requires a complex epitaxy process. Table 2.2 compares the performance of FKE- and QCSE-based EAMs [35].

The performance of FKE based Ge EAMs reported over the last decade is summarized in Table 2.3. The first waveguide integrated Ge based FKE EAM demonstrated on Si was presented in [36] with a vertical p-i-n diode. This device operated at 1550nm with an extinction ratio (ER) of 8 dB for a 3 V swing from -4 V to -7 V. Due to the compact design of the device, the capacitance was as low as 11 fF, resulting in 50 fJ/bit energy consumption at a data-rate of 1Gb/s. This promising result stimulated a series of other demonstration, as can be seen in Table 2.3, with the most recent GeSi (0.7 %) FKE EAM operating at a speed of 40 Gb/s. The FOM of all these devices is low, due to wide WG dimensions resulting in low E-field contrast between the ON and OFF state. This offers room for improvement of the static performance of such a device. Our target at the start of this work was to improve the static performance of Ge FKE EAMs and in particular their FOM, while enabling a small signal bandwidth of >50 GHz. To make this possible, the following subobjectives are set forward for the GeSi FKE EAM to be developed:

- Use a butt coupling scheme to reduce insertion loss.
- Focus on compact waveguide dimensions that will enable high ER/IL performance.
- Optimize the doping profile and doping levels to reduce the RC time constant of the diode.

2.2.2 Thesis overview: Ge based electro absorption modulator

With the target design goals defined in the previos section, in Chapter 6, we will present Ge based and GeSi based FKE EAM devices integrated in imec's 200mm Silicon photonics platform exhibiting a FOM=1.33 for a 3 V swing and a 1 dB small-signal bandwidth of >50 GHz. We will then conclude the chapter with the

		[36]	[37]	[38]	[39]
Material		GeSi	Ge	Ge	GeSi
Design (pin diode)		Vertical	Lateral	Lateral	Lateral
Operating wavelength (nm)		**1539 to 1553**	1580 to 1610	1610 to 1640	**1545 to 1581**
Coupling Scheme		**Butt**	Evanescent	**Butt**	**Butt**
Dimensions	Thickness	400 nm	400 nm	600 nm	550 nm
	Width	600 nm	600 nm	1 μm	1 μm
	Length	50 μm	40 μm	45 μm	55 μm
Static Performance	V swing	-4 to -7	0 to -3	0 to -3	**0 to -3**
	FOM=ER/IL	**2**	0.6	1.2	1.2
Bandwidth (f_{3dB})		1.2	1.25	28.2	**40.7**
Power Consumption	Static	-	-	-	6.7 mW
	Dynamic	**49.5 fJ/bit**	**<100 fJ/bit**	**100 fJ/bit**	**60 fJ/bit**

Table 2.3: Review of Ge based FKE EAM reported over the past decade.

preliminary demonstration of a Ge based quantum confined stark effect electro absorption modulator with a FOM=1.75 for a 1 V swing.

References

[1] Krishna Saraswat, Chi On Chui, Tejas Krishnamohan, Donghyun Kim, Ammar Nayfeh, and Abhijit Pethe. *High performance germanium MOSFETs*. Materials Science and Engineering: B, 135(3):242 – 249, 2006. E-MRS IUMRS ICEM 2006, Symposium B; From strained silicon to nanotubes - Novel channels for field effect devices.

[2] R. Loo, A. Y. Hikavyy, L. Witters, A. Schulze, H. Arimura, D. Cott, J. Mitard, C. Porret, H. Mertens, P. Ryan, J. Wall, K. Matney, M. Wormington, P. Favia, O. Richard, H. Bender, A. Thean, N. Horiguchi, D. Mocuta, and N. Collaert. *Processing Technologies for Advanced Ge Devices*. ECS Journal of Solid State Science and Technology, 6(1):P14–P20, 2017.

[3] Gang Wang, Frederik E Leys, Laurent Souriau, Roger Loo, Matty Caymax, David P Brunco, Jef Geypen, Hugo Bender, Marc Meuris, Wilfried Vandervorst, et al. *Selective epitaxial growth of germanium on Si wafers with shallow trench isolation: an approach for Ge virtual substrates*. ECS Transactions, 16(10):829–836, 2008.

[4] Yasuhiko Ishikawa, Kazumi Wada, Douglas D. Cannon, Jifeng Liu, Hsin-Chiao Luan, and Lionel C. Kimerling. *Strain-induced band gap shrinkage in Ge grown on Si substrate*. Applied Physics Letters, 82(13):2044–2046, 2003.

[5] Richard Geiger, Thomas Zabel, and Hans Sigg. *Group IV direct band gap photonics : Methods , Challenges and Opportunities*. Frontiers in Materials, 2(July), 2015.

[6] Yosuke Shimura, Srinivasan Ashwyn Srinivasan, and Roger Loo. *Design Requirements for Group-IV Laser Based on Fully Strained Ge1xSnx Embedded in Partially Relaxed Si1yzGeySnz Buffer Layers*. ECS Journal of Solid State Science and Technology, 5(5):Q140–Q143, 2016.

[7] Chris G. Van de Walle. *Band lineups and deformation potentials in the model-solid theory*. Phys. Rev. B, 39:1871–1883, Jan 1989.

[8] Jifeng Liu, Douglas D. Cannon, Kazumi Wada, Yasuhiko Ishikawa, David T. Danielson, Samerkhae Jongthammanurak, Jurgen Michel, and Lionel C. Kimerling. *Deformation potential constants of biaxially tensile stressed* Ge *epitaxial films on* $\mathrm{Si}(100)$. Phys. Rev. B, 70:155309, Oct 2004.

[9] Douglas J Paul. *Si/SiGe heterostructures: from material and physics to devices and circuits*. Semiconductor Science and Technology, 19(10):R75, 2004.

[10] Moustafa El Kurdi, Guy Fishman, Sbastien Sauvage, and Philippe Boucaud. *Band structure and optical gain of tensile-strained germanium based on a 30 band kp formalism*. Journal of Applied Physics, 107(1):013710, 2010.

[11] B. Dutt, H. Lin, D. S. Sukhdeo, B. M. Vulovic, S. Gupta, D. Nam, K. C. Saraswat, and J. S. Harris Jr. *Theoretical Analysis of GeSn Alloys as a Gain Medium for a Si-Compatible Laser*. IEEE Journal of Selected Topics in Quantum Electronics, 19(5):1502706–1502706, Sept 2013.

[12] Moustafa El Kurdi, Mathias Prost, Abdelhamid Ghrib, Sbastien Sauvage, Xavier Checoury, Grgoire Beaudoin, Isabelle Sagnes, Gennaro Picardi, Razvigor Ossikovski, and Philippe Boucaud. *Direct Band Gap Germanium Microdisks Obtained with Silicon Nitride Stressor Layers*. ACS Photonics, 3(3):443–448, 2016.

[13] S Wirths, R Geiger, N Von Den Driesch, G Mussler, T Stoica, S Mantl, Z Ikonic, M Luysberg, S Chiussi, J M Hartmann, H Sigg, J Faist, D Buca, and D Grützmacher. *Lasing in direct-bandgap GeSn alloy grown on Si*. Nature Photonics, 9(2):88–92, 2015.

[14] Daniela Stange, Stephan Wirths, Richard Geiger, Christian Schulte-Braucks, Bahareh Marzban, Nils von den Driesch, Gregor Mussler, Thomas Zabel, Toma Stoica, Jean-Michel Hartmann, Siegfried Mantl, Zoran Ikonic, Detlev Grtzmacher, Hans Sigg, Jeremy Witzens, and Dan Buca. *Optically Pumped GeSn Microdisk Lasers on Si*. ACS Photonics, 3(7):1279–1285, 2016.

[15] Sattar Al-Kabi, Seyed Amir Ghetmiri, Joe Margetis, Thach Pham, Yiyin Zhou, Wei Dou, Bria Collier, Randy Quinde, Wei Du, Aboozar Mosleh, Jifeng Liu, Greg Sun, Richard A. Soref, John Tolle, Baohua Li, Mansour Mortazavi, Hameed A. Naseem, and Shui-Qing Yu. *An optically pumped 2.5m GeSn laser on Si operating at 110K*. Applied Physics Letters, 109(17):171105, 2016.

[16] V. Reboud, A. Gassenq, N. Pauc, J. Aubin, L. Milord, Q. M. Thai, M. Bertrand, K. Guilloy, D. Rouchon, J. Rothman, T. Zabel, F. Armand Pilon, H. Sigg, A. Chelnokov, J. M. Hartmann, and V. Calvo. *Optically pumped GeSn micro-disks with 16% Sn lasing at 3.1 m up to 180K*. Applied Physics Letters, 111(9):092101, 2017.

[17] S.M. Sze and K.K. Ng. *Physics of Semiconductor Devices*. Wiley, 2006.

[18] Yasuhiko Ishikawa, Kazumi Wada, Jifeng Liu, Douglas D. Cannon, Hsin-Chiao Luan, Jurgen Michel, and Lionel C. Kimerling. *Strain-induced enhancement of near-infrared absorption in Ge epitaxial layers grown on Si substrate*. Journal of Applied Physics, 98(1):013501, 2005.

[19] Xiaochen Sun, Jifeng Liu, Lionel C. Kimerling, and Jurgen Michel. *Direct gap photoluminescence of n-type tensile-strained Ge-on-Si*. Applied Physics Letters, 95(1):011911, 2009.

[20] M. El Kurdi, T. Kociniewski, T.-P. Ngo, J. Boulmer, D. Dbarre, P. Boucaud, J. F. Damlencourt, O. Kermarrec, and D. Bensahel. *Enhanced photoluminescence of heavily n-doped germanium*. Applied Physics Letters, 94(19):191107, 2009.

[21] Yosuke Shimura, Srinivasan Ashwyn Srinivasan, Dries Van Thourhout, Rik Van Deun, Marianna Pantouvaki, Joris Van Campenhout, and Roger Loo. *Enhanced active P doping by using high order Ge precursors leading to intense photoluminescence*. Thin Solid Films, 602(Supplement C):56 – 59, 2016. The 9th International Conference on Silicon Epitaxy and Heterostructures.

[22] Yuji Yamamoto, Michael Reiner Barget, Giovanni Capellini, Noriyuki Taoka, Michele Virgilio, Peter Zaumseil, Anne Hesse, Thomas Schroeder, and Bernd Tillack. *Photoluminescence of phosphorous doped Ge on Si (100)*. Materials Science in Semiconductor Processing, 70(Supplement C):111 – 116, 2017. Control of Semiconductor Interfaces and SiGe Technology/Devices.

[23] Jifeng Liu, Xiaochen Sun, Rodolfo Camacho-Aguilera, Lionel C. Kimerling, and Jurgen Michel. *Ge-on-Si laser operating at room temperature*. Opt. Lett., 35(5):679–681, Mar 2010.

[24] Rodolfo E. Camacho-Aguilera, Yan Cai, Neil Patel, Jonathan T. Bessette, Marco Romagnoli, Lionel C. Kimerling, and Jurgen Michel. *An electrically pumped germanium laser*. Opt. Express, 20(10):11316–11320, May 2012.

[25] Roman Koerner, Michael Oehme, Martin Gollhofer, Marc Schmid, Konrad Kostecki, Stefan Bechler, Daniel Widmann, Erich Kasper, and Joerg Schulze. *Electrically pumped lasing from Ge Fabry-Perot resonators on Si*. Opt. Express, 23(11):14815–14822, Jun 2015.

[26] Martyna Grydlik, Florian Hackl, Heiko Groiss, Martin Glaser, Alma Halilovic, Thomas Fromherz, Wolfgang Jantsch, Friedrich Schaffler, and Moritz Brehm. *Lasing from glassy Ge quantum dots in crystalline Si*. ACS photonics, 3(2):298–303, 2016.

[27] Shuyu Bao, Daeik Kim, Chibuzo Onwukaeme, Shashank Gupta, Krishna Saraswat, Kwang Hong Lee, Yeji Kim, Dabin Min, Yongduck Jung, Haodong Qiu, et al. *Low-threshold optically pumped lasing in highly strained germanium nanowires*. Nature communications, 8(1):1845, 2017.

[28] Joe Margetis, Sattar Al-Kabi, Wei Du, Wei Dou, Yiyin Zhou, Thach Pham, Perry Grant, Seyed Ghetmiri, Aboozar Mosleh, Baohua Li, et al. *Si-based GeSn lasers with wavelength coverage of 2 to 3 μm and operating temperatures up to 180 K*. ACS Photonics, 2017.

[29] S.L. Chuang. *Physics of Photonic Devices*. Wiley Series in Pure and Applied Optics. John Wiley & Sons, 2009.

[30] Jifeng Liu, Xiaochen Sun, Dong Pan, Xiaoxin Wang, Lionel C. Kimerling, Thomas L. Koch, and Jurgen Michel. *Tensile-strained, n-type Ge as a gain medium for monolithic laser integration on Si*. Opt. Express, 15(18):11272–11277, Sep 2007.

[31] Erman Timurdogan, Cheryl M Sorace-Agaskar, Jie Sun, Ehsan Shah Hosseini, Aleksandr Biberman, and Michael R Watts. *An ultralow power athermal silicon modulator*. Nature communications, 5, 2014.

[32] Xi Xiao, Hao Xu, Xianyao Li, Zhiyong Li, Tao Chu, Yude Yu, and Jinzhong Yu. *High-speed, low-loss silicon Mach–Zehnder modulators with doping optimization*. Opt. Express, 21(4):4116–4125, Feb 2013.

[33] J. F. Lampin, L. Desplanque, and F. Mollot. *Detection of picosecond electrical pulses using the intrinsic FranzKeldysh effect*. Applied Physics Letters, 78(26):4103–4105, 2001.

[34] David A. B. Miller. *Energy consumption in optical modulators for interconnects*. Opt. Express, 20(S2):A293–A308, Mar 2012.

[35] Papichaya Chaisakul, Delphine Marris-Morini, Mohamed-Said Rouifed, Jacopo Frigerio, Daniel Chrastina, Jean-Ren Coudevylle, Xavier Le Roux, Samson Edmond, Giovanni Isella, and Laurent Vivien. *Recent progress in GeSi electro-absorption modulators*. Science and Technology of Advanced Materials, 15(1):014601, 2014.

[36] Jifeng Liu, Mark Beals, Andrew Pomerene, Sarah Bernardis, Rong Sun, Jing Cheng, Lionel C Kimerling, and Jurgen Michel. *Waveguide-integrated, ultralow-energy GeSi electro-absorption modulators*. Nature Photonics, 2(7):433–437, 2008.

[37] Andy Eu-Jin Lim, Tsung-Yang Liow, Fang Qing, Ning Duan, Liang Ding, Mingbin Yu, Guo-Qiang Lo, and Dim-Lee Kwong. *Novel evanescent-coupled germanium electro-absorption modulator featuring monolithic integration with germanium p-i-n photodetector*. Opt. Express, 19(6):5040–5046, Mar 2011.

[38] Ning-Ning Feng, Dazeng Feng, Shirong Liao, Xin Wang, Po Dong, Hong Liang, Cheng-Chih Kung, Wei Qian, Joan Fong, Roshanak Shafiiha, Ying Luo, Jack Cunningham, Ashok V. Krishnamoorthy, and Mehdi Asghari. *30GHz Ge electro-absorption modulator integrated with 3μm silicon-on-insulator waveguide*. Opt. Express, 19(8):7062–7067, Apr 2011.

[39] Dazeng Feng, Shirong Liao, Hong Liang, Joan Fong, Bhavin Bijlani, Roshanak Shafiiha, B. Jonathan Luff, Ying Luo, Jack Cunningham, Ashok V. Krishnamoorthy, and Mehdi Asghari. *High speed GeSi electro-absorption modulator at 1550 nm wavelength on SOI waveguide*. Opt. Express, 20(20):22224–22232, Sep 2012.

3

Carrier lifetimes in Ge-on-Si material systems

In this chapter, we will investigate the quality of nominally undoped Ge films by estimating the carrier lifetime in these films. As we explained in previous chapters, obtaining a sufficiently long carrier lifetime is essential for energy efficient operation of a laser. We first investigate Ge-on-Si WGs with dimensions comparable to our target laser device via fiber based pump probe spectroscopy. Thereafter, we explore various passivation schemes aimed to increase the lifetime in Ge-on-Si films.

3.1 Pump-probe spectroscopy of Ge-on-Si WGs

3.1.1 Sample description and experimental framework

A set of Ge-on-Si WGs with different width (0.4 μm to 1.0 μm) and thickness (0.2 μm and 0.375 μm) are investigated in this section. These WGs are of lengths 8 μm, 17.6 μm and 40 μm, but lifetime analysis was performed predominantly on the 8 μm long WGs. The varying cross-sectional dimensions of the WGs will allow us to investigate how the measured carrier lifetimes depend on the surfaces. The WGs were fabricated using imec's 200 mm Si photonics platform on a SOI wafer with a 220 nm top Si layer and 2 μm burried oxide. Ge was grown on top of the Si layer with a 30 nm and 110 nm recess etch to target a final thickness of 0.2 μm and 0.375 μm respectively as can be seen in Fig. 3.1 [1]. Ge was

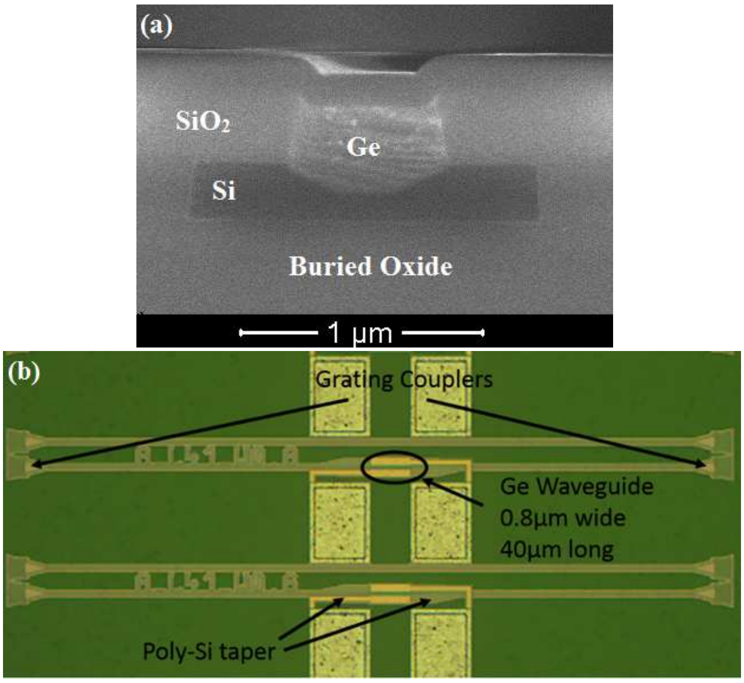

Figure 3.1: a) Cross-sectional scanning electron micrograph of a 0.375 µm thick Ge WG. Ge was epitaxially grown on 110 nm deep recessed Si. b) Top microscope image of Ge-on-Si WGs with poly-Si tapers and grating couplers in the final device under test (DUT).

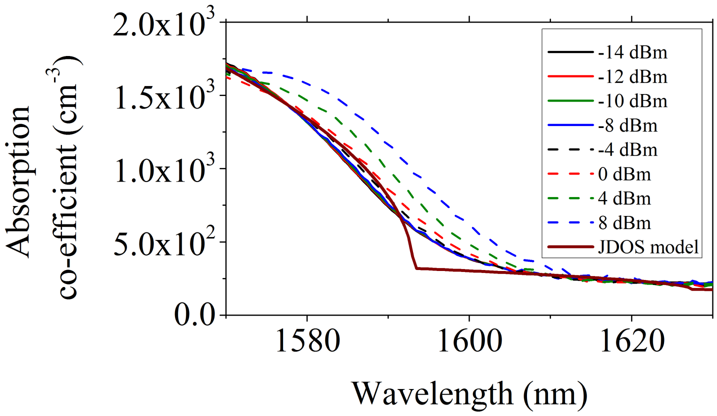

Figure 3.2: Absorption coefficient of Ge-on-Si WG measured using transmission measurement, at different input laser powers (as measured before the input grating coupler).

grown with a selective process using reduced pressure chemical vapour deposition (RPCVD). It was performed in a single step without any intermediate buffer layer, followed by an annealing step to suppress the threading dislocation density and finally chemical mechanical polished (CMP) in order to planarize the WGs to their target thicknesses [1]. The top surface of the Ge was then passivated with PECVD SiO_2 to give a Ge-on-Si WG with cross-section as shown in the scanning electron microscope image in Fig. 3.1. These WGs were butt coupled to an adiabatic tapert using Poly-Si tapers. The SOI WG was terminated with TE polarized grating couplers for coupling light to and from the chip as can be seen in Fig. 3.1.

The carrier lifetimes in the Ge layer of the WGs were measured using fiber based pump-probe spectroscopy [2]. The setup uses a mode locked femtosecond fiber laser (from Calmer laser) as the pump and a CW tunable laser source as the probe. The pump laser has a center wavelength of 1548.57 nm and a pulse width of $<$1 ps. Since the probe signal should ideally be chosen at a wavelength below the band gap of Ge so that excited carriers are dominantly pump induced, it is essential to know the band structure of Ge in the WG. For this, we extracted the absorption coefficient by performing a transmission measurement using a tunable CW laser source and fit it with the standard Density of States model (JDOS) described by Eq. 2.10 to Eq. 2.14 . In this measurement, the insertion loss introduced by the poly-Si tapers was removed using the cut-back method. The loss from the grating couplers was removed by measuring a stand-alone reference SOI WG connected to identical grating couplers. Fig. 3.2 shows the extracted absorption spectrum and fit to the JDOS model. The laser input power has a significant impact on the measurement due to the presence of probe induced excited carriers that causes free-

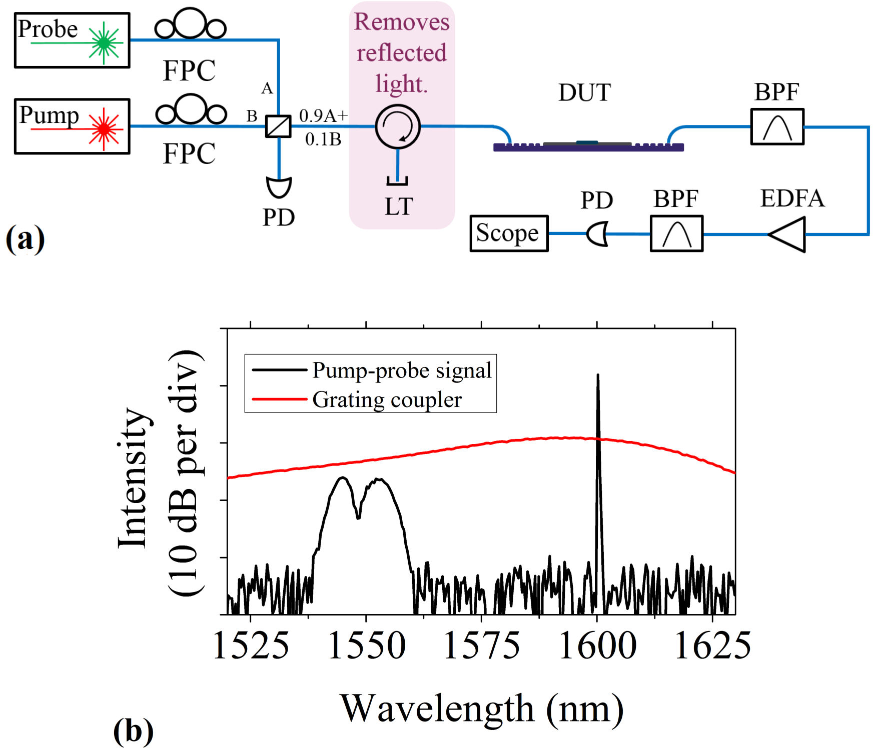

Figure 3.3: a) Schematic of the fiber based pump-probe spectroscopy setup used to estimate the carrier lifetimes in Ge-on-Si WGs. b) The spectrum containing the pump signal centered at 1600 nm and pump signal centered at 1548.67 nm along with the transmission spectra of the grating couplers.

carrier absorption (FCA) and optical bleaching effect (OBE). These effects were earlier observed and reported in [3]. Moreover, given the thick buried oxide layer below the waveguides, thermal effects induced by the CW pump at high optical power modify the shape of the spectrum. As a result, the measured absorption coefficient increases with increase in probe power, contrary to those reported in [3]. Therefore, in order to extract the band gap, we used the spectrum measured at low input power levels. The fitting process also considers absorption from the indirect conduction valley using Macfarlane equations [4]. A biaxial tensile strain of 0.2$\%$ resulting in $E_{g,\Gamma-lh}$= 0.762 eV (1627 nm) and $E_{g,\Gamma-hh}$=0.778 eV (1592 nm) was estimated in Ge. As the absorption is dominated by the $\Gamma - hh$ recombination process, the probe wavelength can be set to any wavelength $>$ 1592 nm. Therefore, a probe wavelength of 1600 nm was chosen since the transmission spectra of the grating coupler also peaked close to 1600 nm.

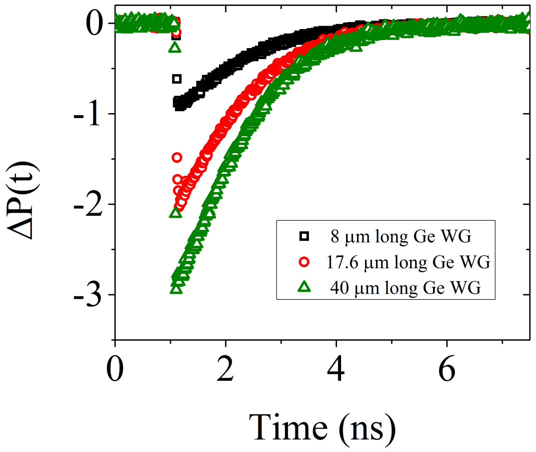

Figure 3.4: Time resolved transmission data of the probe signal through a 1 µm wide, 0.375 µm thick Ge-on-Si WG. ΔP(t) is the excess loss the probe signal experiences due to pump induced photo-excited carriers.

The schematic of the setup used is shown in Fig. 3.3. The pump signal operates at a repetition rate of 20 MHz with an average output power of 7.9 mW, which translates to 400 pJ per pulse. The optical power of the probe signal was set to $<$ 0 dBm (before the grating coupler) at 1600 nm in order to avoid heating effects under CW operation as seen in Fig. 3.2. For maximum coupling with the SOI WG through the grating couplers, the pump and probe polarization were independently controlled before being combined using a 90%:10% coupler leading to 0.5 dB attenuation of the probe signal and 10 dB attenuation of the pump signal. The high attenuation of the pump signal reduces any self-phase modulation along the optical fiber and also reduces interference from photo-excited carriers generated due to two-photon absorption in the SOI WG. The pump pulses are absorbed in the Ge-on-Si WG, generating a high density of photo-excited electrons hole pairs. Any residual pump signal transmitted through the WG and the output grating coupler will be filtered out by the band-pass filters (BPF) centered at the probe wavelength ($>$ 50 nm away from the pump signal wavelength). The probe signal that captures the dynamics of the photo-excited carriers in the WG is detected using an ultrafast photodiode (UPD-15-IR2-FC) from ALPHALAS and Tektronix CSA8000 Signal Analyzer triggered by the pump laser (Oscilloscope). Since the bandwidth of the photodiode and the oscilloscope are $>$ 25 GHz, the resolution of the experiment is better than 15 ps.

3.1.2 Results and discussion

Pump induced photo-excited carriers, that decay in time due to recombination, temporally modify the transmission of the probe signal at 1600 nm, due to FCA and OBE. Therefore, the temporal behaviour of the probe signal, monitored using the ultrafast photodiode and the oscilloscope, carries the signature of the carrier dynamics in Ge WGs. Fig. 3.4 shows the typical result extracted from a 1 μm wide and 0.375 μm thick Ge-on-Si WG with 8 μm, 17.6 μm and 40 μm lengths, where $\Delta P(t)$ is defined in Eq. 3.1.

$$\begin{aligned}\Delta P(t)|_{dB} = \big(&\alpha_{FCA}(t_\circ) + \alpha_{Ge}(t_\circ) - \alpha_{FCA}(t) - \alpha_{Ge}(t)\big) \\ &\times L_{WG} \times 10log_{10}e\end{aligned} \tag{3.1}$$

Here, $\Delta P(t)|_{dB} = 10log_{10}\big(P_{out}(t)/P_{out}(t_\circ)\big)$ with $P_{out}(t_\circ)$ and $P_{out}(t)$ being the output power level of the probe signal at the time instant t = 0 ns and $t > 0$ ns, respectively. The time dependent free carrier absorption (α_{FCA}) at the 1600 nm probe wavelength and the intrinsic material absorption (α_{Ge}) are expressed in Eq. 3.2 and Eq. 3.3 [5].

$$\alpha_{FCA}(t) = 3.1 \times 10^{-18} N(t) + 3.8 \times 10^{-17} P(t) \tag{3.2}$$

$$\begin{aligned}\alpha_{Ge}(t) &= \alpha_\circ \times \Big(f_v\big(N(t)\big) - f_c\big(N(t)\big)\Big) \\ &= \alpha_\circ \times \Big(1 - OBE\big(N(t)\big)\Big)\end{aligned} \tag{3.3}$$

with the optical bleaching effect defined as $OBE = 1 - \Big(f_v\big(N(t)\big) - f_c\big(N(t)\big)\Big)$ such that at t = 0 ns, when we have minimal or no pump induced photo-excited carriers, $OBE = 0$ with $f_c = 0$ and $f_v = 1$ [6]. As a result, Eq. 3.1 translates to Eq. 3.4 where we use $\alpha_{excarr} = \alpha_{FCA} - \alpha_\circ \times OBE$.

$$\Delta P(t)|_{dB} = \Big(\alpha_{excarr}\big(N(t)\big) - \alpha_{excarr}\big(N(t_\circ)\big)\Big) \times L_{WG} \times 10log_{10}e \tag{3.4}$$

The results obtained from the JDOS model described by Eq. 2.10 to Eq. 2.14 and Eq. 3.2 to Eq. 3.3 are shown in Fig. 3.5. We can see that α_{excarr} has a linear dependence on the carrier concentration. As a result, $\Delta P(t)|_{dB} \propto \Delta N(t)$ and the time constant of the decay in Fig. 3.4 is the lifetime of the excess carrier in the WG. It is important to note that in all of the above calculations, we assume a uniform carrier concentration distribution across the length of the WG. This assumption is valid for at least the 8 μm long Ge-on-Si WG as $\Delta P(t)|_{dB}$ for the 17.6 μm long WG is approximately 2.25 times larger than the 8 μm long WG. Instead of the standard exponential decay, the pump signal undergoes OBE and FCA due to its high pulse energy and the location of the pump wavelength close to the $\Gamma - hh$

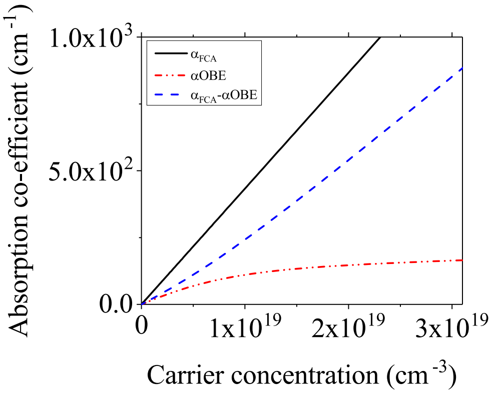

Figure 3.5: Impact of photo-excited carriers on free carrier absorption and optical bleaching effect for a probe signal at 1600 nm, calculated using a standard JDOS model.

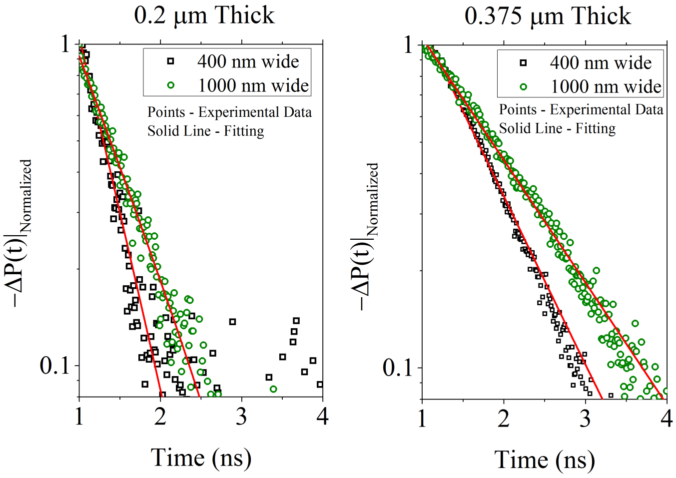

Figure 3.6: Normalized $\Delta P(t)|_{dB}$ as a function of time for Ge-on-Si WGs with a width of 0.4 μm and 1.0 μm and Ge thickness of 0.2 μm and 0.375 μm.

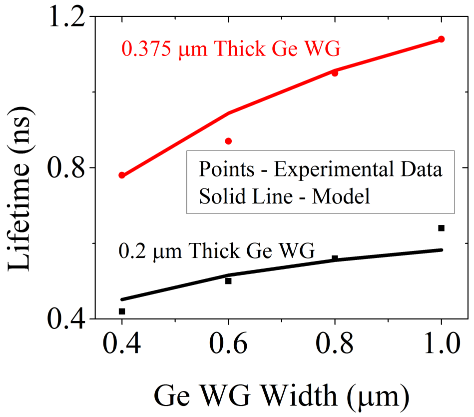

Figure 3.7: Dependence of carrier lifetime on width of the WG. Recombination model using Eq. 3.5 and Eq. 3.6 were used to estimate a surface recombination velocity of 0.975×10^4 *cm/s and* 1.45×10^4 *cm/s for the Ge/Si and Ge/SiO*$_2$ *interfaces respectively.*

WG width (μm)	Measured Lifetime (ns)		Simulated Lifetime (ns)	
	0.2 μm	0.375 μm	0.2 μm	0.375 μm
0.4	0.42	0.78	0.45	0.78
0.6	0.5	0.87	0.52	0.94
0.8	0.56	1.05	0.55	1.05
1.0	0.64	1.14	0.58	1.14

Table 3.1: Measured and simulated carrier lifetime for Ge-on-Si WGs with Ge thickness of 0.2 μm and 0.375 μm integrated in imec's 200 mm silicon photonics platform.

band gap. Therefore, the experimental analysis is performed on the 8 μm long Ge WGs.

Fig. 3.6 shows the extracted $\Delta P(t)|_{dB}$ data after normalization to estimate the time constant of the exponential decay. The results are summarized in Table 3.1. The longest measured lifetime in these WGs was 1.14 ns with lifetimes showing a strong dependence on the width of the WG and the Ge thickness. For a $\Delta P(t)_{max}$ = 1 dB in a 8 μm long Ge WG, we estimate the pump-induced carrier concentration to be 2×10^{19} cm^{-3} using Fig. 3.5. Assuming a radiative recombination coefficient B = 1×10^{-10} cm^{3}s^{-1} and an Auger recombination coefficient C = 1×10^{-31} cm^{6}s^{-1}, the calculated radiative and Auger recombination limited lifetimes in the material are $>$ 10 ns [5, 7]. This suggests that the measured lifetimes of $<$ 1.2 ns are defect mediated, with surface recombination effects being dominant due to the high surface area/volume ratio. They are related using the Eq. 3.5 and Eq. 3.6 with τ_b and τ_s representing bulk and surface lifetimes respectively.

$$\frac{1}{\tau} = \frac{1}{\tau_b} + \frac{1}{\tau_s} \tag{3.5}$$

$$\begin{aligned} \frac{1}{\tau_\mathrm{s}} &= \frac{\mathrm{V_{s,Ge/TopSiO_2}A_{Ge/TopSiO_2}}}{\mathrm{Vol_{WG}}} \\ &+2\times\frac{\mathrm{V_{s,Ge/SideSiO_2}A_{Ge/SideSiO_2}}}{\mathrm{Vol_{WG}}} \\ &+\frac{\mathrm{V_{s,Ge/Si}A_{Ge/Si}}}{\mathrm{Vol_{WG}}} \end{aligned} \tag{3.6}$$

In the above equations, the surface recombination velocity of the Ge interfaces is represented by V_s. The area of the interface and the volume of the WG are denoted as A and Vol$_{WG}$ respectively. Since the Ge was selectively grown on Si in an oxide window opening, the interface with the SiO$_2$ at the side of the waveguide must be different to that with the top SiO$_2$. The latter was deposited using a PEALD process. However, for simplicity, we will assume that the 2 interfaces have the same surface recombination velocity and fit the measured lifetime with Eq. 3.6. The results of the fitting is shown in Fig. 3.7 where a SRV of 0.975×10^{4} cm/s and 1.45×10^{4} cm/s is used for the Ge/Si and Ge/SiO$_2$ interfaces respectively. These high recombination velocities are due to the lattice mismatch between Ge and Si resulting in a defective Ge/Si interface. However, the Ge/SiO$_2$ interface also has a very high recombination velocity. In principle the latter can be reduced with a proper passivation layer like GeO$_\mathrm{x}$ [8]. This would strongly impact the overall carrier lifetime. For example, if the WG was passivated with GeO$_\mathrm{x}$, whose recombination velocity is $\sim1\times10^{3}$ cm/s, then the carrier lifetime would increase from 1.14 ns to 3.75 ns. This motivated us to explore improved passivation schemes, as will be discussed in the following section.

3.2 Germanium passivation study using time-resolved photoluminescence spectroscopy

In this section, we will investigate blanket (unpatterned) Ge films grown on Si. This reduces the processing complexity and enables a quick study. However, in blanket Ge films, the contribution of the bulk lifetime to the net carrier lifetimes cannot be neglected due to the lower surface/volume ratio compared to the WGs investigated in the previous section. Therefore, to decouple the impact of threading dislocation density (TDD) dependent bulk carrier lifetime from the measured carrier lifetime and to be able to estimate the net surface recombination velocity, first unpassivated blanket Ge films with varying thicknesses are studied. In a second step, the top Ge surface is passivated using 5 different approaches: deposition of SiO_2, 2 types of Si cap and 2 types of GeO_x layers.

3.2.1 Unpassivated blanket Ge films on Si

The Ge films investigated in this section were grown on 300 mm Si (001) substrates using an ASM Epsilon^{TM} 3200 epitaxial reactor [9]. A standard wet clean and in-situ high temperature bake in H_2 at 1050°C were performed to remove any native oxide on the Si substrate. Ge with $\sim$1 μm thickness was grown at 450°C and atmospheric pressure using GeH_4 as the precursor and H_2 as the carrier gas. In order to reduce the TDD arising due to misfits at the Ge/Si interface, the wafers underwent a post-epi anneal in N_2 at 850°C for 3 minutes. The annealing was needed to drop the TDD from about 10^{10} cm^{-2} for as grown layers to (4-5)$\times 10^7$ cm^{-2} [10, 11]. The $\sim$1μm thick Ge layer was thinned down to different thicknesses with the removal of 0.4 μm or 0.8 μm of Ge via chemical mechanical polishing (CMP). As a result, we get a set of 3 samples - Sample A, Sample B and Sample C with a Ge thickness of 0.18 μm, 0.53 μm and 0.96 μm respectively.

The quality of the above Ge layers was determined by performing time resolved photoluminescence (TRPL) spectroscopy using a C12132 compact NIR photoluminescence spectrometer from Hamamatsu. The setup uses a Class 3B - YAG laser with a pump intensity of 127 W/cm^2, a wavelength of 532 nm and a repetition rate of 15 kHz. Fig. 3.8 and Fig. 3.9 show the PL and TRPL response of Sample A, Sample B and Sample C. The PL decay curve was measured using a time -correlated single photon counting method at the peak emission wavelength (around 1600 nm). However, this PL decay contains also the response of the incident pump signal. To extract carrier lifetimes from this decay, the instrument response function is deconvoluted and then the PL lifetime (τ_{PL}) is extracted by fitting an exponential decay. The results are summarized in Table 3.2.

$$\Delta P_{\mathrm{ex}}(t) = \Delta N_{\mathrm{ex}}(t) \propto e^{-t/\tau_{\mathrm{Carr}}} \tag{3.7}$$

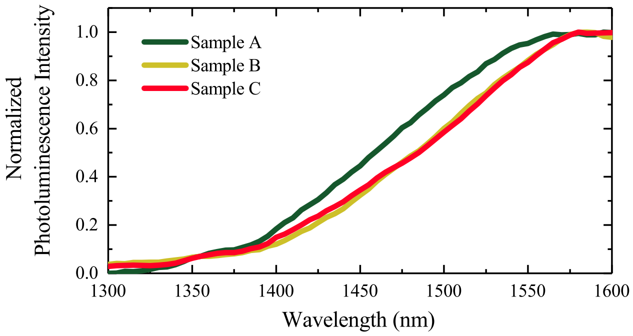

Figure 3.8: PL spectra of all unpassivated Ge samples.

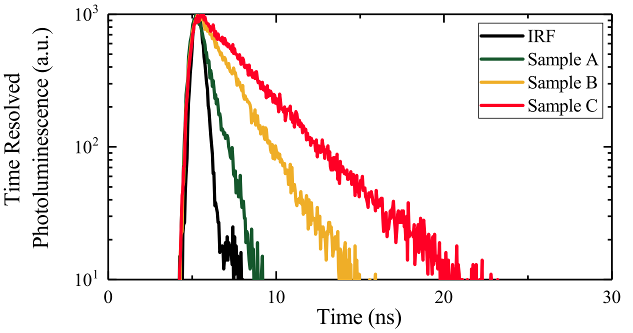

Figure 3.9: Results from time resolved photoluminescence spectroscopy of Ge films of different thickness. The photoluminescence decay was measured at the peak PL emission wavelength determined from the spectra shown in Fig. 3.8, from which. The instrument response function (IRF) represents the temporal signature of the laser pump signal and the response of the experimental setup. The time constant is determined by deconvoluting the measured PL decay with the IRF signal and fitting it with an exponential function.

Sample name	Ge thickness (μm)	τ_{PL} (ns)	τ_{Carr} (ns)
A	0.18 ± 0.015	0.5	1.0
B	0.53 ± 0.013	2.0	4.0
C	0.96 ± 0.022	2.9	5.8

Table 3.2: Summary of carrier lifetimes of unpassivated Ge layers determined using TRPL spectroscopy .

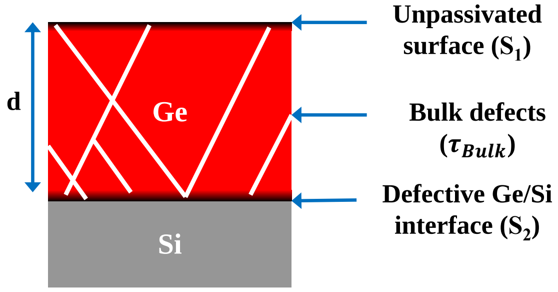

Figure 3.10: Schematic showing defects mediating non-radiative recombination centers in Ge layers. The white lines in this figure schematically represent the threading dislocations in the Ge and the dark regions represent the interface/surface recombination centers.

$$I_{PL}(t)e^{-t/\tau_{\mathrm{PL}}} = R_\Gamma \Delta P_{\mathrm{ex}}(t)\Big(x_\Gamma \Delta N_{\mathrm{ex}}(t)\Big) \propto e^{-2t/\tau_{\mathrm{Carr}}} \tag{3.8}$$

$$\frac{1}{\tau_{Carr}} = \frac{1}{\tau_{Bulk}} + \frac{S_1 + S_2}{d} \tag{3.9}$$

$$\tau_{Bulk} = \frac{1}{\sigma \mathrm{v_{th}} \mathrm{N_T}} \quad \text{with} \quad \mathrm{N_T} = \mathrm{TDD} \times \mathrm{N_D} \tag{3.10}$$

The relationship between the PL lifetime (τ_{PL}) and the carrier lifetime (τ_{Carr}) is $\tau_{\mathrm{Carr}} = 2 \times \tau_{\mathrm{PL}}$ as derived in Eq. 3.7 and Eq. 3.8, where x_Γ represents the fraction of electrons occupying in the Γ valley conduction band [12] and ΔP_{ex}, ΔN_{ex}, I_{PL} and R_Γ are the photo-excited hole density, the photo-excited electron density, the PL intensity and the radiative recombination rate for the Γ valley conduction band respectively. The photo-excited electron and hole density are atleast 3 orders of magnitude larger than intrinsic carrier concentration of Ge.

Given the low pump intensity (127 mW/cm^2), carrier concentration dependent radiative and Auger recombination lifetimes can be ignored. The measured τ_{Carr} is

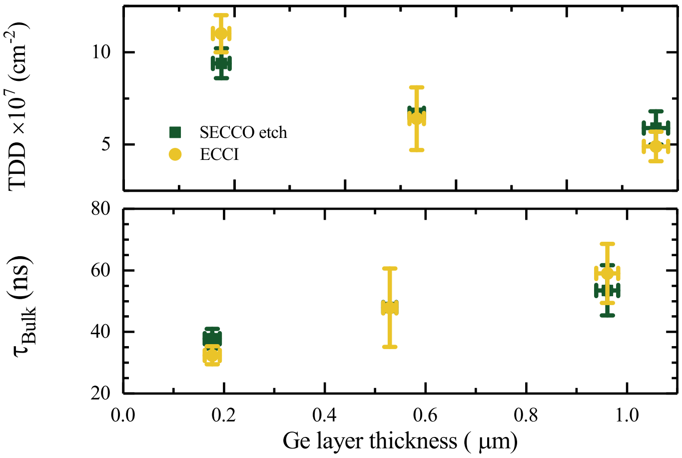

Figure 3.11: Summary of measured TDD with error bars (originating from the measured TDD and the Ge buffer thickness estimation) using SECCO etch and ECCI. The measured TDD shows a dependence on buffer thickness.

dominated by Shockley-Rheed-Hall (SRH) recombination mechanisms with surface and bulk defects the two main sources as illustrated in Fig. 3.10 and are related using Eq. 3.9 [12, 13]. Dangling bonds or border traps at the top surface and Si-Ge intermixing at the bottom Ge/Si interface contribute to these surface recombination lifetimes and are typically quantified in terms of surface recombination velocity ($S_1 + S_2$) while threading dislocations through the bulk of Ge film impact the bulk lifetime. As a result, the bulk Ge lifetime can be determined by estimating the TDD. The latter can be measured using electron channeling contrast imaging (ECCI) or by defect decoration using an etch treatment (SECCO etch) and then counting the etched defects with atomic force microscopy [14, 15]. The TDD estimation using a SECCO etch probes the top 50 nm of the Ge layers. The measured TDD is shown in Fig. 3.11 and the results are summarized in Table 3.3. Sample A has the highest TDD due to thin Ge thickness, whereas Sample B and Sample C have a similar TDD. The bulk lifetime in these samples is estimated using Eq. 3.10 where σ, $\mathrm{v_{th}}$, $\mathrm{N_T}$, TDD and $\mathrm{N_D}$ are the carrier capture cross-section by threading dislocation defects in Ge, the thermal velocity of the carriers in Ge, the total defect density, the threading dislocation density and the number of defects per dislocation respectively [16]. Since the defect density in Sample A will be present in the first $\sim$0.18 μm of the Sample B and C, we integrate the total number of defects through the Ge thickness to estimate the bulk lifetimes as reported in Fig 3.11. Comparing the estimated bulk lifetimes of Fig. 3.11 with the measured lifetimes of Table 3.2, $S_1 + S_2$ is responsible for the measured SRH recombination lifetimes of the

Sample name	Measured τ_{Carr} (ns)	Estimated TDD (cm^2)		Estimated τ_{Bulk} (ns)	Estimated $(\mathrm{S}_1+\mathrm{S}_2)\ \times 10^4$ (cm/s)
		SECCO	ECCI		
A	1.0	9.4×10^7	1.1×10^8	32.0	1.6
B	4.0	6.7×10^7	6.4×10^7	48.0	1.2
C	5.8	5.9×10^7	4.9×10^7	56.0	1.5
		$(S_1+S_2)_{\text{Average}}$			1.4 ± 0.2

Table 3.3: Contribution of bulk and surface recombination lifetimes to the measured carrier lifetime.

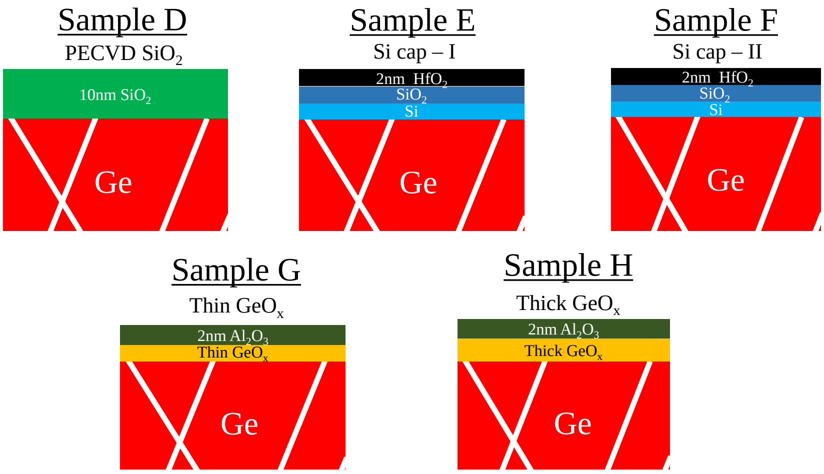

Figure 3.12: Cross-sectional schematic view of the different passivation layers used on our Ge films. Sample E and Sample F have the Si capping layer grown at different temperature. In Sample G and Sample H, GeO$_x$ have different thickness with more details listed in Table 3.4.

films. An average surface recombination velocity of $(1.4 \pm 0.2) \times 10^4$ cm/s was extracted. In the following section we will study the impact of passivation on the carrier lifetime in these Ge layers.

3.2.2 Carrier lifetime of passivated Ge films

As discussed in the previous section, time resolved photoluminescence measurement and TDD analysis of unpassivated Ge shows that the carrier lifetimes are limited by defects at the unpassivated top surface and at the bottom Ge/Si interface. Here, we investigate the influence of different top surface passivation schemes on

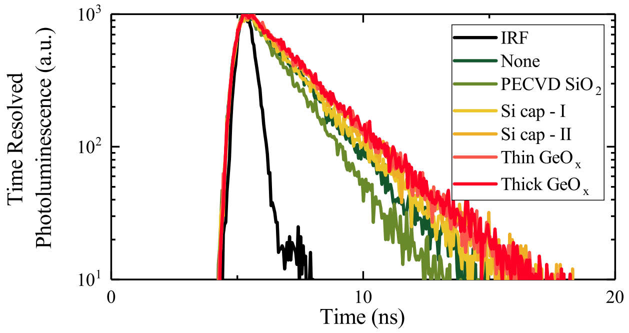

Figure 3.13: Results from time resolved photoluminescence spectroscopy of various passivation schemes.

Sample name	Comments	τ_{Carr} (ns)	S_1+S_2 (cm/s)
B	-	4.0	1.4×10^4
D	10 nm thick SiO_2 deposited at 480°C.	2.5	2.1×10^4
E	6-7 monolayer of Si deposited with Si_4H_{10} at 350°C followed by an ALD process to deposit 2 nm HfO_2 [17].	3.8	1.3×10^4
F	$\sim$1 nm Si deposited with SiH_4 at 500°C followed by deposition of 2nm HfO_2 using an ALD process [18].	4.1	1.2×10^4
G	O_2 oxidation for 4 s followed by an ALD process to deposit of 2 nm Al_2O_3 [19, 20].	3.0	1.7×10^4
H	O_2 oxidation for 1 min followed by an ALD process to deposit of 2 nm Al_2O_3 [19, 20].	4.3	1.2×10^4

Table 3.4: Details of passivation layers deposited on the top surface of Ge films.

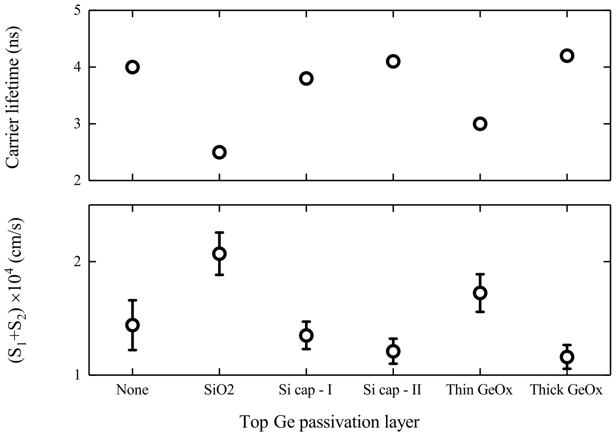

Figure 3.14: Summary of the extracted carrier lifetimes and estimated surface recombination velocities for different passivation schemes.

the carrier lifetime. The passivation layers were deposited on a ~0.6 μm thick Ge layer, similar to Sample B of Table 3.2, and are described in Table 3.4. Sample D has 10 nm of SiO_2 deposited by PECVD, which can be considered similar in terms of passivation to what was used in the Ge-on-Si WGs. The other passivation layers (varieties of a Si and GeO_x) were adopted from the high-K dielectric gate stack studies for Ge pMOSFETs, for which obtaining a low D_{it} (interface state density) gate oxide is important [17–20]. Cross-sectional schematic of the passivation stacks are shown in Fig. 3.12. The Al_2O_3 layer in Samples G and H acts as a diffusion barrier for oxygen to prevent the direct contact of the GeO_x layer with air/water vapor. The PL decay curves are shown in Fig 3.13. To be consistent with Fig. 3.9, the measurements were performed at a pump intensity of 127 mW/cm^2 so that the extracted lifetimes are Shockley-Rheed-Hall recombination limited with negligible influence of radiative and Auger recombination phenomena. Since the underlying Ge layer is nominally undoped, we use the relationship $\tau_{\mathrm{Carr}} = 2\times\tau_{\mathrm{PL}}$ derived from Eq. 3.7 and Eq. 3.8. The extracted carrier lifetimes and surface recombination velocities of these passivated layers are summarized in Table 3.4 and Fig. 3.14 respectively. The standard PECVD SiO_2 has the most dramatic effect on the top surface resulting in the lowest carrier lifetime of 2.5 ns and an extracted $S_1 + S_2$=2.1×10^4 cm/s. Passivation with either a Si cap or a thick GeO_x layer gave the highest carrier lifetimes of up to 4.3 ns. For these layers $S_1 + S_2$ as low as 1.2×10^4 cm/s was estimated. There is a distinct difference between the thin and the thick GeO_x interfaces (Sample G and H). The sample with the thin GeO_x has a high density of interface trap defects, which gets reduced as we increase the layer thickness beyond 2 nm. This is also evident from the carrier lifetime measurement [20]. In summary, the longest carrier lifetime that can be obtained for this 0.6 μm thick Ge is 4.3 ns, which correspond to 3.3 ns for a 0.4 μm thick and 1 μm wide Ge waveguide.

3.3 Summary

In this chapter, we investigated the carrier lifetimes of undoped Ge integrated in a waveguide using pump-probe spectroscopy and of blanket Ge films grown on Si using time-resolved photoluminescence spectroscopy . Ge-on-Si WGs with cross-sectional dimensions of 0.375×1.0 μm^2 have a lifetime of 1.14 ns. The Ge/SiO_2 interface and Ge/Si interface are thereby the 2 limiting recombination centers with interface recombination velocity of 1.45×10^4 cm/s and 0.95×10^4 cm/s respectively. In an effort to find a passivation layer that could replace the existing SiO_2 cladding layer, we found a Si cap or a thick GeO_x to be suitable candidates that can potentially improve the lifetime in the Ge WGs from 1.14 ns to 3.3 ns with the bottom Ge/Si interface being the limiting factor. These lifetimes are below the target of 10 ns defined in chapter 2 and we expect them to drop further with the introduction of dopants due to point defects. This will be investigated in the following 2 chapters.

References

[1] Philippe Absil, Peter De Heyn, Hongtao Chen, Peter Verheyen, Guy Lepage, Marianna Pantouvaki, Jeroen De Coster, Amit Khanna, Youssef Drissi, Dries Van Thourhout, and Joris Van Campenhout. *Imec iSiPP25G silicon photonics: a robust CMOS-based photonics technology platform*, 2015.

[2] S. A. Srinivasan, M. Pantouvaki, P. Verheyen, G. Lepage, P. Absil, J. Van Campenhout, and D. Van Thourhout. *Extraction of carrier lifetime in Ge waveguides using pump probe spectroscopy*. Applied Physics Letters, 108(21):211101, 2016.

[3] Xiaochen Sun, Jifeng Liu, Lionel Kimerling, and Jurgen Michel. *Optical Bleaching of Thin Film Ge on Si*. ECS Transactions, 16(10):881–889, 2008.

[4] R. K. Schaevitz, D. S. Ly-Gagnon, J. E. Roth, E. H. Edwards, and D. A. B. Miller. *Indirect absorption in germanium quantum wells*. AIP Advances, 1(3):032164, 2011.

[5] Lee Carroll, Peter Friedli, Stefan Neuenschwander, Hans Sigg, Stefano Cecchi, Fabio Isa, Daniel Chrastina, Giovanni Isella, Yuriy Fedoryshyn, and

Jérôme Faist. *Direct-Gap Gain and Optical Absorption in Germanium Correlated to the Density of Photoexcited Carriers, Doping, and Strain*. Phys. Rev. Lett., 109:057402, Aug 2012.

[6] S.L. Chuang. *Physics of Photonic Devices*. Wiley Series in Pure and Applied Optics. John Wiley & Sons, 2009.

[7] Jifeng Liu, Xiaochen Sun, Dong Pan, Xiaoxin Wang, Lionel C. Kimerling, Thomas L. Koch, and Jurgen Michel. *Tensile-strained, n-type Ge as a gain medium for monolithic laser integration on Si*. Opt. Express, 15(18):11272–11277, Sep 2007.

[8] Yen-Yu Chen, H-C Chang, Y-H Chi, C-H Huang, and CW Liu. *GeO_2 Passivation for Low Surface Recombination Velocity on Ge Surface*. IEEE Electron Device Letters, 34(3):444–446, 2013.

[9] Gang Wang, Frederik E. Leys, Laurent Souriau, Roger Loo, Matty Caymax, David P. Brunco, Jef Geypen, Hugo Bender, Marc Meuris, Wilfried Vandervorst, and Marc M. Heyns. *Selective Epitaxial Growth of Germanium on Si Wafers with Shallow Trench Isolation: An Approach for Ge Virtual Substrates*. ECS Transactions, 16(10):829–836, 2008.

[10] V. Terzieva, L. Souriau, M. Caymax, D.P. Brunco, A. Moussa, S. Van Elshocht, R. Loo, F. Clemente, A. Satta, and Marc Meuris. *Benefits and side effects of high temperature anneal used to reduce threading dislocation defects in epitaxial Ge layers on Si substrates*. Thin Solid Films, 517(1):172 – 177, 2008. Fifth International Conference on Silicon Epitaxy and Heterostructures (ICSI-5).

[11] G. Wang, R. Loo, E. Simoen, L. Souriau, M. Caymax, M. M. Heyns, and B. Blanpain. *A model of threading dislocation density in strain-relaxed Ge and GaAs epitaxial films on Si (100)*. Applied Physics Letters, 94(10):102115, 2009.

[12] Donguk Nam, Ju-Hyung Kang, Mark L. Brongersma, and Krishna C. Saraswat. *Observation of improved minority carrier lifetimes in high-quality Ge-on-insulator using time-resolved photoluminescence*. Opt. Lett., 39(21):6205–6208, Nov 2014.

[13] Shinichi Saito, Frederic Yannick Gardes, Abdelrahman Zaher Al-Attili, Kazuki Tani, Katsuya Oda, Yuji Suwa, Tatemi Ido, Yasuhiko Ishikawa, Satoshi Kako, Satoshi Iwamoto, et al. *Group IV light sources to enable the convergence of photonics and electronics*. Frontiers in Materials, 1:15, 2014.

[14] Martin A Crimp. *Scanning electron microscopy imaging of dislocations in bulk materials, using electron channeling contrast.* Microscopy research and technique, 69(5):374–381, 2006.

[15] Yuji Yamamoto, Peter Zaumseil, Tzanimir Arguirov, Martin Kittler, and Bernd Tillack. *Low threading dislocation density Ge deposited on Si (100) using RPCVD.* Solid-State Electronics, 60(1):2–6, 2011.

[16] Cor Claeys and Eddy Simoen. *Fundamental and technological aspects of extended defects in Germanium.* Springer.

[17] Matty Caymax, Frederik Leys, Jerome Mitard, Koen Martens, Lijun Yang, Geoffrey Pourtois, Wilfried Vandervorst, Marc Meuris, and Roger Loo. *The influence of the epitaxial growth process parameters on layer characteristics and device performance in Si-passivated Ge pMOSFETs.* Journal of The Electrochemical Society, 156(12):H979–H985, 2009.

[18] B Vincent, R Loo, Wilfried Vandervorst, Jeroen Delmotte, B Douhard, VK Valev, Maarten Vanbel, Thierry Verbiest, J Rip, B Brijs, et al. *Si passivation for Ge pMOSFETs: Impact of Si cap growth conditions.* Solid-State Electronics, 60(1):116–121, 2011.

[19] E Simoen, J Mitard, Geert Hellings, Geert Eneman, B De Jaeger, L Witters, B Vincent, R Loo, A Delabie, S Sioncke, et al. *Challenges and opportunities in advanced Ge pMOSFETs.* Materials Science in Semiconductor Processing, 15(6):588–600, 2012.

[20] Laura Nyns, Dennis Lin, Guy Brammertz, Florence Bellenger, Xiaoping Shi, Sonja Sioncke, Sven Van Elshocht, and Matty Caymax. *Interface and border traps in Ge-based gate stacks.* ECS Transactions, 35(3):465–480, 2011.

4

Characterization of P-doped Ge on 1μm Ge buffer

In this chapter, we will present the results of characterization experiments performed on highly n-type doped Ge grown on Si.

4.1 Material characterization of P-doped Ge

As discussed in Chapter 2 high n-type doping using Phosphorus dopants makes Ge a pseudo direct band gap material and allows for the reduction of the threshold current density required for lasing operation. As the doping concentration reaches beyond 1×10^{19} cm^{-3}, the fermi level is pushed into the L conduction valley of Ge making it degenerate. It reaches the Γ conduction valley when the doping level is as high as 9×10^{19} cm^{-3} for unstrained Ge and 7.5×10^{19} cm^{-3} for 0.2% biaxial tensile strained Ge as demonstrated in Section 2.1.2. Phosphorous is therefore the preferred dopant as it has the highest solubility limit among all the other n-type dopants. However, the required doping levels still exceed the maximal solubility limit of Phosphorus in Ge, which is around 7×10^{19} cm^{-3} at 800°C [1].

A possible way to achieve higher P concentrations is by driving the epitaxy process out of equilibrium as demonstrated using the delta doping technique where an active P concentration as high as 2×10^{20} cm^{-3} was achieved. These layers were grown with P_2 (for molecular beam epitaxy) or PH_3 (for chemical vapour deposition) as the dopant precursors. Delta-doped layers with electrically active P concentration of up to 1×10^{20} cm^{-3} have been reported in the delta doped regions of Ge [2–4]. In order to have uniformly distributed dopants across the entire Ge region, cyclic annealing was performed where the active phosphorus concentrations dropped to 4×10^{19} cm^{-3} [2]. Since this process requires cyclic deposition of Ge and P atoms at temperatures that are varied from 500°C for Ge deposition and room temperature for P incporporation, the throughput of the growth process is dramatically reduced. On the other hand, using conventional in-situ doped Ge grown using chemical vapour deposition, with GeH_4 and PH_3 as the precursors, resulted in electrically active P concentration of 2×10^{19} cm^{-3} [5, 6]. These layers were grown at 400°C. On reducing the growth temperature further, the epitaxy process moves into a non-equilibrium state. This can enable an increase in the active P concentration. Also the use of Ge_2H_6 as a higher order Ge precursor gas [7] can facilitate higher P incorporation. In addition, this in-situ doping allows for high wafer throughput due to the simultaneous deposition of Ge and P atoms. Therefore the impact of growth conditions, like partial pressure (pp) ratio of precursor gases (ppPH_3 - partial pressure of PH_3 and ppGe_2H_6 - partial pressure of Ge_2H_6) and the growth temperature, on the activation of P dopants in Ge, using an in-situ doping process, will be investigated in the next section.

4.1.1 As grown P-doped Ge layers

The P-doped Ge layers studied in this thesis were grown in an ASM-Intrepid XP^{TM} epi tool where Ge_2H_6 (diluted to 1% in H_2) and PH_3 (diluted to 5% in He) were used as the gas precursors. The P-doped Ge layers were grown on 1 μm thick Ge buffer layers used as virtual substrates [8]. These buffer layers were grown on 300 mm Si (001) substrates. The buffer layers exhibit a 0.16% biaxial tensile strain, as confirmed with the help of X-ray diffraction. The in-situ P-doped Ge layers were later grown with a fixed Ge_2H_6 flow at a reduced pressure of 10 Torr (=1.3 kPa). The doping level was modified by tuning the PH_3 gas flow rate. In addition, the growth temperature was varied from 320°C to 550°C and the samples were analyzed using secondary ion mass spectroscopy (SIMS) and a micro hall effect (MHE) measurement to extract the chemical and active P concentrations respectively [9]. A Hall scattering factor of 1 was assumed. This could result in an error of maximum 10% in the extracted carrier concentrations [10]. The crystallinity of the layers was first gauged by examining the microscope images of the top surface and later with the help of photoluminescence spectroscopy.

Fig. 4.1 shows the extracted chemical and active P concentrations for layers grown at 320°C, 425°C and 550°C. The amount of P incorporated in Ge increases monotonically with the increase of the ppPH_3/ppGe_2H_6 ratio with the images of surface morphology shown in Fig. 4.2. However, for higher growth temperatures, it begins to saturate with the maximum achieved at 320°C. For concentrations up

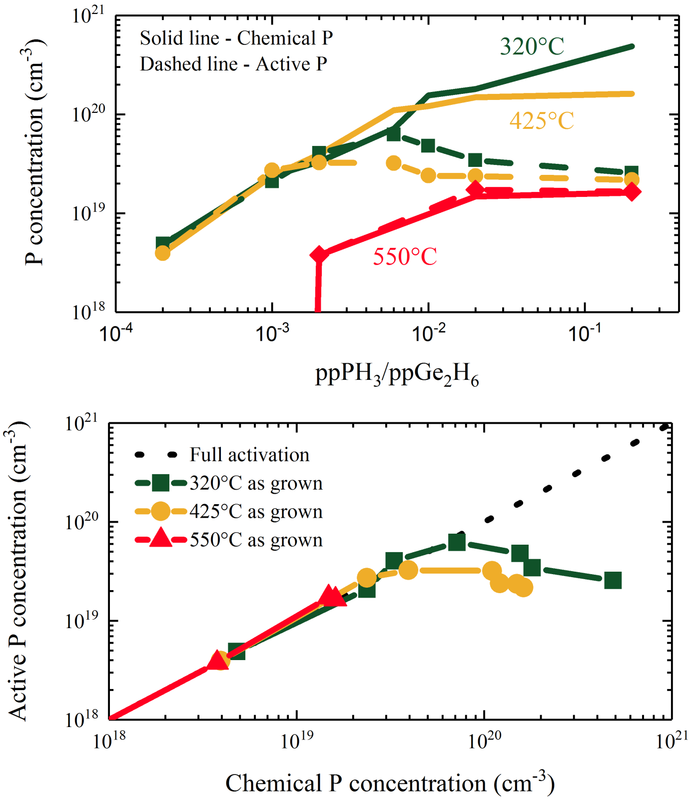

Figure 4.1: Top figure: Chemical and active P concentration estimated by SIMS and MHE measurements respectively for varying partial pressure ratio of PH_3 and Ge_2H_6 ($ppPH_3/ppGe_2H_6$). Bottom figure: Active P concentration plotted as function of chemical P concentration with the dashed line representing 100 % activation.

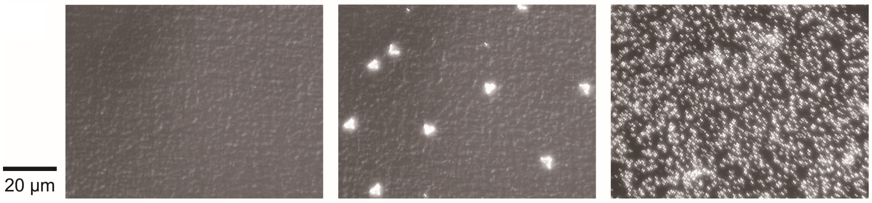

pp ratio = 0.01
Chemical P concentration
= 1.6×10^{20} /cm^3

pp ratio = 0.02
Chemical P concentration
= 1.8×10^{20} /cm^3

pp ratio = 0.2
Chemical P concentration
= 4.9×10^{20} /cm^3

Figure 4.2: Surface morphology of P-doped Ge layers with different ratios of $ppPH_3/ppGe_2H_6$, grown at 320° C [7].

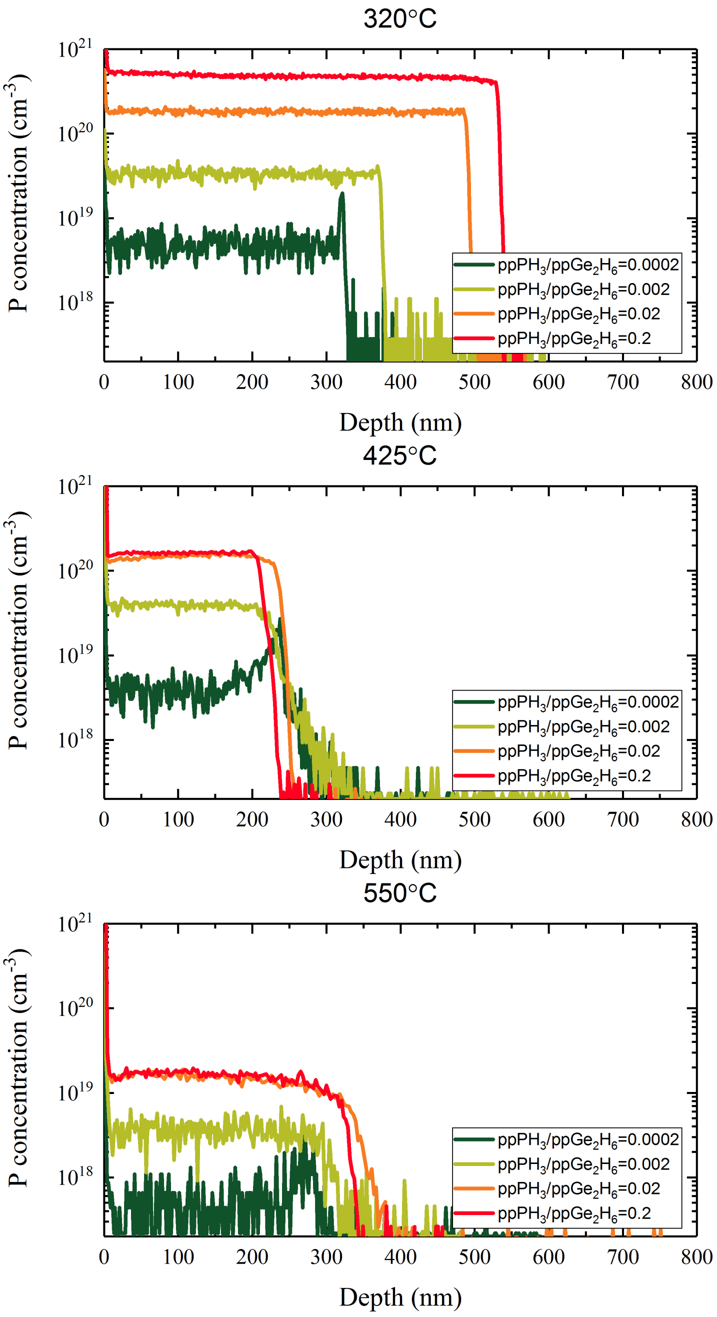

Figure 4.3: Chemical depth profile for P in uniformly doped Ge layers grown at different temperatures as measured using secondary ion mass spectroscopy (SIMS).

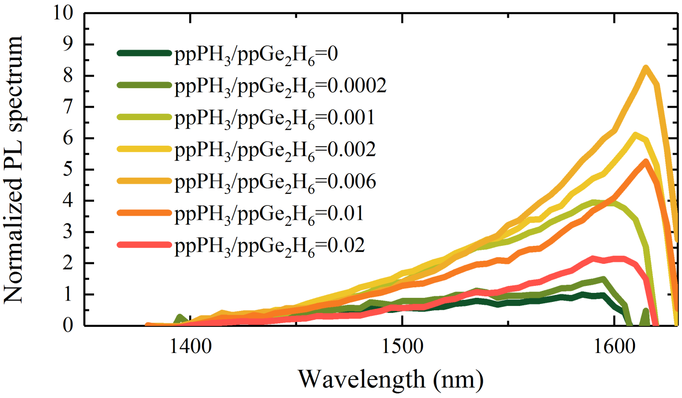

Figure 4.4: PL spectra for P-doped Ge layers grown with increasing ppPH$_3$/ppGe$_2$H$_6$ ratio at 320°C. The PL spectra were normalized with the responsivity of the detector in the PL setup and with the peak PL intensity from undoped Ge. The detector has a cutoff at 1620 nm.

to 6.2×10^{19} cm^{-3}, also the active P content increases linearly with the chemical P content resulting in 100% activation. For higher ppPH$_3$/ppGe$_2$H$_6$ concentration, the active dopant concentration began to saturate and ultimately even to decrease. From Fig. 4.1, the maximum attainable active P concentrations at 320°C, 425°C and 550°C were 6.2×10^{19} cm^{-3}, 3.3×10^{19} cm^{-3} and 1.7×10^{19} cm^{-3} respectively. The solubility limit of P in Ge is around 1×10^{19} cm^{-3} at 320°C, 1.5×10^{19} cm^{-3} at 425°C and 2.8×10^{19} cm^{-3} at 550°C. This shows the reduction of the temperature pushes the growth process away from the equilibrium condition and increases the maximum attainable active P concentration in Ge beyond the solubility limit. While analyzing the SIMS profile of P atoms in the uniformly doped Ge layers in Fig. 4.3, a gradual P diffusion towards the virtual substrate can be observed at higher growth temperatures. The low diffusion coefficient of P in Ge at lower growth temperature allows for an abrupt dopant profile as observed at 320°C.

With doping levels reaching 6.2×10^{19} cm^{-3}, these Ge layers should exhibit a pseudo direct band gap behavior and become an efficient light emitter. This was investigated with a photoluminescence (PL) measurement at room temperature, using a continuous wave laser as the pump at 640 nm with an intensity of 410 mW/cm^2. The PL signal is measured using an near infrared spectrometer with a Hamamatsu R5509-72 NIT photomultiplier tube detector whose cutoff is at 1600-1620 nm. The measured PL spectrum for the P-doped Ge layers grown at 320°C is shown in Fig. 4.4. The PL drops dramatically for wavelengths beyond 1620 nm

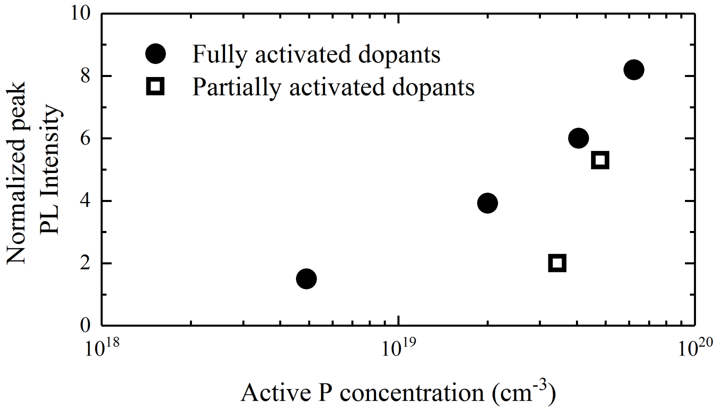

Figure 4.5: Peak PL intensity as a function of the active P concentration for P-doped Ge layers.

due to the detector cut-off. For the undoped samples, the PL intensity shows very similar responses, independent of the growth temperature. Therefore, the spectra from all doped samples were normalized with respect to the peak intensity of the undoped samples. It is worth noting that we expect the peak PL position to shift towards longer wavelengths with the increase in doping level due to dopant dependent band gap narrowing. This cannot be measured here though due to the detector cutoff [14–17]. Nevertheless, an increase in peak PL intensity was observed with an increase in active P concentration as long as they are fully activated as can be seen in Fig. 4.5. This trend is consistent with the PL enhancement shown in [6, 18–20]. Since dopant associated electrons occupy the L-conduction valley, a large fraction of the photo excited electrons will occupy the Γ-conduction valley, as illustrated in Fig. 2.5, resulting in an increased PL. The highest PL intensity, with 8× PL enhancement, was measured for the highest doped Ge layer. On the other hand, the enhancement reduces for partially activated dopants in Ge due to the increase in point defects. For example, the PL enhancement from the sample grown with $ppPH_3/ppGe_2H_6$ ratio = 0.01 is 2.5× higher than that of the sample with $ppPH_3/ppGe_2H_6$ ratio = 0.02 because the former sample is fully activated and the latter is partially activated. The impact of point defect densities on the PL enhancement suggests the need for the development of a rapid thermal annealing strategy that improves the crystallinity of the P-doped layers.

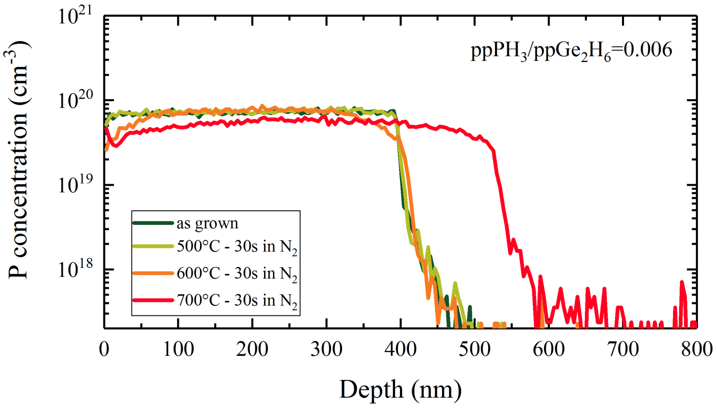

Figure 4.6: SIMS profile of P atoms in samples grown with $ppPH_3/ppGe_2H_6$=0.006 and rapid thermal annealed in N_2 at 500° C, 600° C and 700° C for 30 seconds.

4.1.2 Rapid thermal annealing of P-doped Ge layers

In order to reduce the point defect density associated with the P dopants, rapid thermal annealing was performed. For example, samples grown with $ppPH_3/ppGe_2H_6$ = 0.006 and 0.02 at 320°C were annealed at different temperatures and time duration as shown in Table 4.1, and were analyzed using SIMS, MHE measurements and PL spectroscopy. The SIMS profile provides the impact of dopant diffusion due to annealing, whereas PL enhancement reflects the impact of annealing on the crystallinity. The results for the $ppPH_3/ppGe_2H_6$ = 0.006 sample annealed at temperatures 500°C to 700°C for 30 seconds in N_2 are shown in Fig. 4.6 and Fig. 4.7. On comparing the results, it is evident that RTA at 700°C for 30 seconds had the most impact on both the SIMS profile and the PL enhancement. This anneal resulted in dopant diffusion of roughly 150 nm into the underlying 1 μm Ge buffer, but also improved the PL enhancement from 8× for the as grown layers to 10× for the annealed layers. Even though RTA at 500°C and 600°C did not modify the chemical P profile in the stack, they seem to have suppressed the PL intensity from the as grown sample. Moreover, even though RTA at 700°C gave the lowest active P concentration, the fact that the highest PL enhancement was extracted from this sample shows the importance of annealing and the impact of annealing temperature on the emission properties of these P-doped Ge layers.

Since dopant diffusion was evident for the samples annealed at 700°C , the RTA-process at higher temperatures was performed for the layers grown with a $ppPH_3/ppGe_2H_6$=0.02 ratio, as the chemical P content in this layer is relatively high. Also, each time the temperature was increased by 50°C, over the range

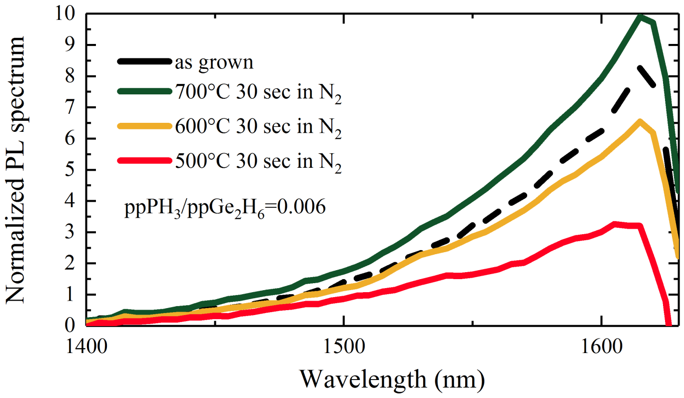

Figure 4.7: Normalized PL spectra of rapid thermal annealed samples in Fig. 4.6.

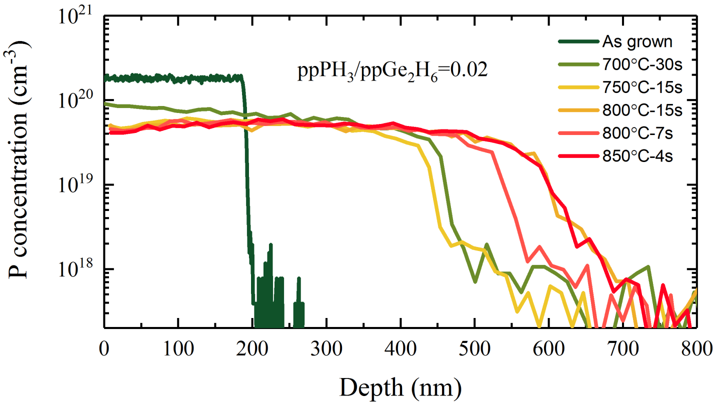

Figure 4.8: SIMS profile of P atoms in samples grown with $ppPH_3/ppGe_2H_6$=0.02 and rapid thermal annealed in N_2 from 700°C to 850°C just below the melting point of Ge.

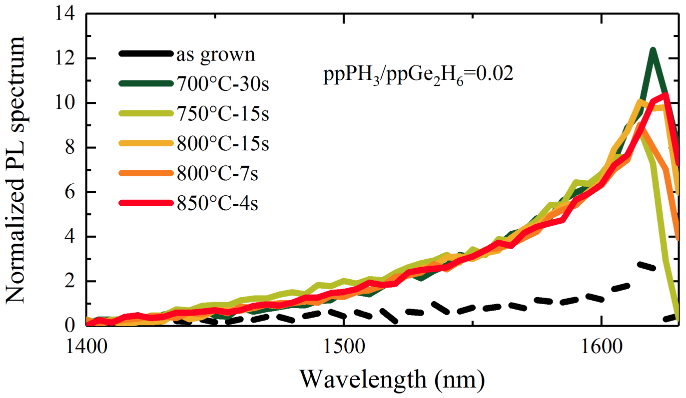

Figure 4.9: Normalized PL spectra of rapid thermal annealed samples in Fig. 4.8.

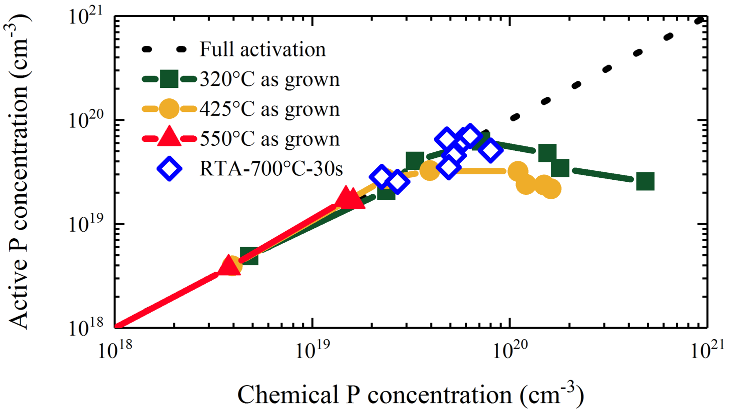

Figure 4.10: Active P concentration plotted as a function of chemical P concentration for as grown and annealed samples with the dashed line representing 100 % activation.

$ppPH_3/ppGe_2H_6$ ratio	RTA Temp (°C)	RTA time (s)	Chem P before RTA (cm^{-3})	Active P before RTA (cm^{-3})	Chem P after RTA (cm^{-3})	Active P after RTA (cm^{-3})
0.006	500	30	7.1×10^{19}	6.3×10^{19}	7.3×10^{19}	4.7×10^{19}
0.006	600	30	7.1×10^{19}	6.3×10^{19}	6.7×10^{19}	5.5×10^{19}
0.006	700	30	7.1×10^{19}	6.3×10^{19}	5.2×10^{19}	4.5×10^{19}
0.02	700	30	1.8×10^{20}	3.5×10^{19}	8×10^{19}	5.1×10^{19}
0.02	750	15	1.8×10^{20}	3.5×10^{19}	5.9×10^{19}	5.9×10^{19}
0.02	800	15	1.8×10^{20}	3.5×10^{19}	4.9×10^{19}	5.5×10^{19}
0.02	800	7	1.8×10^{20}	3.5×10^{19}	4.9×10^{19}	4.5×10^{19}
0.02	850	4	1.8×10^{20}	3.5×10^{19}	5.4×10^{19}	5.0×10^{19}

Table 4.1: List of conditions used for rapid thermal annealing experiments and extracted active and chemical P concentration.

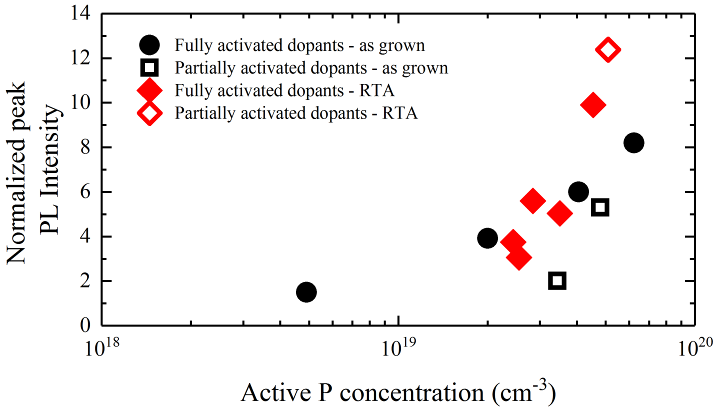

Figure 4.11: Normalized PL enhancement of rapid thermal annealed and as grown samples as function of active P concentration. The results are for samples with RTA at 700°C for 30 seconds in N_2. For highly doped samples, RTA improves the PL enhancement by reducing point defects associated with P dopants.

750°C to 850°C, the duration of the anneal was reduced by a factor 2, to control the dopant diffusion. The SIMS profile and PL spectrum of the layers annealed at 5 different conditions are shown in Fig. 4.8 and Fig. 4.9. The extent of dopant diffusion for samples annealed at 700°C for 30s and annealed at 750°C for 15s remained the same as the time duration was halved. The P concentration profile of 800°C for 15s results in dramatic over diffusion of dopants into the underlying 1 μm Ge virtual substrate when compared to 800°C for 7 seconds due to the extra 8 seconds. Hence, for every increase in temperature by 50°C, the annealing time was halved. In spite of this, for temperatures above 750°C, higher dopant diffusion was observed as the ramp-up and ramp-down time of the annealing furnace also plays an important role in the dopant diffusion process. As a result, the active P concentration in all these layers is around 5×10^{19} cm^{-3}. On comparing the PL spectra shown in Fig. 4.9, the enhancement remained unchanged and constant, within the spectral range that could be measured. This suggests that all these annealed samples had similar crystalline quality. Since the dopant diffusion was the least for the RTA at 700°C-30s, these conditions were used for annealing the remaining set of samples. The normalised peak PL intensity of all these samples is included in Fig. 4.11. When comparing with as-grown samples, rapid thermal annealing plays a critical role for highly doped layers where the point defect density is high. In the next section, time resolved photoluminescence spectroscopy and photoluminescence spectroscopy using an extended-InGaAs detector with responsivity up to 2 μm will be performed, to study the influence of doping on the carrier

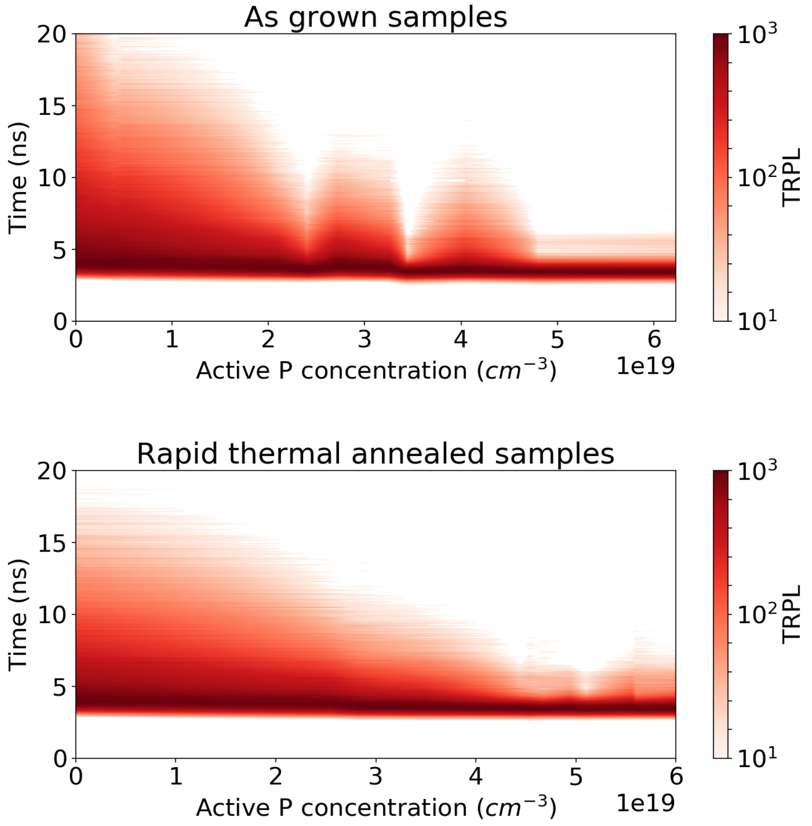

Figure 4.12: Contour plot of time resolved photoluminescence response from P-doped Ge samples as a function of active P concentration in the layer. Only the samples with activation $>$ 90% were considered. With the increase in active doping, the photoluminescence response decay drops quickly.

lifetime and spectral width of the PL spectra.

4.2 Optical characterization of P-doped Ge

4.2.1 Time resolved photoluminescence

The strong increase in PL enhancement with rapid thermal annealing for highly doped Ge layers shows the importance of the point defects. Time resolved photoluminescence (TRPL) spectroscopy (similar to the results presented in Section

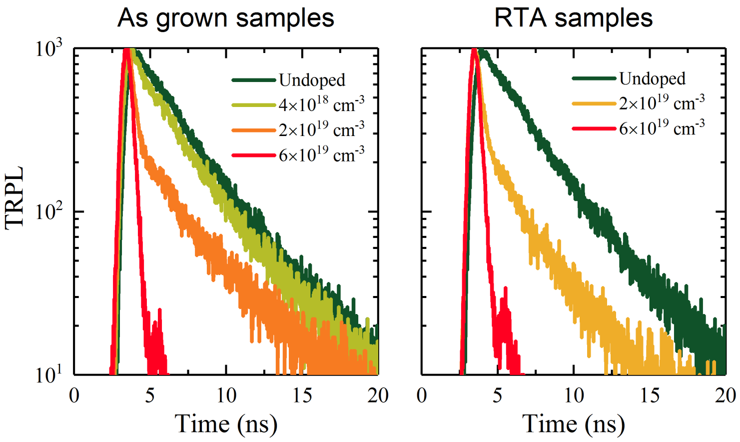

Figure 4.13: Time resolved photoluminescence response of Ge layers taken from Fig. 4.12 for a few doping levels. The PL decays faster with increase in active P concentration.

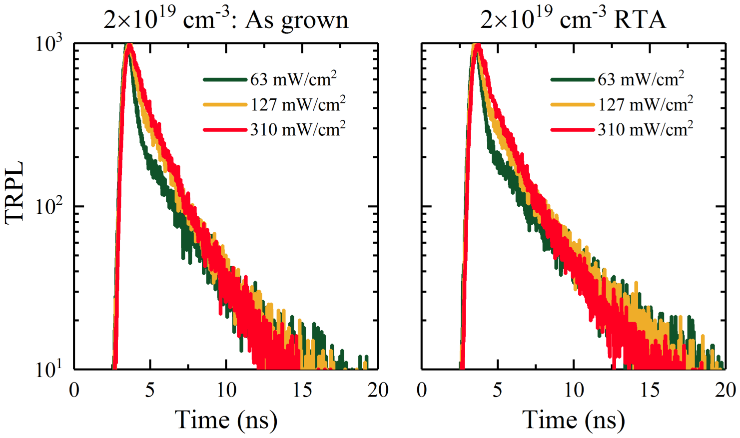

Figure 4.14: Time resolved photoluminescence response of 2×10^{19} cm^{-3} doped Ge layers taken from Fig. 4.12 measured at different pump power levels.

3.2) is additionally performed on all as-grown and rapid thermal annealed samples shown in Fig. 4.10. The TRPL response of Ge layers with fully activated doping levels are plotted in Fig. 4.12 and Fig. 4.13. These figures show that the carrier lifetime in these layers is severely impacted by the increasing dopant concentration. The trends for both as grown and rapid thermal annealed samples are similar. While carefully examining the response of layers with intermediate doping levels, e.g. for the as grown sample with doping level 2×10^{19} cm^{-3} shown in Fig. 4.13, it can be seen that the decay has 2 time constants. This could suggest the presence of carrier density dependent recombination mechanism. Typically, the fast decay component corresponds to Auger recombination and the slower decay component is associated with defects. These 2 decay components have been observed in [21, 22]. In that case one would expect that on increasing the pump intensity, one increases the photo-excited carrier concentration in the Ge layer, resulting in a shorter time constant. But in these samples, the TRPL curves show an opposite trend where only one time constant in its decay and is observed at the highest pump intensity. The layers are pumped using a 532 nm laser source with a penetration depth of 20 nm. However, the high concentration of photo-excited carrier initially excited in the top of the layer typically diffuse across the entire stack in 200 ps [21]. Since the P-doped Ge layer is grown on a 1 μm thick Ge virtual substrate, we believe that the stack can be viewed as being composed of two light emitting sources: the top doped Ge layer and the underlying Ge virtual substrate. The concentration of carriers available for diffusion in the underlying virtual substrate drops with the reduction in pump power. Therefore, the magnitude of the TRPL response originating from the underlying buffer is reduced resulting in 2 time constants. At high optical pump intensity, the TRPL response from the virtual substrate dominates the total decay as shown in Fig. 4.14, giving us the carrier lifetime at the top P-doped Ge layer. Therefore, we focus on the results obtained with low optical pump intensity (63 mW/cm^2). As the doping level increases beyond 2×10^{19} cm^{-3}, the short time constant begins to dominate the total TRPL response. This is due to the high non-radiative recombination rate at the top P-doped Ge layer that reduces the concentration of carriers diffusing to the underlying virtual substrate. It is evident that with increase in carrier concentration, for both as grown and rapid thermal annealed samples, the carrier lifetime drops to the sub ns range. To quantify the carrier lifetimes, uniformly doped Ge layers without any underlying undoped region will be investigated in the next chapter.

4.2.2 Band gap narrowing and spectral broadening

As reported in Section 4.1, the photoluminescence spectra of the Ge layers were first measured using a detector whose responsivity drops dramatically beyond 1620 nm. This limits the measurement wavelength range, making it impossible to deter-

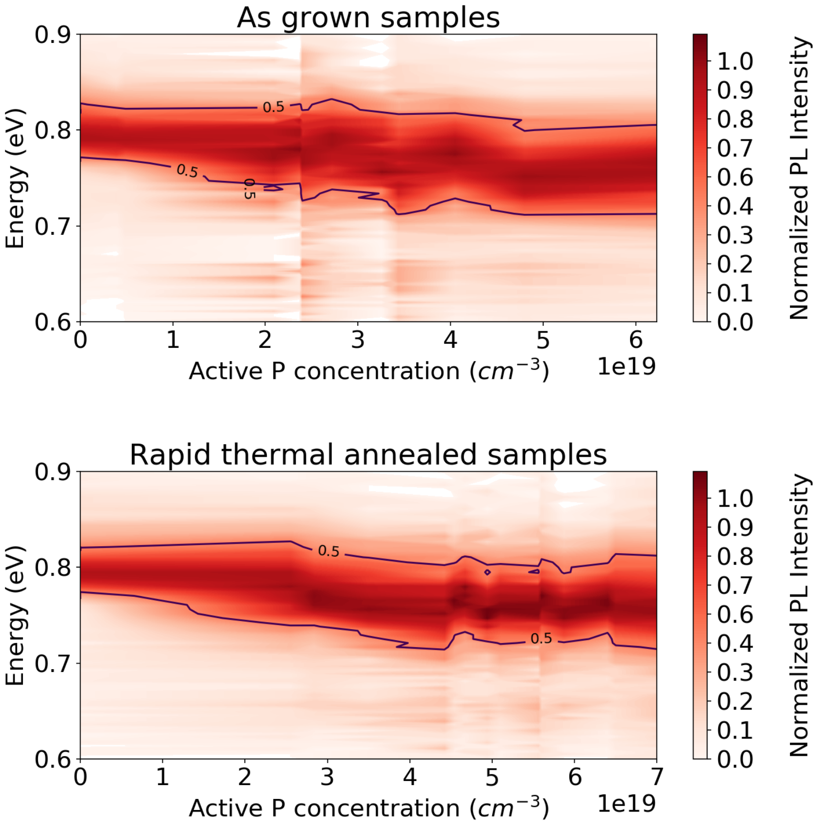

Figure 4.15: Normalized photoluminescence spectra from all doped Ge layers grown on 1 μm thick Ge virtual substrate. The measurements were performed on as grown and rapid thermal annealed samples, pumped with an intensity of 30 kW/cm^2.

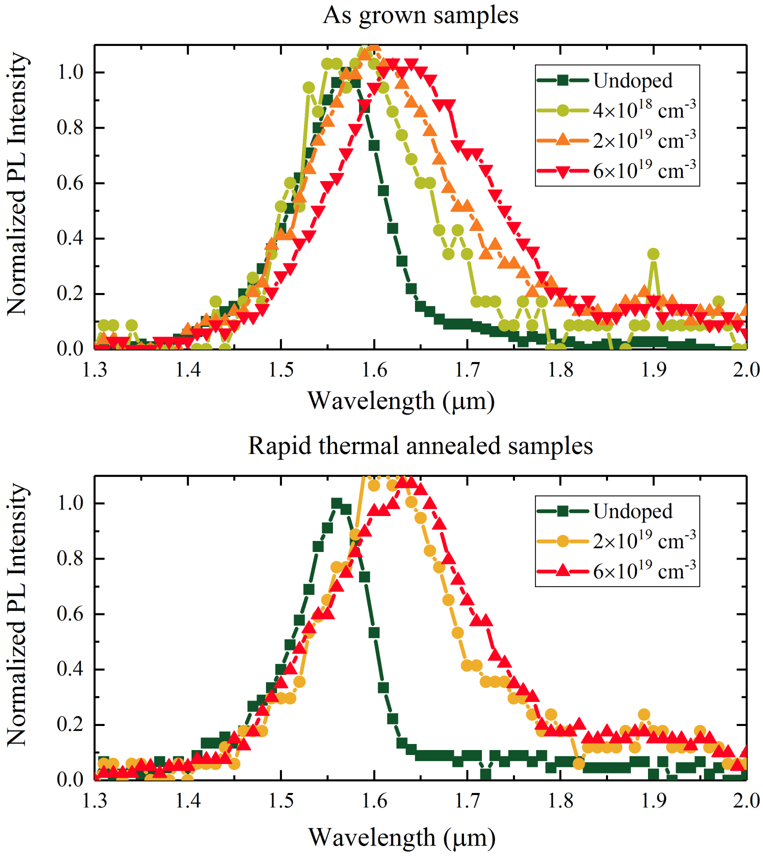

Figure 4.16: Normalized photoluminescence spectra of Ge layers taken from Fig. 4.15 for a few doping levels.

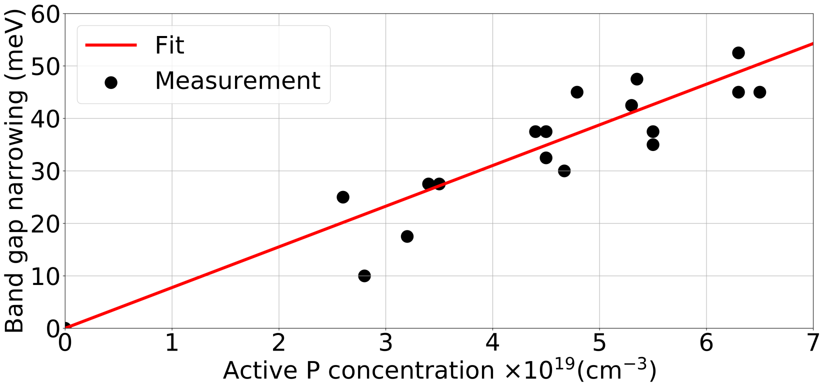

Figure 4.17: Band gap narrowing as function of active P concentration in Ge layers [16].

mine the peak PL emission wavelength and the dopant induced band gap narrowing accurately. Along with the carrier lifetime assessment and the PL enhancement presented earlier in this chapter, information on the full width at half maximum of the PL spectrum can be used to assess the crystalline quality of the material. Therefore, the PL measurement was repeated using a μPL setup, similar to the one presented in [23], at room temperature. A frequency doubled Nd:YAG continuous wave (CW) laser at 2.33 eV (532 nm wavelength) was used as the pump source. The PL signal was collected through the same objective and detected using a liquid nitrogen cooled extended InGaAs detector from Hamamatsu (G7754-03) connected to a monochromator (MS257, Newport). With this detector, the setup allows to measure the PL response over a wavelength range from 1.3 μm to 2.0 μm (0.62 to 0.95 eV) with a maximum pump intensity of 30 kW/cm^2.

The room temperature PL spectra of doped and undoped Ge are shown in Fig. 4.15 and Fig. 4.16. These PL spectra are normalized with the detector responsivity to their peak intensity to compare their shape. Comparing the spectra from doped and undoped Ge, it is obvious that the PL peak shifts to lower energies with the increase in doping level. This is a clear indication of the presence of dopant induced bandgap narrowing where the relative change in the band gap is plotted in Fig. 4.17 and fitted with a polynomial equation of first order.

$$\mathrm{E_g(N_D)} - \mathrm{E_g(N_D = 0)} = \Delta_{\mathrm{BGN}} \times \mathrm{N_D} \qquad (4.1)$$

In the above equation, $\mathrm{E_g}$ is the band gap of Ge, $\mathrm{N_D}$ is the doping level in Ge and Δ_{BGN} is the rate at which the band gap reduces as function of the dopant level. We found Δ_{BGN}=7.7×10^{-19} meV cm^3 is in-line with the results presented in [16]. Apart from dopant induced band gap narrowing effects, we also found that the PL spectra from the doped layers are significantly broader than the spectrum of the undoped Ge layer. The broadening effect was observed in both as-grown and rapid thermal annealed samples whereby the broadening increased with increasing doping level of the top Ge layer. This broadening can be associated with intravalley and intervalley scattering effects originating from ionized P dopants and can typically be modelled using many-body-effect physics [24–26]. Presence of such scattering events affects the absorption and gain spectra of the material and can increase the threshold current density by reducing the efficiency of the laser by a factor > 4. In the next chapter, the impact of dopants on the carrier lifetime and linewidth broadening of Ge will be studied in more detail by investigating uniformly doped Ge layers on Si.

4.3 Summary

In this chapter, we investigated high n-type doped Ge layers that were grown on a 1 μm thick Ge virtual substrate with Ge_2H_6 and PH_3 as precursors gas for in-situ doping. An active P concentration up to 6.2×10^{19} cm^{-3} with 100% activation was obtained for layers grown at 320°C, without any annealing step. These samples emitted $>8\times$ higher PL intensity compared to undoped Ge, confirming the pseudo direct band behaviour associated with the presence of n-type dopants. These samples were later rapid thermal annealed at different temperatures ranging from 500°C to 850°C, with the 700°C anneal for 30 seconds being the most effective in reducing the point defects and showing the most optimal dopant diffusion for maintaining high active doping levels. An evidence of reduction in point defects due to annealing was observed, with the maximum PL enhancement increasing from 8× for 6.2×10^{19} cm^{-3} doped unannealed Ge to 12× for 5×10^{19} cm^{-3} doped rapid thermal annealed Ge. However, an in depth study including time-resolved photoluminescence spectroscopy and photoluminescence spectroscopy showed that P doping degrades the crystalline quality of the material, resulting in reduced carrier lifetimes (< 1 ns) and significantly increasing the spectral width of doped Ge. These effects will be investigated in more detail in the next chapter.

References

[1] RW Olesinski, N Kanani, and GJ Abbaschian. *The Ge- P (germanium-phosphorus) system.* Journal of Phase Equilibria, 6(3):262–266, 1985.

[2] Rodolfo E Camacho-Aguilera, Yan Cai, Jonathan T Bessette, Lionel C Kimerling, and Jurgen Michel. *High active carrier concentration in n-type, thin film Ge using delta-doping.* Optical Materials Express, 2(11):1462–1469, 2012.

[3] WM Klesse, G Scappucci, G Capellini, JM Hartmann, and MY Simmons. *Atomic layer doping of strained Ge-on-insulator thin films with high electron densities*. Applied Physics Letters, 102(15):151103, 2013.

[4] Giordano Mattoni, Wolfgang M Klesse, Giovanni Capellini, Michelle Yvonne Simmons, and Giordano Scappucci. *Phosphorus molecules on Ge (001): a playground for controlled n-doping of germanium at high densities*. ACS nano, 7(12):11310–11316, 2013.

[5] Jifeng Liu, Rodolfo Camacho-Aguilera, Jonathan T Bessette, Xiaochen Sun, Xiaoxin Wang, Yan Cai, Lionel C Kimerling, and Jurgen Michel. *Ge-on-Si optoelectronics*. Thin Solid Films, 520(8):3354–3360, 2012.

[6] Yuji Yamamoto, Michael Reiner Barget, Giovanni Capellini, Noriyuki Taoka, Michele Virgilio, Peter Zaumseil, Anne Hesse, Thomas Schroeder, and Bernd Tillack. *Photoluminescence of phosphorous doped Ge on Si (100)*. Materials Science in Semiconductor Processing, 2016.

[7] Yosuke Shimura, Srinivasan Ashwyn Srinivasan, Dries Van Thourhout, Rik Van Deun, Marianna Pantouvaki, Joris Van Campenhout, and Roger Loo. *Enhanced active P doping by using high order Ge precursors leading to intense photoluminescence*. Thin Solid Films, 602:56–59, 2016.

[8] Gang Wang, Frederik E Leys, Laurent Souriau, Roger Loo, Matty Caymax, David P Brunco, Jef Geypen, Hugo Bender, Marc Meuris, Wilfried Vandervorst, et al. *Selective epitaxial growth of germanium on Si wafers with shallow trench isolation: an approach for Ge virtual substrates*. ECS Transactions, 16(10):829–836, 2008.

[9] Dirch H Petersen, Ole Hansen, Rong Lin, and Peter F Nielsen. *Micro-four-point probe Hall effect measurement method*. Journal of Applied Physics, 104(1):013710, 2008.

[10] FJ Morin. *Lattice-scattering mobility in germanium*. Physical Review, 93(1):62, 1954.

[11] Gabriela Dilliway, Ruud Van Den Boom, Alain Moussa, Frederik Leys, Benny Van Daele, Brigitte Parmentier, Trudo Clarysse, Eddy R Simoen, C Defranoux, Marc M Meuris, et al. *In situ phosphorus doping of germanium by APCVD*. ECS Transactions, 3(7):599–609, 2006.

[12] Hyun-Yong Yu, Szu-Lin Cheng, Peter B Griffin, Yoshio Nishi, and Krishna C Saraswat. *Germanium In Situ Doped Epitaxial Growth on Si for High-Performance n+/p-Junction Diode*. IEEE Electron Device Letters, 30(9):1002–1004, 2009.

[13] JM Hartmann, JP Barnes, M Veillerot, JM Fedeli, Q Benoit A La Guillaume, and V Calvo. *Structural, electrical and optical properties of in-situ phosphorous-doped Ge layers*. Journal of Crystal Growth, 347(1):37–44, 2012.

[14] S Noor Mohammad and M Abdus Sobhan. *Doping dependent bandgap narrowing in silicon and germanium*. physica status solidi (b), 156(1):287–302, 1989.

[15] SC Jain and DJ Roulston. *A simple expression for band gap narrowing (BGN) in heavily doped Si, Ge, GaAs and GexSi1- x strained layers*. Solid-State Electronics, 34(5):453–465, 1991.

[16] Rodolfo Camacho-Aguilera, Zhaohong Han, Yan Cai, Lionel C Kimerling, and Jurgen Michel. *Direct band gap narrowing in highly doped Ge*. Applied Physics Letters, 102(15):152106, 2013.

[17] Michael Oehme, Martin Gollhofer, Daniel Widmann, Marc Schmid, Mathias Kaschel, Erich Kasper, and Jörg Schulze. *Direct bandgap narrowing in Ge LEDs on Si substrates*. Optics express, 21(2):2206–2211, 2013.

[18] M El Kurdi, T Kociniewski, T-P Ngo, J Boulmer, D Debarre, P Boucaud, JF Damlencourt, O Kermarrec, and D Bensahel. *Enhanced photoluminescence of heavily n-doped germanium*. Applied Physics Letters, 94(19):191107, 2009.

[19] Xiaochen Sun, Jifeng Liu, Lionel C Kimerling, and Jurgen Michel. *Direct gap photoluminescence of n-type tensile-strained Ge-on-Si*. Applied Physics Letters, 95(1):011911, 2009.

[20] Yuji Yamamoto, Li-Wei Nien, Giovanni Capellini, Michele Virgilio, Ioan Costina, Markus Andreas Schubert, Winfried Seifert, Ashwyn Srinivasan, Roger Loo, Giordano Scappucci, et al. *Photoluminescence of phosphorus atomic layer doped Ge grown on Si*. Semiconductor Science and Technology, 32(10):104005, 2017.

[21] R Geiger, J Frigerio, MJ Süess, D Chrastina, G Isella, R Spolenak, Jérôme Faist, and H Sigg. *Excess carrier lifetimes in Ge layers on Si*. Applied Physics Letters, 104(6):062106, 2014.

[22] R Geiger, T Zabel, E Marin, A Gassenq, J-M Hartmann, J Widiez, J Escalante, K Guilloy, N Pauc, D Rouchon, et al. *Uniaxially stressed germanium with fundamental direct band gap*. arXiv preprint arXiv:1603.03454, 2015.

[23] Zhechao Wang, Bin Tian, Marianna Pantouvaki, Weiming Guo, Philippe Absil, Joris Van Campenhout, Clement Merckling, and Dries Van Thourhout. *Room-temperature InP distributed feedback laser array directly grown on silicon*. Nature Photonics, 9(12):837–842, 2015.

[24] M Prost, M El Kurdi, F Aniel, N Zerounian, S Sauvage, X Checoury, F Bœuf, and P Boucaud. *Analysis of optical gain threshold in n-doped and tensile-strained germanium heterostructure diodes*. Journal of Applied Physics, 118(12):125704, 2015.

[25] Abdelhamid Ghrib, Moustafa El Kurdi, Mathias Prost, Sébastien Sauvage, Xavier Checoury, Grégoire Beaudoin, Marc Chaigneau, Razvigor Ossikovski, Isabelle Sagnes, and Philippe Boucaud. *All-Around SiN Stressor for High and Homogeneous Tensile Strain in Germanium Microdisk Cavities*. Advanced Optical Materials, 3(3):353–358, 2015.

[26] Larry A Coldren, Scott W Corzine, and Milan L Mashanovitch. *Diode lasers and photonic integrated circuits*, volume 218. John Wiley & Sons, 2012.

5

Carrier scattering in P-doped Ge

In Chapter 4, P-doped Ge with an active phosphorus concentration of up to 6.2×10^{19} cm^{-3} was achieved without any annealing step. We also observed that the energy of the direct band gap reduced linearly with active P concentration in the Ge layer. In addition to this, the PL spectra of the doped Ge layers were broadended as compared to those of undoped Ge. The broadening of the PL spectra due to carrier scattering and band gap narrowing originate from many-body effects associated with P dopants. The impact of carrier scattering events can be understood through photoluminescence and absorption spectroscopy. They both provide information about the carrier recombination and generation mechanisms in doped Ge. Studying uniformly doped Ge on Si eases the modeling and is more representative for final device stacks, compared to the non-uniformily doped stacks studied in the previous chapter. Therefore, in this chapter we study uniformly doped Ge layers grown on Si. We begin with a study of the epitaxy of these stacks, and then continue with photoluminescence and time resolved photoluminescence measurements of these stacks. Thereafter, we develop a joint density of states model that takes into account carrier scattering induced linewidth broadening effects. Through transient absorption spectroscopy, we probe the dynamics of photo-excited carriers, both in spectral and temporal domain, to extract the impact of linewidth broadening on the absorption and gain spectra of doped Ge.

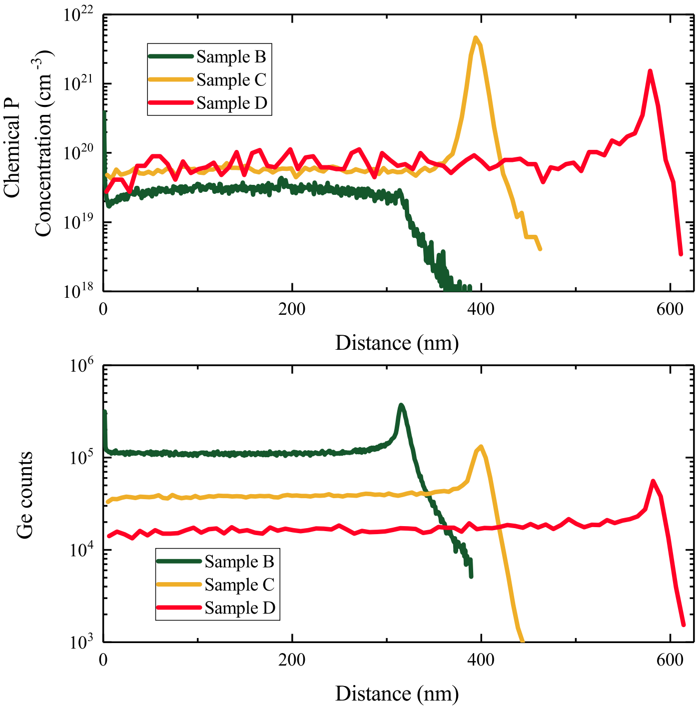

Figure 5.1: Secondary ion mass spectroscopy of 3 uniformly doped Ge layers (Sample B, Sample C and Sample D) grown on Si. The spike in P concentration (top figure) occurs at the interface of Ge and Si.

5.1 Characterization of uniformly doped Ge on Si

The investigated set of samples consists of undoped and doped Ge films epitaxially grown on Si using reduced pressure chemical vapour deposition [1]. Undoped Ge films were grown up to a thickness of 1 μm on a 300 mm Si (001) substrate and thinned down to 0.6 μm using chemical mechanical polishing (CMP). As discussed in previous chapters, this Ge buffer layer is typically biaxially tensile strained by 0.16 $\%$ due to the difference in the thermal expansion coefficients between the epitaxial layer and the Si substrate. This was confirmed by X-ray diffraction. In order to obtain a uniformly doped Ge, the 0.6 μm undoped Ge buffer was further thinned down to 0.2 μm before growing any P-doped Ge layer. Similar to the approach presented in the previous chapter, the doping level in the Ge layer was controlled by modifying the partial pressure ratio of PH_3 and Ge_2H_6. The layers were grown at 320°C or 425°C and were later rapid thermal annealed at 700°C for 30s. The annealing step not only activated the dopants, but also

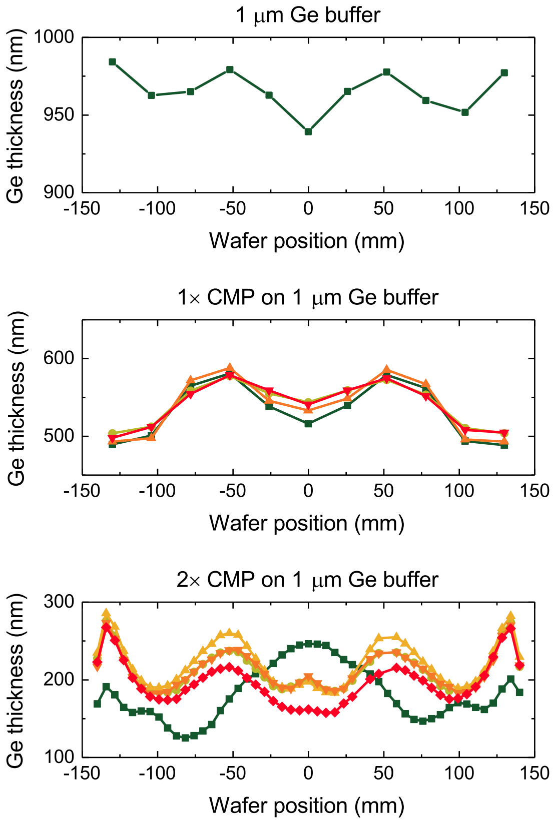

Figure 5.2: Measured Ge thickness for the Ge-layer, as grown (top), with 1× CMP-step (middle) and with 2× CMP-step (bottom).

diffused them into the underlying 0.2 μm of undoped Ge, ultimately resulting in a uniformly doped Ge layer. Using this strategy, 3 samples (Sample B, Sample C and Sample D) with high concentration of P atoms were prepared. They were grown with partial pressure ratio of 0.006 and 0.02, since the studies in Chapter 4 showed that these partial pressures and annealing conditions gave the highest active Phosphorus concentrations and highest PL enhancement. To reach a higher P content in the last sample, a 0.4 μm thick P-doped Ge was grown on the 0.2 μm buffer so that we have a higher reservoir of P dopants atoms before annealing. Out-gassing of dopants during the annealing step in Sample D was suppressed by capping it with SiN, which was etched away after annealing. Using this approach we obtained active doping levels of 2.65×10^{19} cm^{-3}, 4.5×10^{19} cm^{-3} and 5.35×10^{19} cm^{-3} in samples B, C and D respectively. This was verified using secondary ion mass spectroscopy (SIMS) and micro hall effect (MHE) measurements. A 0.6 μm thick undoped Ge layer (Sample A) is used as the reference sample. The SIMS profile of the doped layers is shown in Fig. 5.1 and confirms the uniform distribution of P atoms across the layer. Table 5.1 and Table 5.2 summarize these results. The thickness measured through SIMS and shown in Table 5.2 is different from the targeted thickness. This is related to process variability in the CMP process used to generate 0.2 μm Ge buffer on Si. This thickness variation can be seen in Fig. 5.2. This figures shows the thickness measured for the 1 μm Ge buffer, and the same layer after the first and second CMP step, with each CMP step aimed to remove 0.4 μm of Ge.

Sample Name	Growth Temp	$ppPH_3/ppGe_2H_6$ ratio	Targeted Ge Stack	Anneal with SiN cap
A	N/A	N/A	0.6 μm Buffer	No
B	320°C	0.006	0.2 μm Ge:P on 0.2 μm Buffer	No
C	320°C	0.02	0.2 μm Ge:P on 0.2 μm Buffer	No
D	425°C	0.02	0.4 μm Ge:P on 0.2 μm Buffer	Yes

Table 5.1: Overview of samples studied in this work.

Sample Name	Chemical P Conc. (cm^{-3})	Active P Conc. (cm^{-3})	Measured Ge thickness (μm)
A	N/A	N/A	0.6
B	3.0×10^{19}	2.65×10^{19}	0.32
C	5.6×10^{19}	4.5×10^{19}	0.4
D	7.2×10^{19}	5.35×10^{19}	0.6

Table 5.2: Extracted carrier concentration and thickness of the samples studied in this chapter.

Once the samples were grown, photoluminescence measurements were carried out using the μPL setup with the extended InGaAs detector. As discussed in Chapter 4, this setup allows to measure PL signal over the wavelength range of 1.3-2.0 μm (0.62-0.95 eV). The measurements are performed with a pump intensity of 30 kW/cm^2 using a CW laser source at 532 nm wavelength (2.33 eV). Since the samples in Table 5.2 show a uniform doping profile, we can assume that the photo excited carriers will also be distributed uniformly across the entire Ge thickness. We estimate the photo-excited carrier concentration to be $< 1\times10^{19}$ cm^{-3} by solving the steady state equation [2]. In this equation, the radiative recombina-

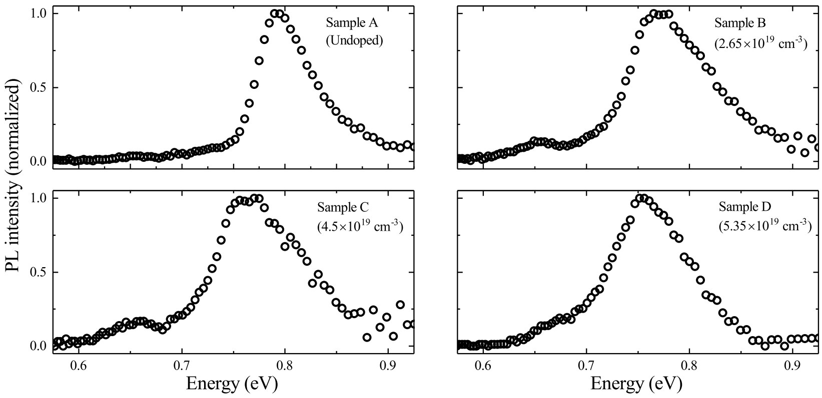

Figure 5.3: Measured photoluminescence spectra for samples listed in Table 5.2. The measurement was performed with a pumping intensity of 30 kW/cm^2 using a CW laser with wavelength of 532 nm (2.33 eV).

tion coefficients ($R^{\Gamma_c\Gamma_v}$) and Auger recombination coefficients (C_n and C_p) were taken from the latest experimentally derived values [3, 4]. A Shockley Read Hall recombination associated carrier lifetime of 3 ns and 0.3 ns was used for undoped and doped Ge respectively. These values are supported by the experimental results that will be presented later. The room temperature PL spectra of undoped and doped Ge layers are shown in Fig. 5.3, whereby the dominant peak corresponds with the Γ_c-Γ_v direct transition between the conduction and valence bands.

When comparing the PL spectra from the 4 samples, there is an evident shift in the PL peak to lower energies for the doped samples. This is due to the dopant induced bandgap narrowing effect that was also observed in the previous chapter [6, 10]. In addition to this, a second emission peak is observed at energy-levels in the range of 0.6 - 0.7 eV, releated to the L_c-Γ_v indirect transition arising due to ionized impurities in the doped samples [11]. Even aside from this second peak, the measured spectra for the doped layers, Sample B to D, were significantly broader than that of the undoped Ge layer, Sample A. This broadening was also observed in the doped Ge layers grown on 1 μm thick virtual substrates as seen in Fig. 4.15 and Fig. 4.16. We believe that the spectral broadening arises due to the dopant dependent carrier scattering that broadens the carrier recombination and carrier generation (absorption of light) spectrum. Fig. 5.4 illustrates this further, where we summarize the P-concentration dependent FWHM of PL and EL spectra measured by different groups working in the field. This shows that the effect is general and not limited to our specific samples.

On a parallel note, time resolved PL (TRPL) was also performed. The PL decay from sample B to D shows the exact same response as that of the pump laser, unlike the decay obtained from sample A, as can be seen in Fig. 5.5. This is because of the extremely low carrier lifetime in the doped films which makes their TRPL response follow the shape of the pump laser. Contrary to what was observed in the previous chapter, a PL decay with two time constants was not observed in the currently studied doped samples due to the absence of any underlying buffer layer. These 3 phenomena - dopant induced band gap narrowing, broadening of the PL spectra associated with the direct bandgap and fast PL decay were also observed in P-doped Ge layers grown on 1 μm Ge buffers presented in the previous chapter. This indicates that the measured phenomena are associated with dopants and occur for all high in-situ doped Ge layers. Therefore, in order to better understand the impact of these carrier scattering events on the achievable gain, we will investigate the linewidth broadening effects in Ge by analyzing the PL spectra and transient absorption spectroscopy in the following section.

5.2 Analysis of carrier scattering

5.2.1 Theoretical and experimental background

The presence of dopants introduces many-body effects in the form of linewidth broadening or homogeneous broadening and band gap narrowing by modifying the absorption and photoluminescence spectra [12, 13]. Typically, a standard Joint Density of States (JDOS) model based on single particle theory is used to describe

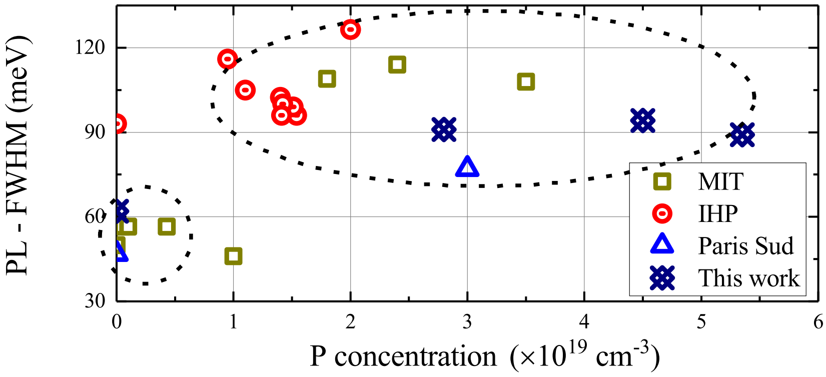

Figure 5.4: Comparison of full width at half maximum (FWHM) vs. P-dopoing level of measured PL spectra. The figure compares samples from MIT [5, 6], IHP [7], Paris Sud [8, 9] and those studied in this chapter as listed in Table 5.1 and Table 5.2.

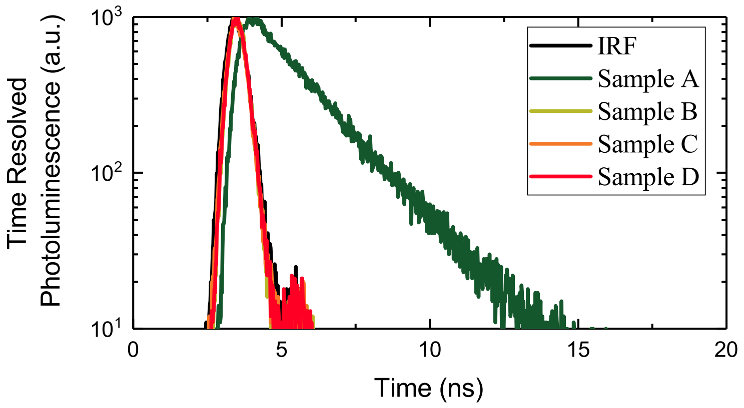

Figure 5.5: Results from time resolved photoluminescence measurements.

the absorption (α) and photoluminescence spectra r^{spon} using Eq. 5.1 and Eq. 5.2 [14]:

$$\begin{aligned} \alpha(\hbar\omega) &\propto \rho_r(\hbar\omega)\big[\mathrm{f_v} - \mathrm{f_c}\big] \\ r^{spon}(\hbar\omega) &\propto \rho_r(\hbar\omega)\big[\mathrm{f_c}\big(1 - \mathrm{f_v}\big)\big] \end{aligned} \tag{5.1}$$

with the reduced (or joint) density of states defined as:

$$\rho_\mathrm{r}(\hbar\omega) = \int \frac{2\mathrm{d}^3\mathrm{k}}{(2\pi)^2}\delta(\mathrm{E_g} + \frac{\hbar^2\mathrm{k}^2}{2\mathrm{m_r^*}} - \hbar\omega) \propto \sqrt{\hbar\omega - \mathrm{E_g}} \tag{5.2}$$

In the above equations, the presence of a quadratic band dispersion and a delta dirac function assumes ideal carrier dynamics in a defect free crystal lattice. Any deviation from this ideality will result in the occurrence of an Urbach tail and many-body effects [15]. The Urbach tail is an exponential tail added to the quadratic absorption spectrum for energy levels close to and below the band gap. It is characterised by a decay width $\mathrm{E_o}$ called the Urbach parameter. On the other hand, linewidth broadening due to scattering effects broadens the absorption and recombination spectra. This effect is modelled by convoluting the ideal spectrum with a lineshape function $\mathrm{L}(\hbar\omega - \mathrm{E})$, typically a Lorentzian function. The standard JDOS model is updated to a modified JDOS model by including the Urbach tail and linewidth broadening effects where the spectra described by Eq. 5.1 and Eq.

5.2 are modified to:

$$
\begin{aligned}
\alpha_{\mathrm{modified}}(\hbar\omega) &\propto \int \rho_{\mathrm{r,urbach}}(\hbar\omega)(\mathrm{f_v}-\mathrm{f_c})\mathrm{L}(\hbar\omega-\mathrm{E})\mathrm{dE} \\
\mathrm{r}^{\mathrm{spon}}_{\mathrm{modified}}(\hbar\omega) &\propto \int \rho_{\mathrm{r,urbach}}(\hbar\omega)\Big[\mathrm{f_v}(1-\mathrm{f_c})\Big]\mathrm{L}(\hbar\omega-\mathrm{E})\mathrm{dE} \qquad (5.3)\\
\text{with}\quad \mathrm{L}(\hbar\omega-\mathrm{E}) &= \frac{1}{\pi}\frac{\Gamma_{\mathrm{opt}}/2}{(\Gamma_{\mathrm{opt}}/2)^2+(\hbar\omega-\mathrm{E})^2}
\end{aligned}
$$

The FWHM (Γ_{opt}) of the lineshape function $L(\hbar\omega - E)$ is called the broadening parameter and is the sum of all contributing scattering channels that exist in parallel, originating from ionized impurities - (II), neutral impurities due to inactive P atoms - (NI), acoustical phonons (AP), optical phonons (OP) and other forms of material defects such as misfit dislocations at the Ge and Si interface or threading dislocation defects that propagate through the bulk of Ge crystal [16, 17].

$$
\Gamma_{\mathrm{opt}} = \Gamma^{\mathrm{II}} + \Gamma^{\mathrm{NI}} + \Gamma^{\mathrm{AP}} + \Gamma^{\mathrm{OP}} + \Gamma^{\mathrm{D}} \qquad (5.4)
$$

Each of these scattering channels can be decomposed into intravalley and intervalley scattering mechanisms but will not be investigated for this thesis. Therefore, only the net scattering effect associated with Γ_{opt} will be considered. The extent of linewidth broadening present in doped Ge can be determined by comparing the measured photoluminescence spectra as seen in Fig. 5.3 with the modified model of Eq. 5.3. In addition to this, pump probe spectroscopy can be performed to study the spectral shape of the change in absorption coefficient under optical pumping. These measurements can be used to validate the conclusions drawn from the photoluminescence spectroscopy.

A schematic of the setup is shown in Fig. 5.6. It comprises of a Mai Tai Ti:S oscillator and a regenerative amplifier (Spitfire ACE from Spectra Physics), generating 100 fs pulses at 1 kHz repetition rate with pulse energy of up to 4 mJ per pulse at 1.46 eV (900 nm wavelength) [13]. The pump signal was operated at extremely low duty cycle, so that heating effects can be ignored. Five percent of this beam was sent through a YAG crystal to generate a broadband probe signal from 0.73 eV to 1.46 eV (850 nm to 1700 nm wavelength), whereas the remaining 95% of the original 800 nm optical beam was coupled into an optical parametric amplifier (OPA) that converts the incident signal to generate femtosecond pump pulses at 0.95 eV (1300 nm wavelength). The intensity of this pump pulse can be varied from 28 mW/cm^2 to 140 mW/cm^2 (28 μJ/cm^2 to 140 μJ/cm^2). This results in pump excited carrier concentration of 3.0×10^{18} to 1.5×10^{19} cm^{-3}. A temporal delay between the pump and the probe pulses of up to 6 ns can be realized and a resolution of 150 fs is reached with the help of a 2 folded delay stage. The sample is optically excited using a femtosecond pump pulse, which generates a high density of photo-excited carriers that decay in time due to radiative and non-radiative

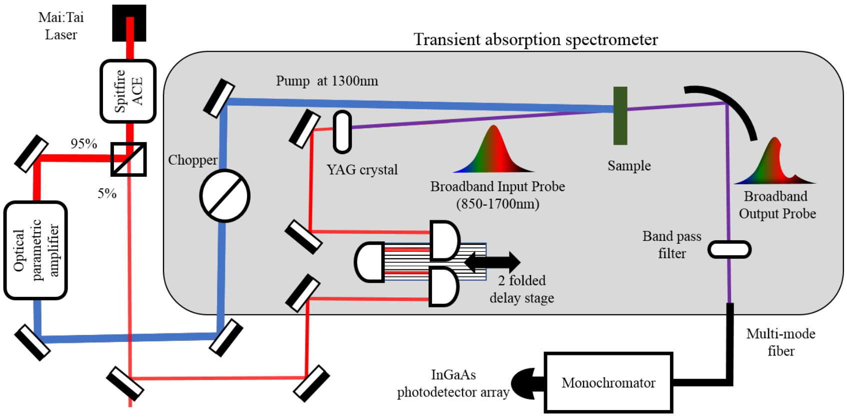

Figure 5.6: Schematic of the transient absorption spectrometer. Femtosecond pump pulses generate carriers in the Ge sample that modify the transmission spectrum of the sample. This change in transmission is monitored by a broadband probe as a function of time with the help of a folded delay stage.

recombination. These photo-excited carriers affect the absorption spectrum of Ge through free-carrier absorption (FCA) and the optical bleaching effect (OBE) and hence affect the spectral shape of the transmitted broadband probe. By monitoring the change in probe power, in the presence and absence of the pump signal, we can track the change in absorption coefficient to understand the carrier dynamics as a function of time and photon energy. This allows us to determine the strength of the linewidth broadening in doped and undoped samples using Eq. 5.3. Since all the samples have Ge films of thickness less than 1 μm on a 760 μm thick Si substrate, the free spectral range of Fabry Perot oscillations related to reflections on the front and back surface of the wafer, is < 0.5 nm, which is below the resolution limit of the measurement setup ($\sim$1 nm). As a result, we ignore free carrier induced dispersion effects of the Ge refractive index that can shift the Fabry Perot oscillation peaks of the transmission spectrum as they will be averaged out in our measurement.

5.2.2 Results and discussion

The room temperature PL spectra of undoped and doped Ge layers were presented in Fig. 5.3 in section 5.1. To estimate the strength of the linewidth broadening, we fitted the measured PL spectra with the standard and modified JDOS model as shown in Fig. 5.7. The measured PL spectra do not match the standard JDOS model, in particular for the doped samples. The modified JDOS model on the other hand fits the measured data-points well. The optimized values extracted from this

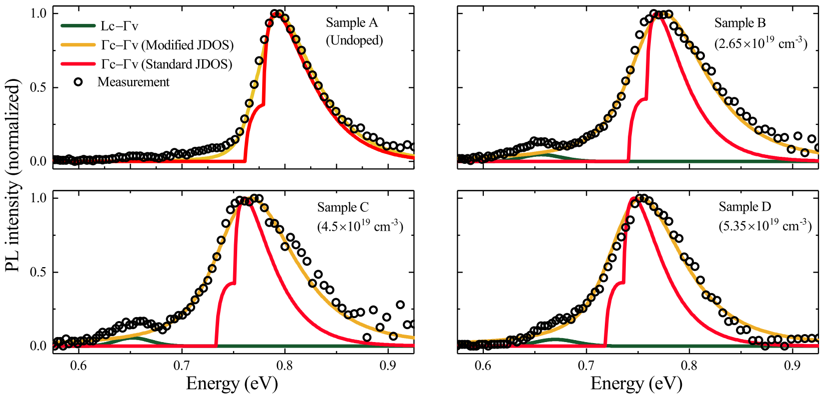

Figure 5.7: The Standard JDOS and the Modified JDOS model were used to analyze the PL spectra originating from $\Gamma_C - \Gamma_V$ *recombination. The small PL peak at lower photon energy (longer wavelength) corresponding to the* $L_C - \Gamma_V$ *indirect radiative recombination process observed in doped Ge is due to Coulomb scattering with charged impurities [11]. These carrier scattering events also broaden the PL spectra that is evident in the P-doped Ge sample. The value of the parameters used in the modified JDOS model are summarized in Table 5.3.*

fit for the broadening parameter Γ_{opt} and the decay width $E_\circ$ of the Urbach tail in the modified JDOS model are listed in Table 5.3. For undoped Ge, we obtain Γ_{opt} = 8 ± 3 meV and $E_\circ$ = 7 ± 1.5 meV. Prior experiments for bulk Ge (undoped) also resulted in Γ_{opt} = 6.4 meV and are consistent with our results [18]. However, for doped Ge, Γ_{opt} increased to 45 meV with the width of the Urbach tail being unaffected. The increase in the linewidth broadening parameter Γ_{opt} is believed to be related to the presence of additional carrier scattering channels originating from the presence of dopant dependent ionized impurity. In addition to the PL measurement, the time dependent and wavelength dependent change in

Sample Name	Chemical P Conc. (cm^{-3})	Active P Conc. (cm^{-3})	Γ_{opt} (meV)	$E_\circ$ (meV)
A	N/A	N/A	8 ± 3	7 ± 1.5
B	2.8×10^{19}	2.65×10^{19}	47.5 ± 2.5	6 ± 1.5
C	5.5×10^{19}	4.5×10^{19}	50 ± 2.5	7 ± 1.5
D	8.3×10^{19}	5.35×10^{19}	45 ± 2.5	5 ± 1.5

Table 5.3: Summary of extracted broadening parameter (Γ_{opt}) *and Urbach tail* ($E_\circ$) *using modified JDOS model.*

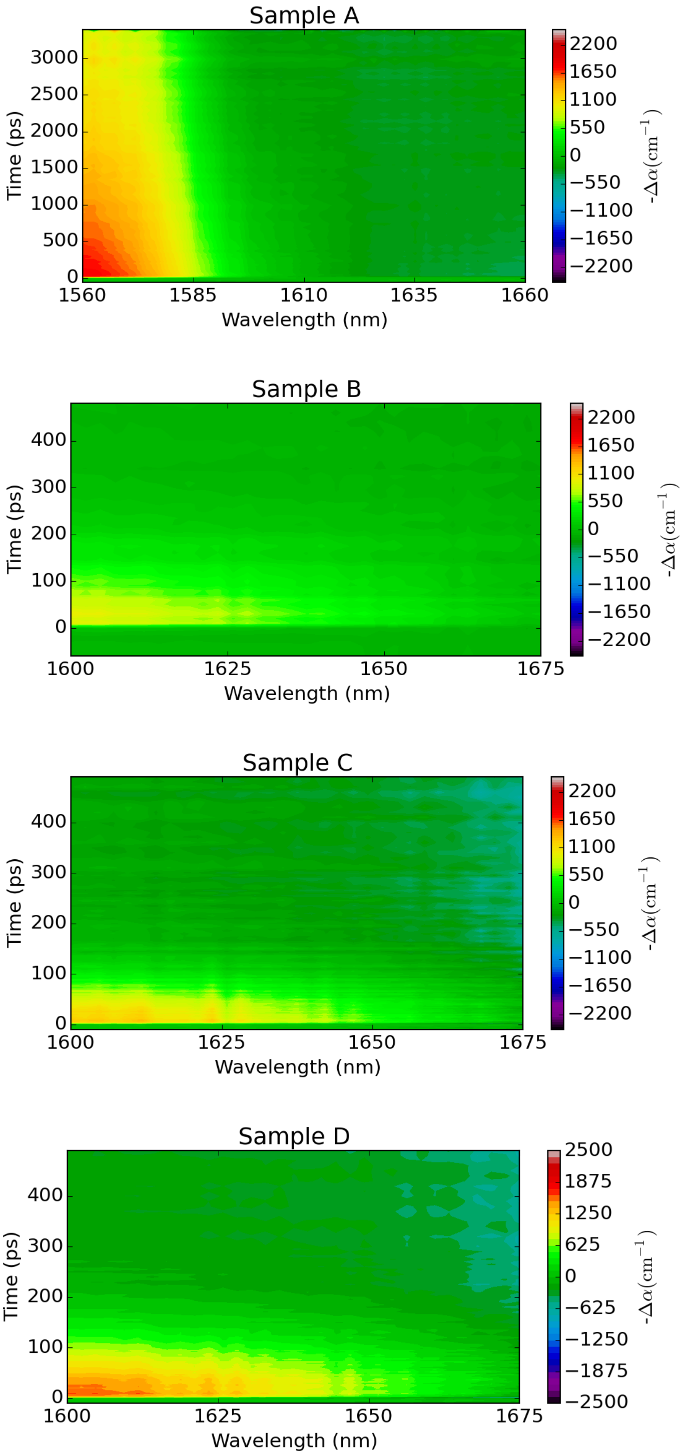

Figure 5.8: Time and wavelength resolved change in absorption coefficient of undoped Ge (Sample A) and doped Ge (Sample B to D) extracted for a pump induced photo-excited carrier concentration of 1.0×10^{19} cm^{-3}. Note that here the y-axis is $-\Delta\alpha$ where $-\Delta\alpha = \alpha(\text{Unumped}) - \alpha(\text{Pumped})$ does not represent gain, it is the change in absorption coefficient (or optical bleaching effect).

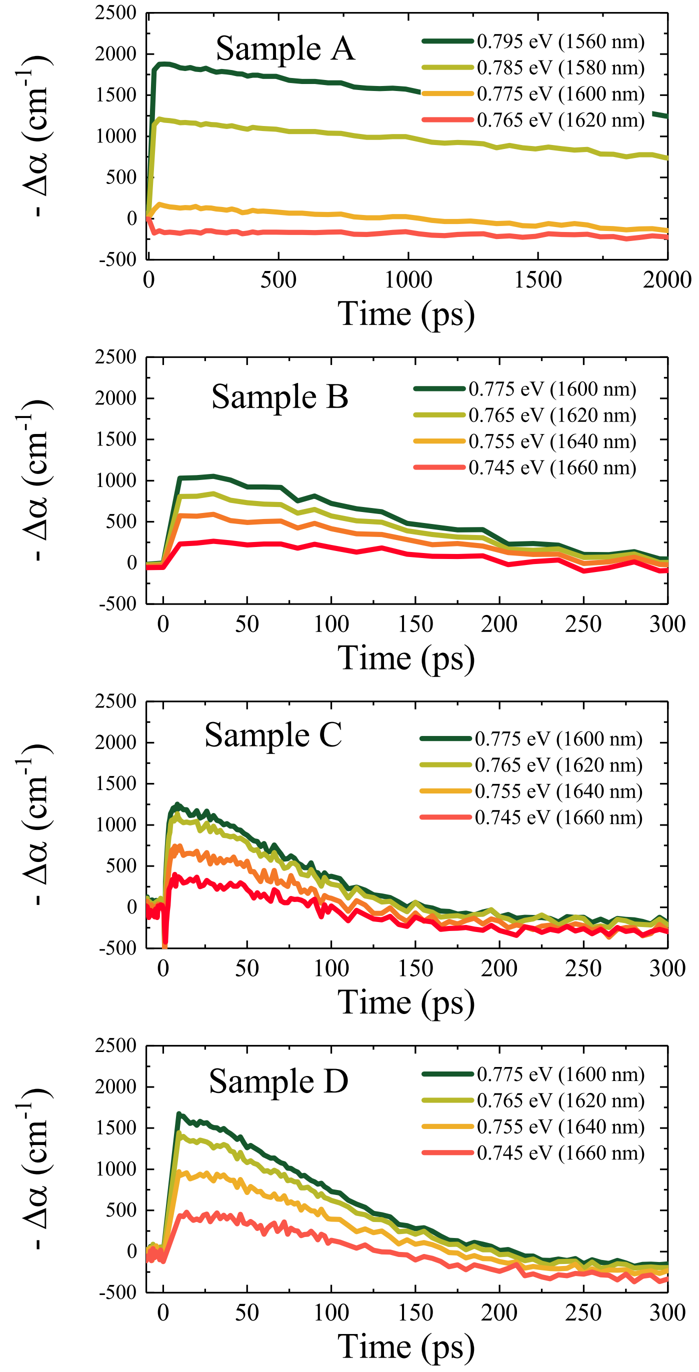

Figure 5.9: Reduction in absorption coefficient of undoped Ge (Sample A) and doped Ge (Sample B to D) as function of time, for a pump induced photo-excited carrier concentration of 1.0$\times$*10*^{19} *cm*$^{-3}$ *at different wavelengths. Note that here the y-axis is* $-\Delta\alpha$ *where* $-\Delta\alpha = \alpha(\mathrm{Unumped}) - \alpha(\mathrm{Pumped})$ *does not represent gain, it is the change in absorption coefficient (or optical bleaching effect).*

absorption extracted from pump-probe spectroscopy is shown in Fig. 5.8. Slices of this figure at different probe wavelengths are shown in Fig. 5.9, where we see the change in absorption due to the optical bleaching effect (OBE) [19, 20]. The typical time for a photo excited carrier to scatter from the Γ valley to the L valley is around 230 fs in bulk Ge. During this 230 fs timeframe, an optical gain of $\geq$ 1300 cm^{-1} was extracted solely related to the occupancy of the Γ valley [21, 22]. However, in practical device operation, electrons are redistributed between the Γ and the L valleys. Therefore, in this work, we focus on the data analysis of the transient absorption spectra taken 1 ps after the incidence of the pump pulse. When comparing the temporal response for doped and undoped Ge films, the carrier lifetime dropped from 3 ns in Sample A to $<$ 0.3 ns for all the doped Ge films. This drop was observed across a wide range of pump intensities. As discussed in Chapter 3, the carrier lifetime in undoped Ge are primarily limited by the defective Ge/Si interface that has a high interface recombination velocity of 1.0×10^4 cm/s [23]. However, the drop in carrier lifetime from undoped Ge to doped Ge is solely related to dopant induced Coulomb scattering or dopant induced point defects [4, 11, 24]. Fig. 5.10 shows the pump power dependent transient absorption spectra. In this figure, all OBE spectra for the doped samples are shifted towards low photon energy (longer wavelength) due to dopant dependent band gap narrowing. In addition, the spectra for doped Ge (Sample B to D) are suppressed and broadened when compared with undoped Ge (Sample A) for the same pump level. The pump intensity in this measurement was varied from 28-140 mW/cm^2, which generates a photo-excited carrier concentration of 3.0×10^{18}-1.5×10^{19} cm^{-3}. Since the majority of the dopant associated electrons occupy the low L_c valley, any excess electrons injected should have higher probability to occupy the Γ_c valley and are expected to be more efficient in bleaching the absorption coefficient. When modeled using the standard JDOS model, the bleaching effect is indeed higher for doped Ge, as shown in the 2^{nd} column of Fig. 5.10. However, these curves do not represent the measured trends where the change in absorption coefficient was suppressed in doped Ge. The modified JDOS model on the other hand, as shown in the 3^{rd} column of Fig. 5.10, matches well with the experimentally obtained trends. To simulate these curves we used the broadening parameter (Γ_{opt}) and the width ($E_\circ$) of the Urbach tail extracted from the PL study summarized in Table 5.3. The good match confirms that the parameters describing the many-body-effects in these doped Ge layers are consistent across the pump-probe based absorption and PL measurements. This suggests that it is essential to include these effects in the models to accurately describe the measured spectra. This analysis was performed across the entire range of investigated photoexcited carrier concentration (3.0×10^{18}-1.5×10^{19} cm^{-3}), across a wide spectral region of 0.74-0.83 eV (1500-1650 nm wavelength). Since the measurement was performed across a wide range of pump intensities, we believe that the photoex-

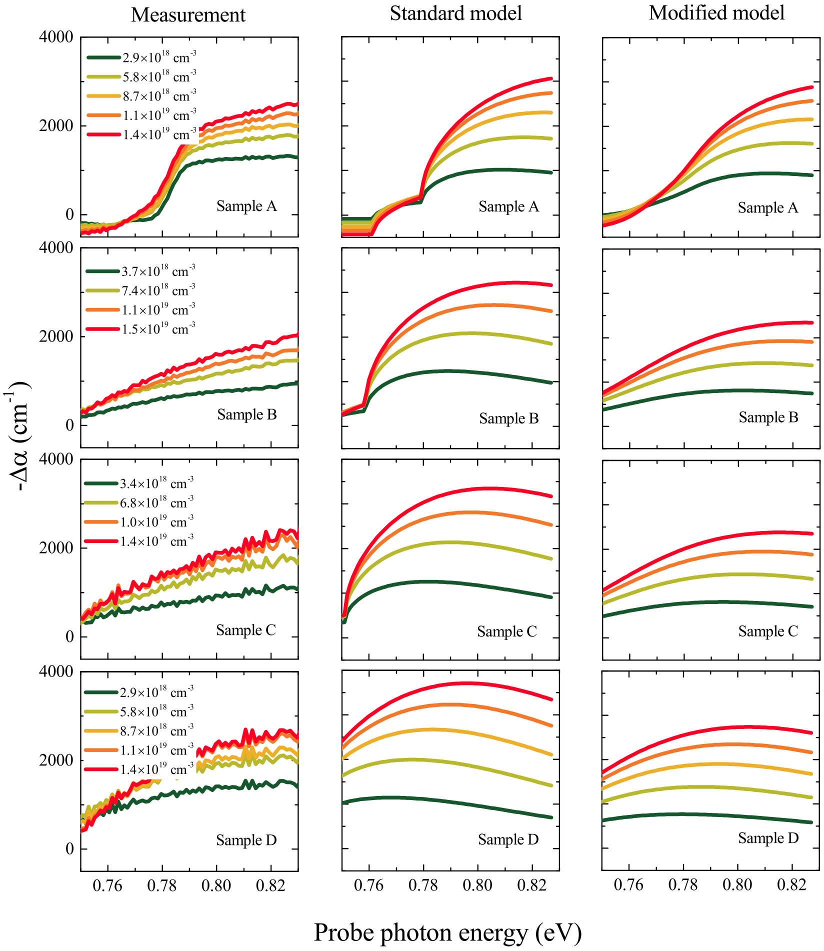

Figure 5.10: Summary of pump-probe spectroscopy for all samples presented in Table 5.2. Note that here the y-axis is $-\Delta\alpha$ where $-\Delta\alpha = \alpha(\text{Unpumped}) - \alpha(\text{Pumped})$ does not represent gain, it is the change in absorption coefficient (or optical bleaching effect). The peak $-\Delta\alpha$ is extracted from Fig. 5.9 across a wide range of pump induced photo-excited carrier concentrations. The standard JDOS model and modified JDOS model were used to model the impact of these photo-excited carriers on the change in absorption coefficient of Ge. A good agreement across all carrier concentrations and photon energies validates the modified JDOS model and supports the presence of carrier scattering events in P-doped Ge, while the standard JDOS model failed to reproduce the experiments. The parameters used for the modified JDOS model are those used for fitting the PL spectra in Fig. 5.7 and are summarized in Table 5.3.

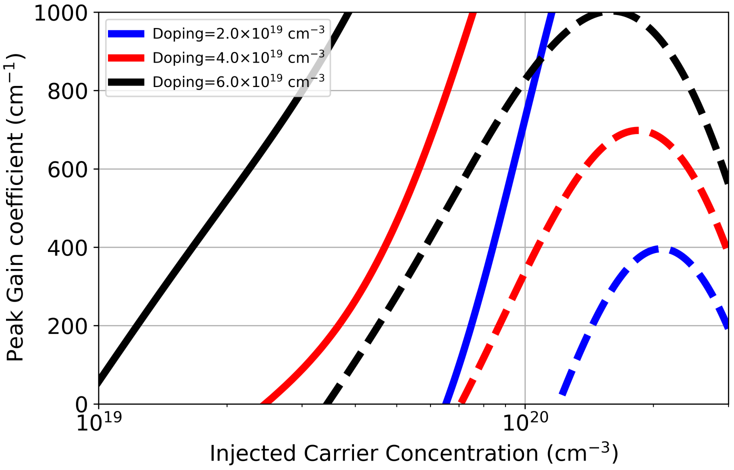

Figure 5.11: Peak optical gain estimated from Ge with varying doping level and injected carrier concentrations. The solid lines represent the results from the standard JDOS model using Eq. 2.10 whereas the dashed lines represent results simulated with the modified JDOS model, taking into account a linewidth broadening parameter Γ_{opt} *= 45 meV, in Eq. 5.3.*

cited carrier concentration does not have a dramatic influence on the broadening of recombination/gain spectra and we therefore attribute the broadening effect to dopant dependent carrier scattering events that results in a broadening parameter $\Gamma_{opt} \geq 45$ meV.

5.3 Impact of carrier scattering on target laser performance

In the previous section, we showed that a broadening parameter of $\Gamma_{opt} \geq 45$ meV, originating from carrier scattering events, significantly suppresses and broadens the absorption and photoluminescence spectra. Clearly, the linewidth broadening phenomena cannot be ignored for modeling the gain and threshold as was earlier presented in section 2.1.2. By replacing Eq. 2.10 with Eq. 5.3, we can take into account the many-body effects. This results in a modification of the gain curves of Fig. 2.7 and threshold current density curves of Fig. 2.8 to those shown in Fig. 5.11 and Fig. 5.12 respectively. The results were restricted to doping levels of $\leq 6\times10^{19}$ cm^{-3} as a maximum doping level of 5.35×10^{19} cm^{-3} was achieved in our work, see Table 5.2. The simulation results from the standard JDOS model underestimate the threshold current density by a factor > 4 due to

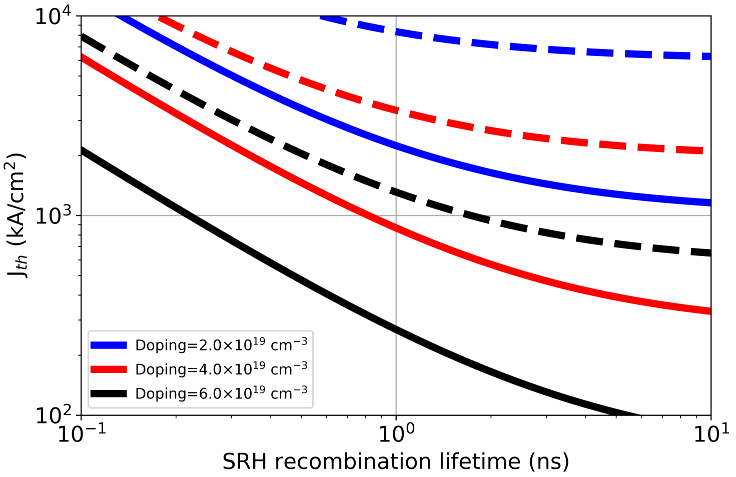

Figure 5.12: Threshold current density estimated for a target modal gain of 200 cm^{-1} using Eq. 2.15 and Fig. 5.11. The solid lines represent the standard JDOS model whereas the dashed line represents results simulated with the modified JDOS model with a linewidth broadening parameter of Γ_{opt} = 45 meV. Carrier scattering associated linewidth broadening effects clearly increases the threshold current density of the target laser by a factor > 4.

the absence of carrier-scattering. In addition to this, we observed that the carrier lifetime dropped to < 0.3 ns in all doped Ge layers from 3 ns in undoped Ge. As a result, if we assume a double heterojunction laser diode using uniformly doped Ge layers with an active doping level of 6×10^{19} cm^{-3} and a carrier lifetime of 0.3 ns as the active medium, then we expect the device to lase at a threshold current density of 3×10^{3} kA/cm^{2} for a target cavity loss of 150 cm^{-1}. The estimated threshold current density is higher by a factor > 40 as compared to the originally targeted laser diode with a carrier lifetime of 3 ns (similar to that of an undoped Ge) and no linewidth broadening effects. As a result of these many-body effects, we now believe achieving an energy-efficient laser using P-doped Ge on Si is beyond reach. In addition, it must be noter that the demonstrated Ge laser using n-type dopants have a threshold current density of 280-500 kA/cm^{2} have doping levels up to 4×10^{19} cm^{-3} [25–27]. Without considering any linewidth broadening events, based on Fig. 5.12, the expected lifetime in the doped Ge layer is in the range of 4-10 ns. These lifetimes are an order of magnitude higher than those measured in this work and presented in the literature [4, 13, 24]. With the inclusion of linewidth broadening effects, the reported threshold current densities do not agree with the work presented in this thesis.

5.4 Summary

In this chapter, we studied the carrier scattering induced linewidth broadening effects in Ge due to P dopants. Results from PL spectroscopy and femtosecond pump probe spectroscopy were analyzed using a modified joint density of states model to identify the presence of linewidth broadening. A significant increase in the full width at half maximum of the PL spectra and suppressed and broadened optical bleaching spectra for doped Ge as compared to undoped Ge were observed. By fitting a modified JDOS model to the results from PL and pump-probe spectroscopy, we extract a broadening parameter $\Gamma_{opt} \geq 45$ meV for doped Ge and $\Gamma_{opt} = 8$ meV for undoped Ge. Such a high broadening parameter reduces the pump/injection efficiency for reaching transparency or gain by a factor ≥ 4. In addition, the carrier lifetime is lowered by more than an order of magnitude, from 3 ns in undoped Ge to < 0.3 ns in P-doped Ge due to the dopant impurities. This observation is not dependent on the pump fluence. Therefore, we believe that even though these P dopants are necessary to make Ge an efficient light emitter by making it a pseudo direct band gap material, they introduce detrimental scattering effects that significantly increase the threshold current density due to reduction in carrier lifetime by a factor ≥ 10 and reduced efficiency in reaching transparency of gain due to linewidth broadening by a factor ≥ 4. This results in a net increase in the estimated threshold current density by a factor > 40, strongly reducing the potential of pseudo-direct P-doped Ge as an optical gain material.

References

[1] Yosuke Shimura, Srinivasan Ashwyn Srinivasan, Dries Van Thourhout, Rik Van Deun, Marianna Pantouvaki, Joris Van Campenhout, and Roger Loo. *Enhanced active P doping by using high order Ge precursors leading to intense photoluminescence*. Thin Solid Films, 602:56–59, 2016.

[2] M Virgilio, CL Manganelli, G Grosso, Thomas Schroeder, and G Capellini. *Photoluminescence, recombination rate, and gain spectra in optically excited n-type and tensile strained germanium layers*. Journal of Applied Physics, 114(24):243102, 2013.

[3] R Geiger, T Zabel, E Marin, A Gassenq, J-M Hartmann, J Widiez, J Escalante, K Guilloy, N Pauc, D Rouchon, et al. *Uniaxially stressed germanium with fundamental direct band gap*. arXiv preprint arXiv:1603.03454, 2015.

[4] R Geiger, J Frigerio, MJ Süess, D Chrastina, G Isella, R Spolenak, Jérôme Faist, and H Sigg. *Excess carrier lifetimes in Ge layers on Si*. Applied Physics Letters, 104(6):062106, 2014.

[5] Xiaochen Sun, Jifeng Liu, Lionel C Kimerling, and Jurgen Michel. *Direct gap photoluminescence of n-type tensile-strained Ge-on-Si*. Applied Physics Letters, 95(1):011911, 2009.

[6] Rodolfo Camacho-Aguilera, Zhaohong Han, Yan Cai, Lionel C Kimerling, and Jurgen Michel. *Direct band gap narrowing in highly doped Ge*. Applied Physics Letters, 102(15):152106, 2013.

[7] Yuji Yamamoto, Michael Reiner Barget, Giovanni Capellini, Noriyuki Taoka, Michele Virgilio, Peter Zaumseil, Anne Hesse, Thomas Schroeder, and Bernd Tillack. *Photoluminescence of phosphorous doped Ge on Si (100)*. Materials Science in Semiconductor Processing, 70:111–116, 2017.

[8] M El Kurdi, H Bertin, E Martincic, M De Kersauson, G Fishman, S Sauvage, A Bosseboeuf, and P Boucaud. *Control of direct band gap emission of bulk germanium by mechanical tensile strain*. Applied Physics Letters, 96(4):041909, 2010.

[9] M De Kersauson, M El Kurdi, S David, X Checoury, G Fishman, S Sauvage, R Jakomin, G Beaudoin, I Sagnes, and P Boucaud. *Optical gain in single tensile-strained germanium photonic wire*. Optics express, 19(19):17925–17934, 2011.

[10] Michael Oehme, Martin Gollhofer, Daniel Widmann, Marc Schmid, Mathias Kaschel, Erich Kasper, and Jörg Schulze. *Direct bandgap narrowing in Ge LEDs on Si substrates*. Optics express, 21(2):2206–2211, 2013.

[11] Michael R Barget, Michele Virgilio, Giovanni Capellini, Yuji Yamamoto, and Thomas Schroeder. *The impact of donors on recombination mechanisms in heavily doped Ge/Si layers*. Journal of Applied Physics, 121(24):245701, 2017.

[12] Larry A Coldren, Scott W Corzine, and Milan L Mashanovitch. *Diode lasers and photonic integrated circuits*, volume 218. John Wiley & Sons, 2012.

[13] S. A. Srinivasan, C. Porret, M. Pantouvaki, Y. Shimura, P. Geiregat, R. Loo, J. Van Campenhout, and D. Van Thourhout. *Reduction of optical bleaching in phosphorus doped Ge layer on Si*. In 2017 IEEE 14th International Conference on Group IV Photonics (GFP), pages 53–54, Aug 2017.

[14] S.L. Chuang. *Physics of Photonic Devices*. Wiley Series in Pure and Applied Optics. John Wiley & Sons, 2009.

[15] Marius Grundmann. *Physics of Semiconductors*, volume 11. Springer, 2010.

[16] Jasprit Singh. *Electronic and optoelectronic properties of semiconductor structures*. Cambridge University Press, 2007.

[17] Michele Virgilio, Diego Sabbagh, Michele Ortolani, Luciana Di Gaspare, Giovanni Capellini, and Monica De Seta. *Physical mechanisms of intersubband-absorption linewidth broadening in s-Ge/SiGe quantum wells*. Physical Review B, 90(15):155420, 2014.

[18] Richard Geiger. *Direct Band Gap Germanium for Si-compatible Lasing*. PhD thesis, 2016.

[19] Xiaochen Sun, Jifeng Liu, Lionel Kimerling, and Jurgen Michel. *Optical bleaching of thin film Ge on Si*. ECS Transactions, 16(10):881–889, 2008.

[20] R Koerner, M Oehme, M Gollhofer, K Kostecki, M Schmid, S Bechler, D Widmann, E Kasper, and J Schulze. *Optical bleaching in electrical pumped n-doped Ge on Si optical devices*. In Silicon-Germanium Technology and Device Meeting (ISTDM), 2014 7th International, pages 121–122. IEEE, 2014.

[21] Xuejun Xu, Xiaoxin Wang, Keisuke Nishida, Koki Takabayashi, Kentarou Sawano, Yasuhiro Shiraki, Haofeng Li, Jifeng Liu, and Takuya Maruizumi. *Ultralarge transient optical gain from tensile-strained, n-doped germanium on silicon by spin-on dopant diffusion*. Applied Physics Express, 8(9):092101, 2015.

[22] Xiaoxin Wang, Lionel C Kimerling, Jurgen Michel, and Jifeng Liu. *Large inherent optical gain from the direct gap transition of Ge thin films*. Applied Physics Letters, 102(13):131116, 2013.

[23] S. A. Srinivasan, M. Pantouvaki, P. Verheyen, G. Lepage, P. Absil, J. Van Campenhout, and D. Van Thourhout. *Extraction of carrier lifetime in Ge waveguides using pump probe spectroscopy*. Applied Physics Letters, 108(21):211101, 2016.

[24] Yuji Yamamoto, Li-Wei Nien, Giovanni Capellini, Michele Virgilio, Ioan Costina, Markus Andreas Schubert, Winfried Seifert, Ashwyn Srinivasan, Roger Loo, Giordano Scappucci, Diego Sabbagh, Anne Hesse, Junichi Murota, Thomas Schroeder, and Bernd Tillack. *Photoluminescence of phosphorus atomic layer doped Ge grown on Si*. Semiconductor Science and Technology, 32(10):104005, 2017.

[25] Jifeng Liu, Xiaochen Sun, Rodolfo Camacho-Aguilera, Lionel C Kimerling, and Jurgen Michel. *Ge-on-Si laser operating at room temperature*. Optics letters, 35(5):679–681, 2010.

[26] Rodolfo E Camacho-Aguilera, Yan Cai, Neil Patel, Jonathan T Bessette, Marco Romagnoli, Lionel C Kimerling, and Jurgen Michel. *An electrically pumped germanium laser*. Optics express, 20(10):11316–11320, 2012.

[27] Roman Koerner, Michael Oehme, Martin Gollhofer, Marc Schmid, Konrad Kostecki, Stefan Bechler, Daniel Widmann, Erich Kasper, and Joerg Schulze. *Electrically pumped lasing from Ge Fabry-Perot resonators on Si*. Optics express, 23(11):14815–14822, 2015.

6

Ge based electro absorption modulator

Electro absorption modulators exploiting the Franz-Keldysh effect (FKE) or the quantum confined stark effect (QCSE) in the epitaxially grown GeSi or Ge material system will be investigated in this chapter. The FKE and QCSE effects are known to be sub-picosecond phenomena, meaning they can be considered for enabling low power consumption and high band width Si based modulators. In an attempt to demonstrate this, Ge based L- band and GeSi based C- band FKE EAMs, followed by Ge based QCSE EAMs operating in the S- band will be studied in this chapter. The results from this chapter will demonstrate the potential of Ge based modulators for short reach optical interconnect applications.

6.1 Franz Keldysh effect electro absorption modulator

6.1.1 Device design and fabrication

The Franz Keldysh effect based electro-absorption modulator exploits the modulation of the absorption coefficient in bulk semiconductor at photon energies near the direct band gap [1]. An electric field is applied using a p-i-n diode operated in reverse bias. This electric field modulates the absorption coefficient by changing the applied bias [2, 3]. This can be better understood from the Eq. 6.1 below [4],

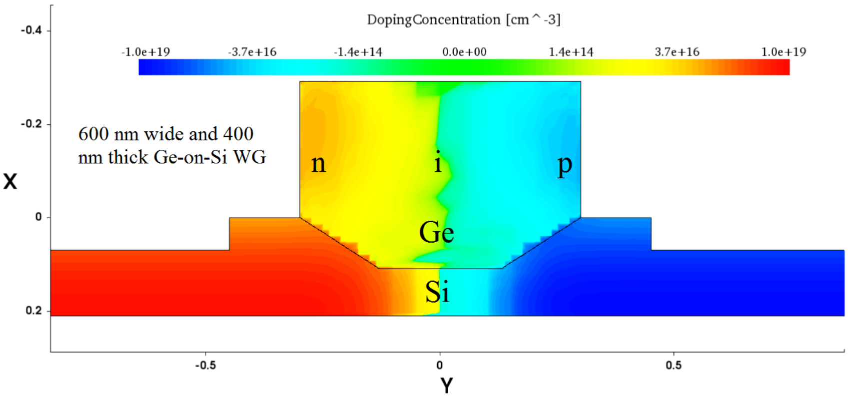

Figure 6.1: Cross-sectional schematic of the Ge EAM device integrated on a 220 nm SOI platform. The doping profile was obtained by simulating the process flow using Sentaurus TCAD process simulator.

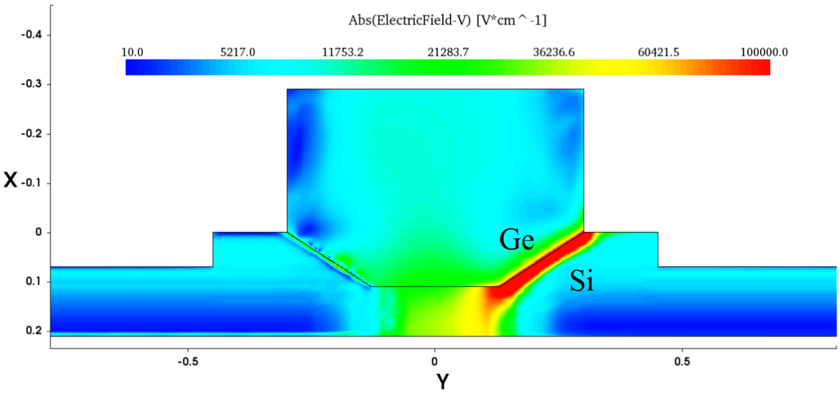

Figure 6.2: Electric field distribution at 0 V simulated using Sentaurus TCAD device simulator.

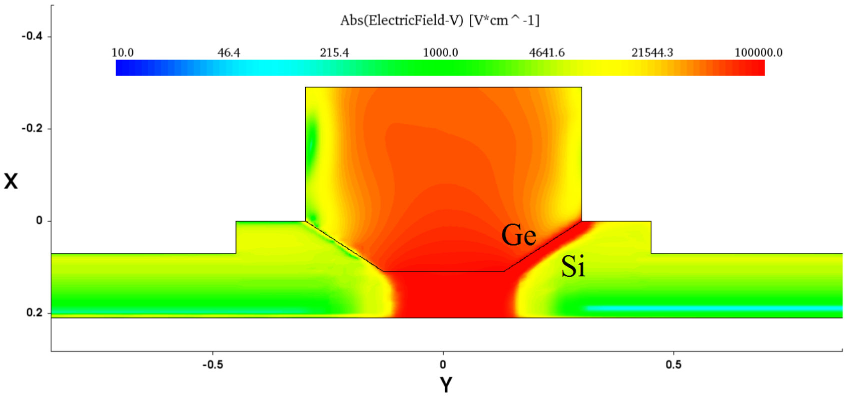

Figure 6.3: Electric field distribution at -2 V simulated using Sentaurus TCAD device simulator.

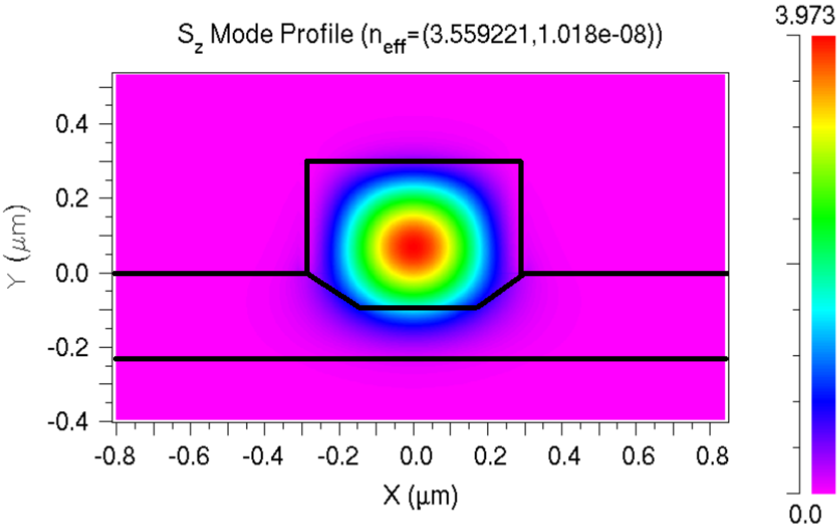

Figure 6.4: Optical mode distribution of the 0.6 μm wide and 0.4 μm thick Ge-on-Si waveguide obtained using the FEM toolkit of RSOFT.

which gives the absorption spectrum as function of the applied field:

$$\alpha_{\mathrm{Direct}}(\hbar\omega) = \frac{\mathrm{A}_{\circ}}{2\pi}\left(\frac{2\mathrm{m}_{\mathrm{r}}^{*}}{\hbar^{2}}\right)^{3/2}\sqrt{\hbar\theta_{\mathrm{F}}}\Big(-\eta\mathrm{Ai}^{2}(\eta)+\mathrm{Ai}'^{2}(\eta)\Big)$$
$$\text{with}\quad \hbar\theta_{\mathrm{F}} = \left(\frac{\hbar^{2}\mathrm{e}^{2}\mathrm{F}^{2}}{2\mathrm{m}_{\mathrm{r}}^{*}}\right)^{1/3} \quad \text{and} \quad \eta = \frac{\mathrm{E_g}-\hbar\omega}{\hbar\theta_{\mathrm{F}}} \tag{6.1}$$

where, the electric field is denoted by F with Ai and Ai′ representing the Airy function and its derivative. A cross-sectional schematic of a 0.6 μm wide and 0.4 μm thick Ge-on-Si waveguide is shown in Fig. 6.1. This WG comprises a lateral p-i-n diode and is biased through the contacts at the highly doped Si region. The doping level in the Ge waveguide is in the order of 10^{17}-10^{18} cm^{-3} such that the EAM has an electric field of 9.8 kV/cm at 0 V and 56 kV/cm at -2V along the width of the Ge waveguide at half its height as seen in Fig. 6.2 and Fig. 6.3. By performing extensive simulations in the Sentaurus TCAD environment, the doping profile was optimised to enable a strong optical mode overlap with the electric field and sufficiently low free-carrier absorption due to dopants. The distribution of the optical mode at 1550 nm wavelength of the 0.6 μm wide and 0.4 μm thick Ge-on-Si waveguide is shown in Fig. 6.4. By combining the simulated electric field distribution in the waveguide, the optical mode distribution, the doping profile and the field dependent Ge absorption through Eq. 6.1, the absorption in the Ge waveguide can be accurately modeled. To demonstrate this, Ge and Ge$_{0.992}$Si$_{0.008}$ will be considered as the active medium. The ~0.8% Si pushes the band gap (associated with the heavy hole valence band) of Ge from 0.785 eV (1580 nm) to 0.808

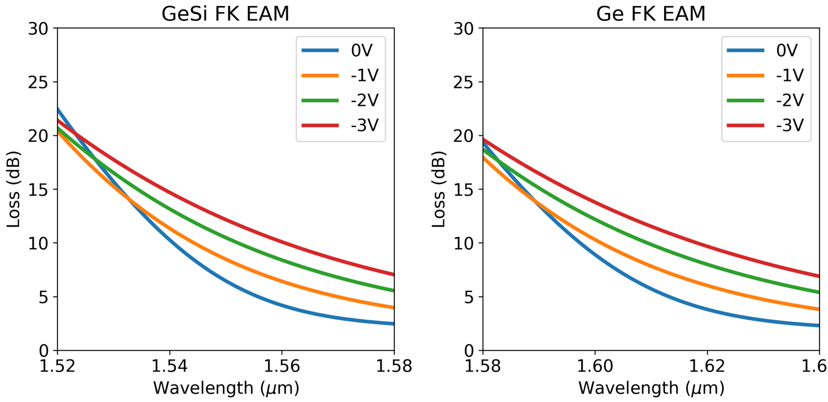

Figure 6.5: Simulated insertion loss spectrum of a 0.6 μm wide and 40 μm long Ge waveguide near the band edge at 0 V, -1 V, -2 V and -3 V, at room temperature.

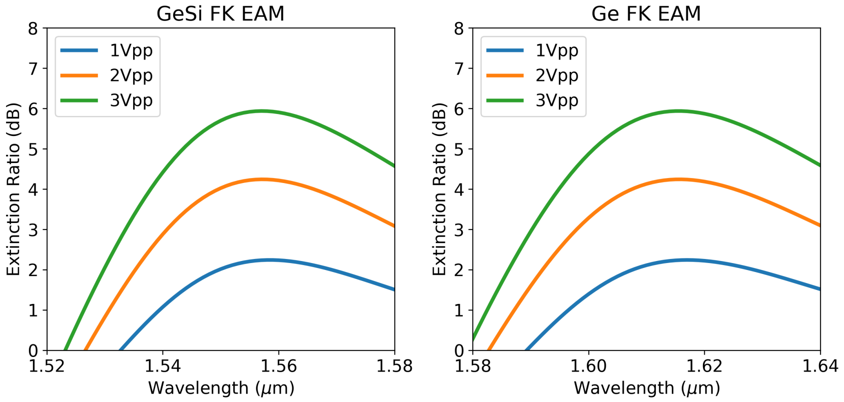

Figure 6.6: Estimated extinction ratio spectrum through a 0.6 μm wide and 40 μm long Ge waveguide near the band edge for a voltage swing of 0 V to -1 V (1 Vpp), 0 V to -2 V (2 Vpp) and 0 V to -3 V (3 Vpp), at room temperature.

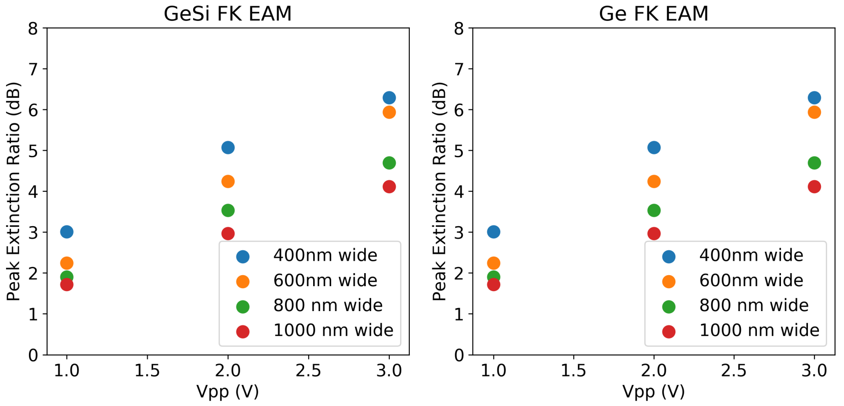

Figure 6.7: Estimated peak extinction ratio from the spectrum shown in Fig. 6.6 as a function of Voltage swing for 40 μm long Ge WG and width varying from 0.4 μm to 1.0 μm.

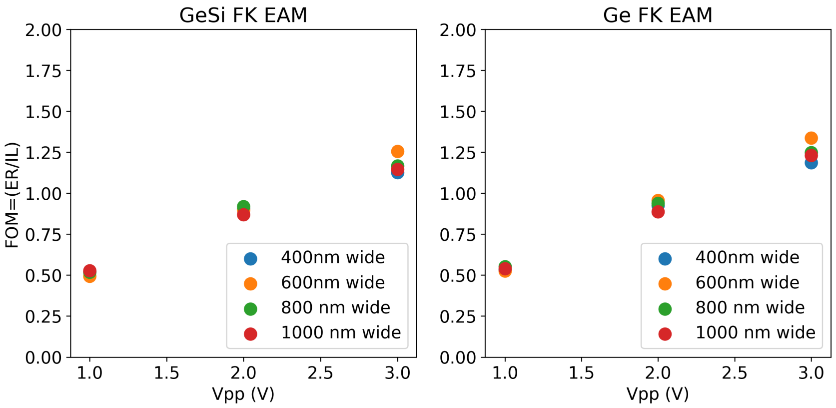

Figure 6.8: Figure of merit (FOM = peak ER/IL) for a 40 μm long Ge WG with a width of 0.4 μm to 1.0 μm for voltage swings of 1 Vpp, 2Vpp and 3 Vpp. When comparing WGs with different widths, 600 μm showed slightly higher FOM . This is due to the compromise between E-field contrast for a fixed voltage swing and the built-in E-field in a given WG where 0.6 μm provides the highest FOM.

eV (1535 nm). As a result of this, Ge will allow modulation of light at wavelength $>$ 1580 nm (L- band) , whereas, GeSi will modulate light at wavelength $>$ 1550 nm (C- band). This can be seen in Fig. 6.5 that shows the simulation result of light absorbed through a 40 μm long Ge or GeSi WG with a p-i-n diode. The simulated result also includes absorption from the indirect band gap using Macfarlane's equations [5, 6]. The doping profile and optical mode in the WG is shown in Fig. 6.1 to Fig. 6.4. The applied reverse bias clearly modulates the insertion loss (IL) of the WG. From Fig. 6.5, the extinction ratio (ER) in dB at a given voltage (V) of the modulator can be extracted using the formula: $\mathrm{ER(V)} = \mathrm{IL(V)} - \mathrm{IL(0)}$, where IL is in dB. The ER for a voltage swing of 0 V to -1 V (1 Vpp), 0 V to -2 V (2 Vpp) and 0 V to -3 V (3 Vpp) are plotted in Fig. 6.6. Due to the presence of the band gap at 0.785 eV and 0.808 eV in Ge and GeSi, maximum modulation can be achieved at 1615 nm (L- band) and 1550 nm (C- band) respectively where we can expect an ER of 4 dB for 2 Vpp voltage swing in a 40 μm long waveguide. As the applied electric field (or reverse bias voltage) increases, the peak ER also increases as seen in Fig. 6.7. The simulation was performed on a wide range of Ge WG widths and a clear dependence of the peak ER is visible. This can be related to the presence of a high electric field difference for narrow Ge WGs with narrow intrinsic region widths. A useful figure of merit (FOM) for such a modulator is the ratio ER/IL, where for large FOMs, the modulator must introduce high loss for the OFF state and low loss for the ON state. On comparing the FOMs from the simulation in Fig. 6.8, the voltage swing from 0 to -3 V (3 Vpp) provides the highest FOM due to the high ER introduced at high E-fields. In addition, 600 μm showed slightly higher FOM when compared to all widths. This is because for a 0.4 μm wide WG, even though the E-field contrast is high as can be seen with the ER, the built-in E-field is also high, due to the thinner depletion region, resulting in high insertion loss and hence low FOM. On the other hand, a 1.0 μm wide WG has the least E-field difference among all WG widths considered but will also have the lowest built-in E-field and hence lowest insertion loss and comparable FOM. As a result of this compromise between E-field difference for a fixed voltage swing and the built-in E-field, 0.6 μm wide WG provides the optimum and highest FOM. A FOM of $\sim$1 and $\sim$1.3 is estimated for voltage swings of 2 Vpp and 3 Vpp. These values are comparable or slightly improved compared to those discussed in Table 2.3.

To experimentally demonstrate this, a set of modulators with Ge length varying in the range of 10-80 μm and width varying in the range of 0.4-1.0 μm were fabricated using imec's iSiPP25G Si photonics platform, which is running on a 130 nm CMOS toolset [7]. The process flow to fabricate these devices is the same as that presented in Section 3.1 with the addition of a dopant implant for the Ge WG. A lateral p-i-n diode with moderate doping concentrations ($\sim 5\times10^{17}$ cm^{-3}) was implemented in the Ge WG with both the anode and cathode contacted from the highly doped Si layers ($>1\times10^{19}$ cm^{-3}), avoiding the need for metal contacts directly on Ge that would introduce excessive IL. These WGs are coupled to a Si WG using low-loss tapers implemented in the poly-Si layer of the iSiPP25G technology. Grating couplers for transverse electric (TE) polarization with peak-coupling wavelength of 1610 nm were used for fiber coupling to and from the chip.

6.1.2 Modulator performance: Static characteristics

Fig. 6.9 shows the I-V characteristics of fabricated 0.6×40 μm^2 Ge and GeSi EAM. The low dark current measured for the Ge (or GeSi) on Si diodes ($\sim$10 nA at -1V for a 40 μm long device) proves the high epitaxy quality of Ge and controlled electrostatics. The low dark current ensures very low static energy consumption in the modulator during IDLE mode. The optical loss or insertion loss introduced by the Ge WG at different reverse bias was measured using transmission measurements and normalizing it with the transmission spectrum of neighbouring reference Si WGs. Fig. 6.10 shows the measured IL spectrum at room temperature. The extracted IL also includes the coupling loss from the poly-Si taper between the Si WG and Ge WG. These measured absorption spectra are similar to theoretical predictions from FKE theory and the simulations shown in Fig. 6.5. From the measured IL spectrum, an ER of 4.3 dB at 1615 nm for the Ge FKE

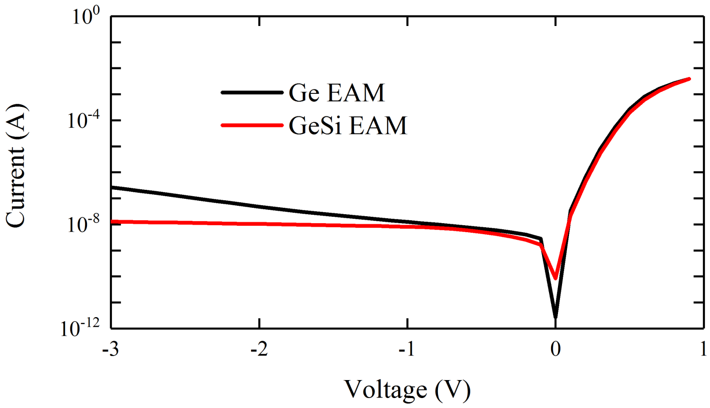

Figure 6.9: Measured I-V characteristics of the fabricated 0.6×40 µm² Ge and GeSi EAM.

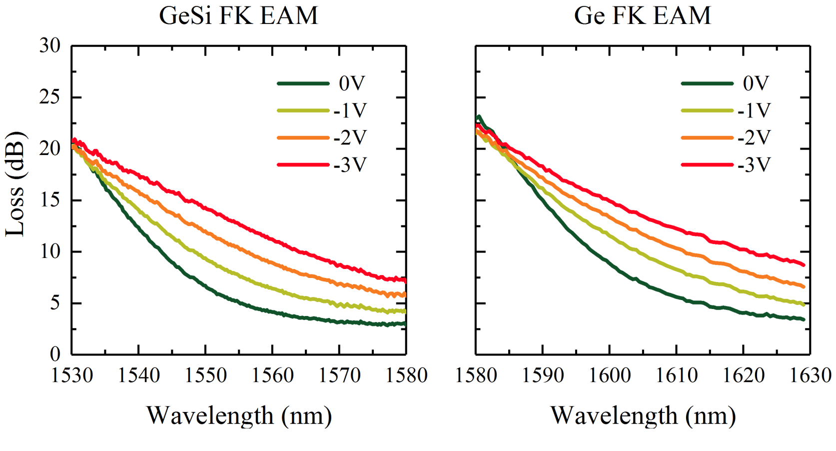

Figure 6.10: Measured Insertion Loss (IL) spectra for a 0.6 µm wide and 40 µm long Ge and GeSi EAM at 0V, -1V, -2V and -3V at room temperature.

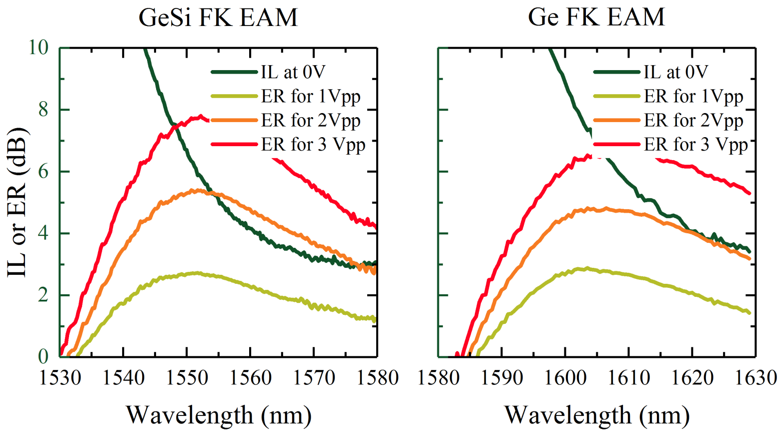

Figure 6.11: Measured extinction ratio (ER) spectra assuming 1 Vpp, 2 Vpp and 3 Vpp for a 0.6 µm wide and 40 µm long Ge and GeSi EAM at room temperature.

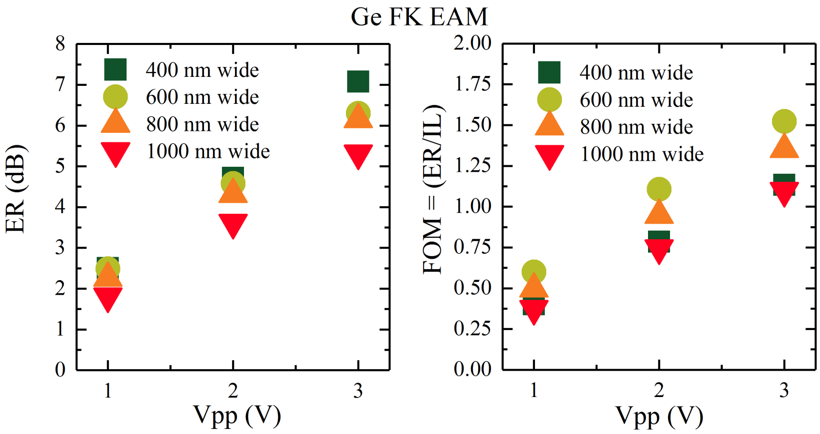

Figure 6.12: Measured peak ER and figure of merit (FOM=ER/IL) from the spectra shown in Fig. 6.11 measured through a set of Ge WGs with width ranging from 0.4 µm to 1.0 µm. The result is similar to the simulated model in Fig. 6.7 and Fig. 6.8.

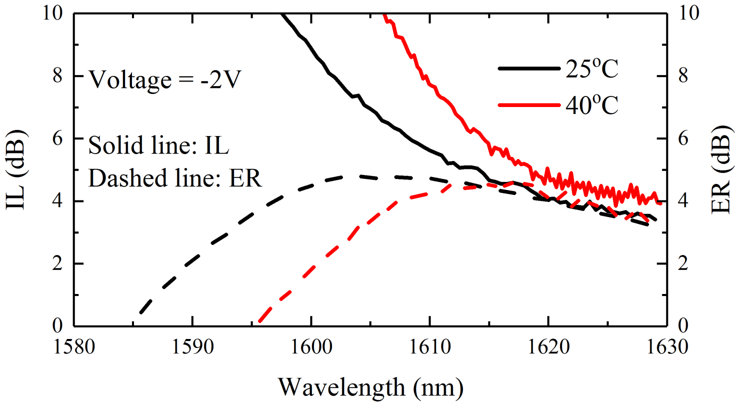

Figure 6.13: IL spectrum at 0 V and extracted ER for 2 Vpp measured at 25° C and 40° C.

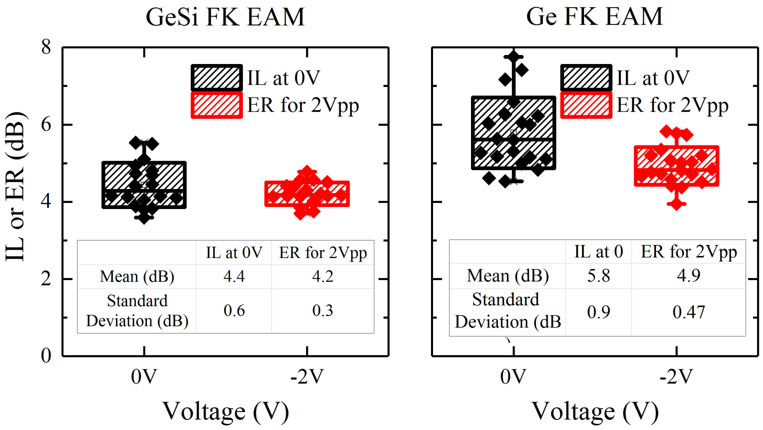

	IL at 0V	ER for 2Vpp
Mean (dB)	4.4	4.2
Standard Deviation (dB)	0.6	0.3

	IL at 0	ER for 2Vpp
Mean (dB)	5.8	4.9
Standard Deviation (dB	0.9	0.47

Figure 6.14: IL and ER at 1550 nm for the GeSi EAM and at 1615 nm for the Ge EAM extracted across 20 dies on a 200 mm SOI wafer. The box edge represents the standard deviation of the measured data.

EAM and 4.65 dB at 1550 nm for the GeSi FKE EAM was extracted as can be seen in Fig. 6.11. The dependence of ER with the voltage swing is shown in Fig. 6.12. These ER and IL spectra are sensitive to the measured temperature as they shift to longer wavelength with the increase in temperature due to band gap narrowing effects. The rate at which the spectra shift is 0.78 nm/°C and is consistent with the Varshni relation for Ge based material systems [8]. The average IL and ER extracted from 20 dies in a 200 mm wafer is shown in Fig. 6.14. An average IL of 5.8±0.9 dB and 4.4±0.6 dB and an average ER of 4.9±0.5 dB and 4.2±0.3 dB were measured for the Ge and GeSi devices respectively. The low standard deviation in the measured ER illustrates the wafer-scale manufacturability of the device.

The impact of having the device in an optical link is quantified through the optical link power penalty (LPP) that the modulator introduces in order to maintain a constant average optical power at the output of the device as compared to the input of the device. This is typically evaluated using Eq. 6.2 [1].

$$\mathrm{LPP(dB)} = -10\log_{10}\Big(\frac{\mathrm{P_{out}(1) - P_{out}(0)}}{2 \times \mathrm{P_{in}}}\Big) \tag{6.2}$$

In this equation, $\mathrm{P_{out}}(1)$ and $\mathrm{P_{out}}(0)$ are the high and low level of output optical power from the modulator and $\mathrm{P_{in}}$ is the input optical power The LPP of a modulator is also used to quantify the operational optical bandwidth of the modulator. A minimum LPP of 8.5 dB at around 1565-1570 nm for the GeSi EAM and 9.1 dB at around 1615-1620 nm for the Ge EAM were extracted for 2 Vpp with a 1dB optical bandwidth of up to 35 nm as can be seen in Fig. 6.15. The LPP reduces with the increase in voltage swing due to the higher ER, however the complexity to design electronic circuits capable of delivering large voltage swing increases and therefore restricts the typical voltage swings up to 2 Vpp. Nevertheless, 30 nm large operational optical bandwidth shows the advantage Ge based EAMs have as compared to silicon ring modulators.

Since the physical mechanism behind the modulation is based on the electro absorption effect, the operation of the device results in the generation of electrons and holes that are extracted from the intrinsic region in the form of photocurrent due to the built-in E-field or applied bias. Fig. 6.16 shows the I-V characteristics of the device with and without illumination. At -1 V and -2 V, the Ge EAM has a dark current of 12.5 nA and 47 nA respectively. Once the laser at 1615 nm was switched on, the light current measured was $\sim$0.5 mA with a responsivity of ~ 1 A/W. The responsivity was extracted by sweeping the input optical power in the waveguide and monitoring the photocurrent. A similar response was measured for the GeSi EAM where a responsivity of $\sim$0.9 A/W was extracted at 1560 nm. This high responsivity adds to the static power consumption of the modulator and will be considered in Section 6.1.4.

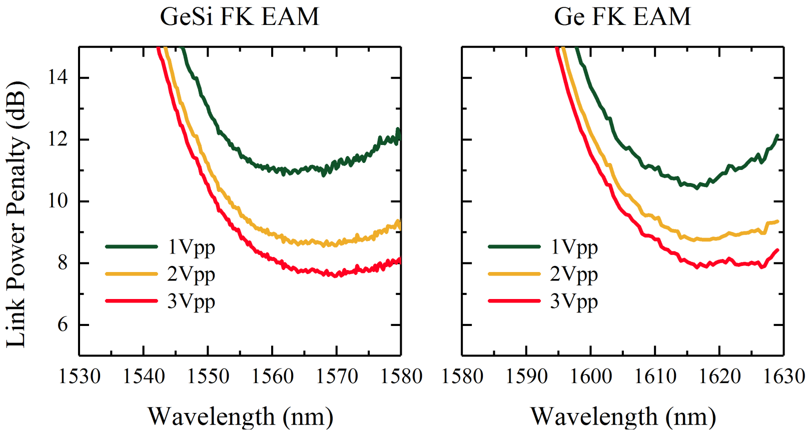

Figure 6.15: Link power penalty for 1 Vpp, 2Vpp and 3 Vpp extracted from Fig. 6.11 and using Eq. 6.2.

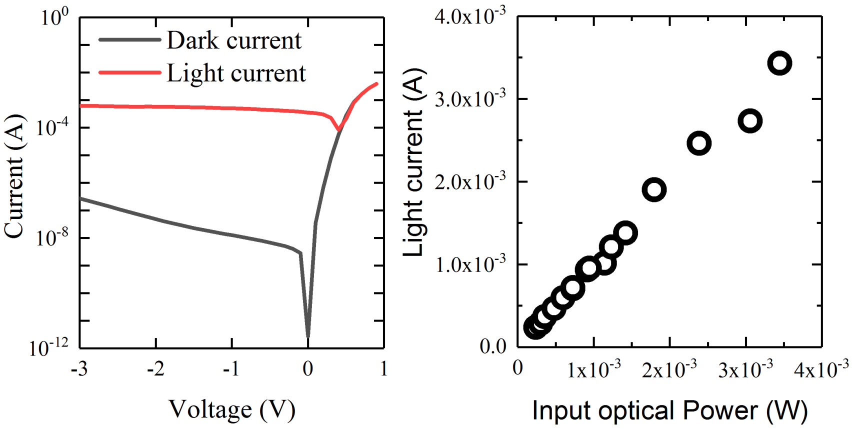

Figure 6.16: Measured photocurrent and dark IV for a 0.6×40 μm Ge EAM. The photocurrent was measured at 1615 nm with an input optical power of -3 dBm (or 0.5 mW) just before the device in Si WG. A responsivity of ∼1 A/W at 1615 nm was extracted.

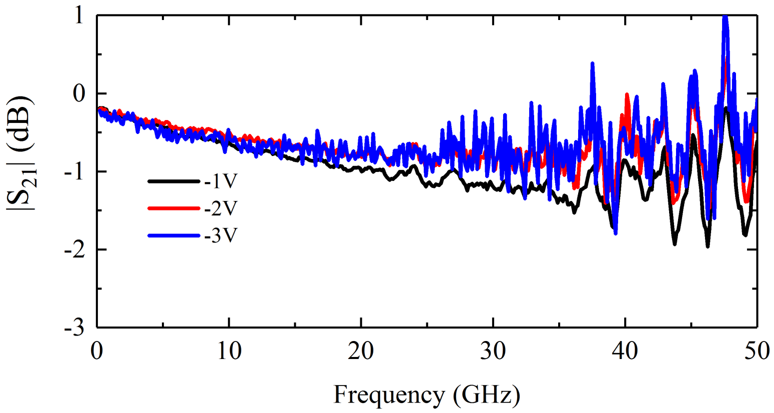

Figure 6.17: S_{21} measurements of Ge EAM with a bandwidth >50 GHz at -1 V, -2 V and -3 V and input power power of 5 dBm.

6.1.3 Modulator performance: High speed characteristics

The high speed performance of the Ge based FKE EAM was characterized by performing small signal S-parameter analysis and large signal modulation to obtain the eye diagram of modulated light transmitted through the waveguide. The measurements were restricted to a 0.6 μm wide and 40 μm long Ge EAM. The bandwidth of the modulator was measured using a 50 GHz lightwave component analyzer where the system was calibrated to normalize the measurement with the response of the probe, cables, bias-tree and the photodetector present in the equipment. Fig. 6.17 shows the typical S_{21} parameter at operating bias of -1 V, -2 V and -3 V measured on a 0.6×40 μm^2 long Ge EAM. A *Keithley* source was used to provide the bias voltage. The 3 dB bandwidth of the modulator is $>$ 50 GHz for operating biases of -1 V to -3 V where the speed of the modulator is typically limited by the RC delay of the device since the FK effect is a phenomenon occurring on a sub picosecond time scale [9]. The same behaviour was observed for both the Ge and GeSi EAM as the RF response is limited by the diode characteristics and not by the material properties. By numerically fitting the experimentally obtained reflectance coefficient of small-signal S-parameter (S_{11}) with an equivalent circuit model, the RC response of the diode can be determined. Fig. 6.18 and Fig. 6.19 shows the measured response and the equivalent circuit model used to fit it. In the equivalent circuit model, R_s and C_j represent the p-i-n diode associated series resistance and junction capacitance. R_{Si} and C_{ox} represent the current path through the bulk Si substrate and the buried oxide respectively. The capacitance due to the metal contact pads is also considered by introducing C_m in parallel to the diode.

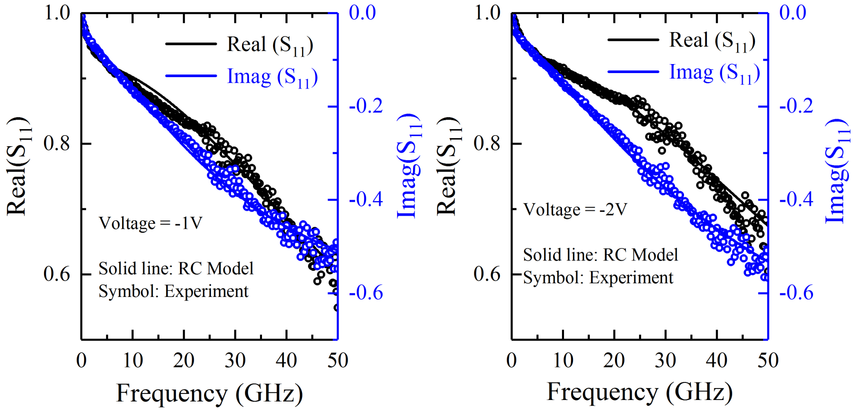

Figure 6.18: S_{11} measurements of Ge EAM at -1 V and at -2 V. Symbols represent the measurement data and solid lines represent the fitting using an equivalent circuit model.

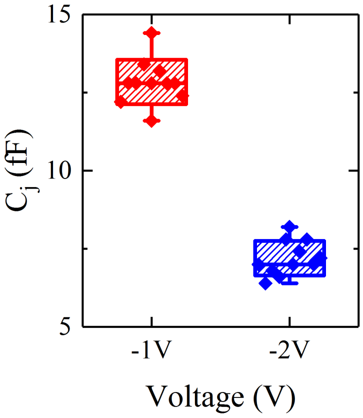

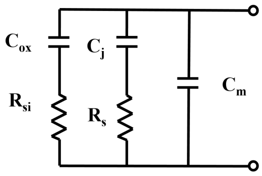

	C_j (fF)	R_s (Ω)	C_{ox} (fF)	R_{si} (Ω)	C_m (fF)
-1V	**12.8**	**139**	**82**	**1248**	**13**
-2V	**7.2**	**280**	**61**	**1398**	**16.7**

Figure 6.19: Small signal equivalent circuit model of the modulator with extracted resistance and capacitance at -1 V and -2 V. The fitting of the model with the S_{11} measurement at -1 V and -2 V is shown in Fig. 6.18.

The impedance of the device ($\mathrm{Z_{EAM}}$) is included in the equivalent circuit model that is used to fit $\mathrm{S_{11}}$ using Eq. 6.3 below:

$$\mathrm{S_{11}} = \frac{\mathrm{Z_{EAM}} - 50\Omega}{\mathrm{Z_{EAM}} + 50\Omega} \tag{6.3}$$

In the above equation, 50 Ω is the characteristics impedance of the RF probe. The junction capacitance of the modulator is estimated to have a wafer mean of 12.8 fF and 7.2 fF along with a series resistance of 138 Ω and 280 Ω at operating bias of -1 V and -2 V respectively. At higher reverse bias, the width of the depletion region in the p-i-n diode should increase resulting in a decrease in junction capacitance and increase in speed. The reduction in junction capacitance with increase in reverse bias is consistent with the extracted values shown in Fig. 6.19, thus adding confidence to the fitting. Using the above estimated R and C values, the RC limited bandwidth of the device is estimated to be beyond 80 GHz. This explains the measured 1 dB bandwidth of ~50 GHz from the EAM as can be seen in Fig. 6.17. Moreover, the fF-range capacitance will result in ultra low power consumption. This makes these modulators promising candidates for optical interconnect applications when compared to MZI based Si modulators. This will be studied further in Sec 6.1.4.

Large signal modulation of the modulator is shown in Fig. 6.20 and Fig. 6.21 for the Ge and GeSi FKE EAM respectively. A pseudorandom binary sequence (PRBS) signal with a pattern length of 2^{31}-1 and data rates of 28, 40, 50 and 56 Gb/s were generated using four 14 Gb/s MU181020B Anritsu pulse pattern generators, a MP1821A 50G/56 Gb/s MUX and were delivered to the device using a GS RF probe from Cascade Microtech. The modulated light from the device was amplified using a C- and L- band EDFA and filtered using an optical tunable filter with wavelength tunability of 1530-1610 nm, before reaching the oscilloscope. The measurements were performed with a nominal peak-to-peak voltage swing of 1.5, 2.0 and 2.5 Vpp to modulate light at 1560nm and 1610nm for GeSi and Ge FKE EAM respectively. For the Ge EAM, the EDFA and the tunable filter limit the operating wavelength to 1610 nm, which is 5-10 nm below the optimum wavelength with the lowest LPP. Clear and open eye diagrams with dynamic ER of 3.29 dB and 3.02 dB for 2 Vpp swing were obtained at 56 Gb/s and 50 Gb/s the for Ge and GeSi FKE EAM respectively. The signal to noise ratio of the eyes were greater than 5. The demonstration of non-return to zero on-off keying (NRZ-OOK) modulation at 50-56 Gb/s data-rates by Ge based EAM makes this device one of the fastest modulators monolithically integrated on Si.

6.1.4 Modulator performance: Power consumption

The power consumption in a modulator has two main contributions: dynamic power consumption and static power consumption [10]. The dynamic power con-

Figure 6.20: Measured eye diagrams from Ge EAM, at room temperature, at 1610 nm with 1.5 Vpp, 2.0 Vpp and 2.5 Vpp voltage swing and with data rates of 28 Gb/s, 40 Gb/s and 56 Gb/s with input power of 0 dBm before the modulator in the device.

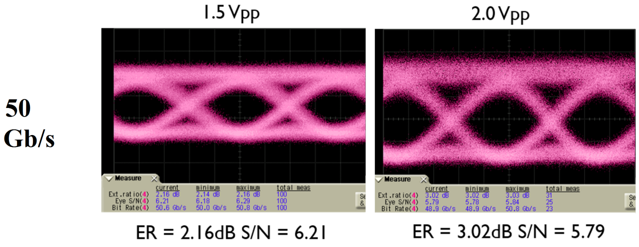

```
             current    minimum    maximum    total meas
Ext.ratio(4) 2.16 dB    2.14 dB    2.16 dB    100
 Eye S/N(4)  6.21       6.18       6.29       100
 Bit Rate(4) 50.6 Gb/s  50.0 Gb/s  50.8 Gb/s  100
```

ER = 2.16dB S/N = 6.21

```
             current    minimum    maximum    total meas
Ext.ratio(4) 3.02 dB    3.02 dB    3.03 dB    31
 Eye S/N(4)  5.79       5.78       5.84       25
 Bit Rate(4) 48.9 Gb/s  48.9 Gb/s  50.8 Gb/s  23
```

ER = 3.02dB S/N = 5.79

Figure 6.21: Measured eye diagrams from GeSi EAM, at room temperature, at 1560 nm with 1.5 Vpp and 2.0 Vpp voltage swing and with data rates of 50 Gb/s with input optical power of 3 dBm before the modulator in the device.

sumption is defined as the power consumed to switch the modulator between the ON and OFF states. The junction capacitance extracted from the S_{11} parameter of the modulator can be used to estimate the average dynamic energy consumption per bit using the formula: 1/4($C_j V_{pp}^2$). With C_j = 12.8 fF at a bias voltage of -1V, the dynamic energy consumption per bit is 12.8 fJ/bit for Vpp=2. This translates to a dynamic power consumption of 0.64 mW for 56 Gb/s of transmission rate. On the other hand, the static power consumption in the EAM originates mostly from the light current and can be estimated as 1/2($P_{in} R_{on} V_{on}$ + $P_{in} R_{off} V_{off}$). With a responsivity of 0.9 A/W at -2V and input optical power of 0 dBm (1mW) in the Si WG before the EAM, the static power consumption is 0.9 mW. As a result, the total power consumption (dynamic and static contributions) is 1.64 mW for 2 Vpp voltage swing. At 56 Gb/s, it translates to 29 fJ/bit. The performance of this modulator is compared to other Si, hybrid Si and Ge(Si) based modulators in Table 6.1.

Modulator Type	ref.	Footprint [μm^2]	Wavelength [nm]	Voltage Swing [V]	Optical Range [nm]	ER [dB]	IL [dB]	Static Power [mW]	Dynamic Power [fJ/bit]	3 dB 3 dB [GHz]	Max. Bit Rate [Gb/s]
Si MZI	[11]	∼2000×500	1300	2.5	>80	3.4	7.1	63.9	750	22	56
Si Ring - Low Q	[11]	∼10×10	1550	1.5	<0.3	6.1	∼8.4	63.3 (with) heaters)	12.8	47	56
III-V on Si	[12]	>100×350	1300	2.2	>30	>10	4.8	6.2	484	74	50
GeSi FK EAM - I	[1]	10×55	1550	3	∼30	6	5	6.7	60	40.7	28
GeSi FK EAM - II	[2, 3, 11] This work	10×40	1560 and 1615	2	∼30	4.6	4.9	1.2	12.8	>50	56
Ge QCSE EAM	[13]	3×90	1445	5	∼20	11	7.5	-	16	23	-

Table 6.1: Benchmarking table comparing the presented Ge modulator with other types of state-of-art Si, III-V and Ge based optical modulators.

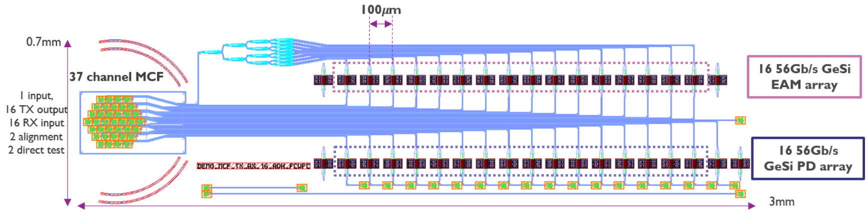

Figure 6.22: layout schematic of 16-channel SDM transceiver with 16-channel GeSi FKE EAM and PD array and 1-to 16 optical power splitter. The whole devuce has a footprint of 2.1 mm^2 [14].

6.1.5 Demonstrators using Ge based FKE EAM

The presented GeSi FKE EAM has a compact footprint, superior electrostatics with low power consumption and high speed making it an attractive device for various demonstrators. The compact footprint of each EAM enable to realize space division multiplexing (SDM) that increases the bandwidth of optical links. SDM using 4 parallel single-mode fibers (PSM-4) has been commonly used for short reach optical links as the cost of fiber is not dominant. On the other hand, wavelength-division multiplexing is intended to reduce fiber cost for medium to long range optical links, but suffers from low link power efficiency if thermal tuning of each individual channel is required to keep all channels aligned to the grid. Therefore, for realizing a SDM transceiver, 61 channel multi-core fiber (MCF) with GeSi FKE EAM were used to demonstrate a 16-channel SDM bidirectional optical transceiver. This transceiver was operating at 896 Gb/s with a overall footprint of 2.1 mm^2 as reported in [14]. Fig. 6.22 shows the layout of the 16-channel SDM transceiver with a 16 GeSi EAM array and an additional 16 GeSi EAM array used as a photodiode. The PDs were 60 μm long and operated at -2 V whereas the EAMs were 40 μm long. Out of the 61 channel 125 μm diameter flexible multicore fiber, 37 channels were used for the 16-channel SDM transceiver demonstrator with the measured eye diagrams at the transmit and receive side as shown in Fig. 6.23 and Fig. 6.24. This demonstration shows the feasibility of realizing aggressive silicon-based SDM transceivers for very short-reach interconnects ($\sim$1m).

Alternatively, 4 lanes of 100 Gb/s non-return-to-zero (NRZ) channels can be used to achieve 400 GbE transceivers. This addresses the needs of data center optical links that result in the evolution of 100 Gb/s Ethernet (100 GbE) to 400 Gb/s Ethernet (400 GbE). GeSi FKE EAM was used in combination with a six-tap analog feedforward equalizer (FFE) on the transmitter IC (TX IC) designed in SiGe BiCMOS technology and reported in [15, 16]. The TX IC generates a pre-emphasized electrical signal to compensate the frequency roll-off and non-

Figure 6.23: 56 Gb/s PRBS eyes diagrams at 1565 nm for 16 channel GeSi EAM, each 40 μm long, and driven with 2.5 Vpp voltage swing [14].

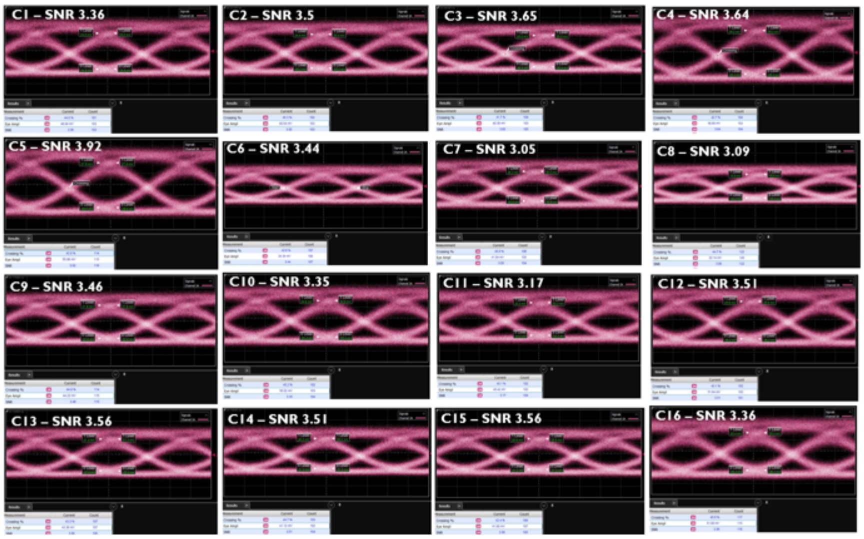

Figure 6.24: 56 Gb/s PRBS eyes diagrams at 1565 nm for 16 channel GeSi PD, each 60 μm long, and operated at -2 V [14].

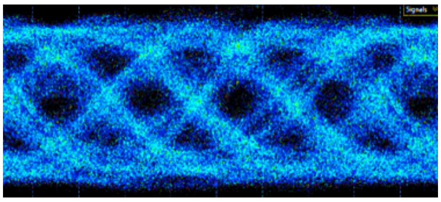

Figure 6.25: Eye diagram for 100 Gb/s NRZ-OOK transmission through GeSi FK EAM to GeSi FK EAM used as a photodetector [15, 16].

idealities of all the components in the optical link in order to generate a pre-emphasized electrical signal. This signal is amplified using an RF amplifier to generate 2 Vpp voltage swings for the optical modulator. An 80 μm long GeSi FK EAM was used as the modulator and a second device was used as the photodetector in an optical link with back-to-back configuration. The eye diagram with 100 Gb/s non-return-to-zero on-off keying modulation is shown in Fig. 6.25. With a received optical power of 8 dBm at the photodetector, the bit error rates of the transmitted data in B2B configuration, as well of 500m of standard single mode fiber and 2 km of dispersion shifted fiber were all below the HD-FEC threshold.

These examples, SDM and 100 Gb/s NRZ-OOK modulation, showcase the capabilities of the Ge based FK EAM as a disruptive device that can be used for realizing compact and low-power optical transceivers for short-reach optical interconnects applications.

6.2 Electro absorption modulator using quantum confined stark effect

One of the drawbacks of the Ge FKE EAM is that the device suffers from high link power penalty ($\sim$9 dB for 2 Vpp swing) due to the low ER/IL ratio. This directly increases the power consumption of the link as it requires the laser to emit higher optical power. Therefore, it is essential to reduce the link power penalty of the modulator without compromising the low power consumption and the footprint of the individual device. This is feasible using a quantum confined stark effect electro-absorption modulator (QCSE EAM) due to the presence of sharp exciton resonances in the absorption spectrum of a multi-quantum well stack. These sharp absorption features allow for an ER/IL ratio as high as 3 for 1 Vpp and thus have the potential to reduce the link power penalty [17]. Ge/SiGe based multi-quantum systems exploiting the quantum confined stark effect have been extensively explored in the Group-IV photonics research community [13, 17–20]. In addition to having high FOM, these devices can also operate at 1.3 μm wavelength with an appropriate stack design [19, 20]. This operation wavelength is of great inter-

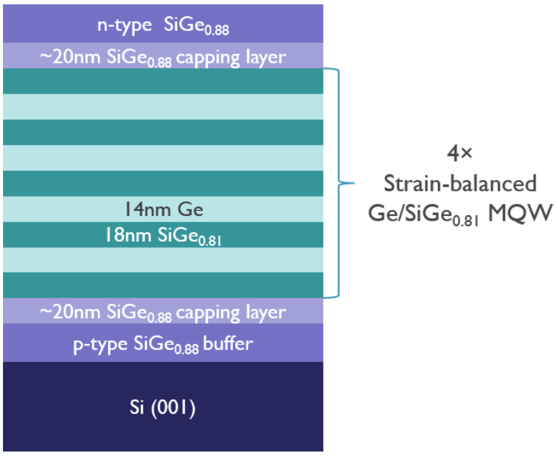

Figure 6.26: Target multi-quantum well stack for operating wavelength of 1425-1475 nm at room temperature [17].

est for the optical interconnect community as the fiber dispersion is zero at this wavelength, allowing the transmission of information at high data-rates without any loss in signal integrity. Therefore, Ge based QCSE EAM has the potential to substantially outperform the static performance of Ge based FKE EAM. With a long term goal of integrating QCSE EAMs in imec's Si photonics platform, in this thesis, we will explore the material and device development of first multi-quantum well based QCSE stacks, similar to the 1425 nm stack presented in [17]. This exercise will demonstrate the potential of such a device and will pave the way for future developments.

6.2.1 Material characterization of Ge based multi-quantum wells

For the initial development of the Ge based QCSE EAM, a target stack as shown in Fig. 6.26 with operating wavelength of 1425-1475 nm was similar to the stacks presented in [17]. This structure is based on an epitaxy strategy that results in a minimum strain build-up through the entire stack and uses thin buffer layers. In the stack, $Si_{0.12}Ge_{0.88}$ is used as the buffer layer. Throughout the entire stack, the in-plane lattice constant must be constant so that no defects can be generated. Therefore, in order to maintain the strain balance in the multi-quantum well system, 14 nm thick Ge quantum wells were sandwiched between 18 nm of $Si_{0.19}Ge_{0.81}$ barrier layers. The underlying buffer layer and the top layer of the stack, used as the contact, must be of the same material composition and doped so that an electric field can be applied between these layers across the multi-quantum well region.

The buffer layer was grown at 500°C using GeH_4 and dichlorosilane as the precursors in a reduced pressure chemical vapour deposition (ASM-Intrepid XP^{TM})

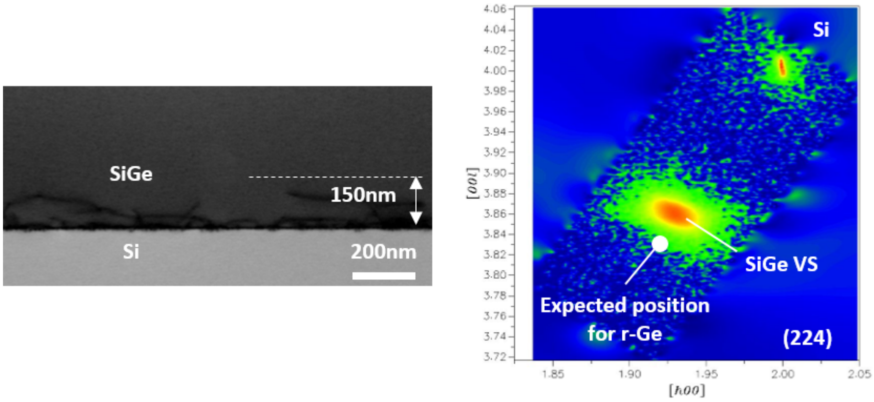

Figure 6.27: Cross-sectional TEM image and RSM image of the buffer layer in Fig. 6.26.

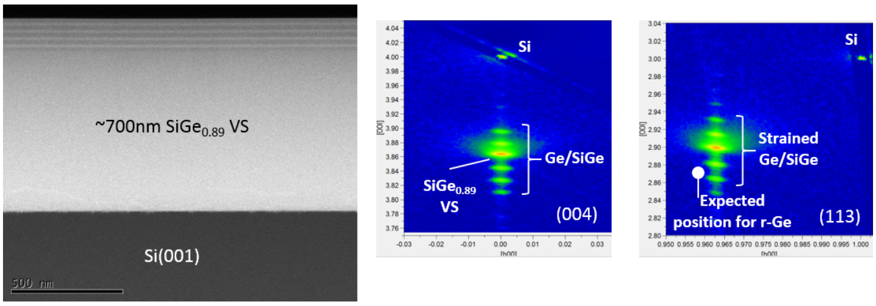

Figure 6.28: Cross-sectional TEM image and RSM image of the multi-quantum well stack shown in Fig. 6.26.

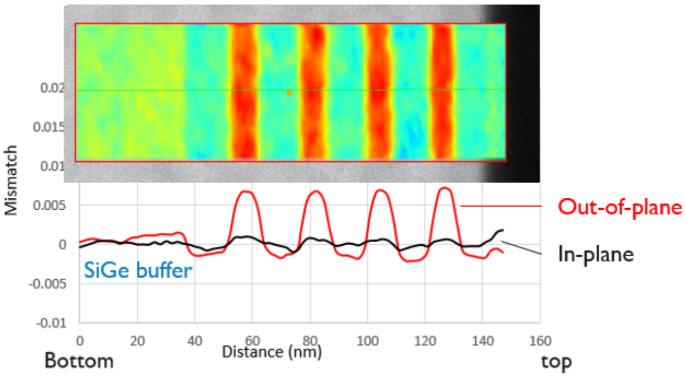

Figure 6.29: Distribution of strain in the multi-quantum well region evaluated using a nano-beam diffraction technique.

epi tool. The buffer layer had a thickness of 1 μm and was grown on a Si substrate. The growth was followed by a post-epi anneal in N_2 at 850°C for 3 minutes in order to reduce the threading dislocation density arising from the misfits at the Si/SiGe interface. The buffer layers were then thinned down to a target thickness of 0.6 μm and 0.2 μm with the removal of 0.4 μm and 0.8 μm of SiGe using chemical mechanical polishing respectively. Characterization using X-ray Diffraction (XRD), reciprocal space mapping (RSM) and Rutherfold Back Scattering (RBS) confirmed that the buffer layers with target thickness of 0.2 μm, 0.6 μm and 1.0 μm were fully relaxed and had 11$\%$ of Si content in these layers. TEM analysis also revealed that the majority of the defects were confined in the bottom 150 nm of the buffer layer as seen in Fig. 6.27. Obtaining such fully relaxed high quality buffer layers was possible due to the high temperature growth at 500°C. The multi-quantum well section of the stack was then grown on the 0.2 μm or 0.6 μm thick buffer layer at 350°C using Ge_2H_6 and Si_2H_6 as precursors. These layers were fully strained as seen from the RSM and were also defect free within the measurement window shown in Fig. 6.28. Smooth surfaces with RMS roughness of $<$1 nm were measured using atomic force microscopy. In addition to this, sharp transitions with no or very limited inter diffusion of Si content between the quantum and barrier layers were obtained, as verified by EDS mapping across the stack. This was possible due to the use of high order precursors and a low growth temperature (350°C) for the multi-quantum well region. The latter results in minimal atomic diffusion between the quantum well and barrier region. To confirm the presence of quantization in the quantum well, absorption measurements were measured on these thin films using a free space spectrophotometer and is shown in Fig. 6.30. At wavelength around 1425 nm, there is a sharp transition in the absorption that corresponds to the exciton resonance associated absorption feature in these stacks. The presence of this exciton resonance also confirms strong quantum confinement in the Ge QWs due to high content of Si in the barriers that prevents the coupling of a QW wavefunction with an adjacent QW. Moreover, the profile of absorption spectrum for wavelengths below 1410-1420 nm is visibly flat and constant confirming the box like behaviour of the density of states above the band gap of the quantum well region, contrary to the quadratic behaviour of density of states and absorption spectrum observed above the band gap of bulk materials.

6.2.2 Demonstration of quantum confined stark effect

The absorption measurement shown in Fig. 6.30 confirms the presence of the exciton resonance and quantization in the multi-quantum well stack. To demonstrate the quantum confined stark effect based electro absorption, p-i-n diodes were fabricated with the multi-quantum region in the intrinsic region of the diode such that a change in applied bias will change the electric field in the intrinsic region and

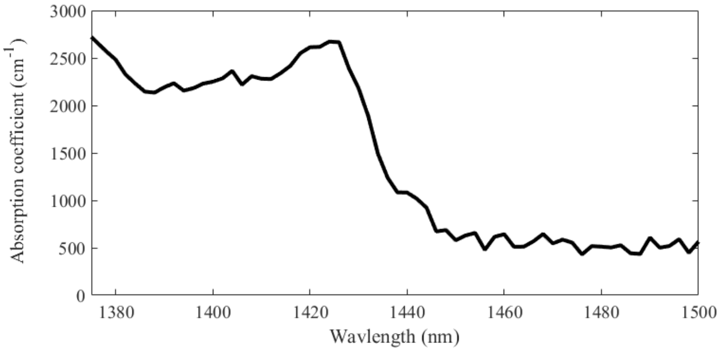

Figure 6.30: Absorption spectrum of the stack with target operation wavelength of 1425 nm, shown in Fig. 6.26 and Fig. 6.28. The sharp exciton absorption peak at 1425 nm confirms the presence of quantization in the Ge wells.

hence modulate the absorption coefficient of the quantum wells. The device geometry used for this demonstration is shown in Fig. 6.31. In this case 200 and 600 nm of $Si_{0.11}Ge_{0.89}$ buffer were grown on ion-implanted Si that forms the p contact of the diode with an active doping level of $\sim 3\times 10^{18}$ cm^{-3}. These layers are obtained by 1× or 2× 0.4 μm CMP of a 1 μm thick undoped $Si_{0.11}Ge_{0.89}$ buffer. After the deposition of the multi-quantum well stacks on these buffer layers, 20 nm of undoped $Si_{0.11}Ge_{0.89}$ was grown before the n-type doped $Si_{0.11}Ge_{0.89}$ in order to avoid dopant diffusion into the underlying quantum wells. The top region was doped in-situ with Arsenic (As), reaching an active doping level of 1×10^{19} cm^{-3}.

The QCSE related shift in absorption can be measured by monitoring the change in photocurrent of the diode as a function of applied bias. To facilitate this measurement, diodes were fabricated by vertically dry etching circular structures through the Ge/SiGe MQW stack down to the Si substrate. The devices are electrically isolated due to the presence of SiO_2 around the Ge/SiGe MQW Mesas. Ti/Pt/Au contacts with a circular opening at the center of the device were then defined by electron beam evaporation and a lift-off process. These devices were vertically illuminated using a tunable laser and a cleaved fiber. Since the tunable laser could measure from 1440-1640 nm wavelength, the devices were heated up to 75°C so that the room temperature exciton resonance at 1425 nm shifts to 1460 nm. The measured photocurrent response for stacks with 200 nm thick undoped buffer and 600 nm thick undoped buffer is shown in Fig. 6.33 and Fig. 6.34. The photocurrent response was extracted by substrating the dark current from the light current, even though the dark current was lower by 2 orders of magnitude. At 0 V bias and operating temperature of 75°C, the peak photocurrent for both stacks was in the range of 1450-1460 nm. At room temperature, the measured spec-

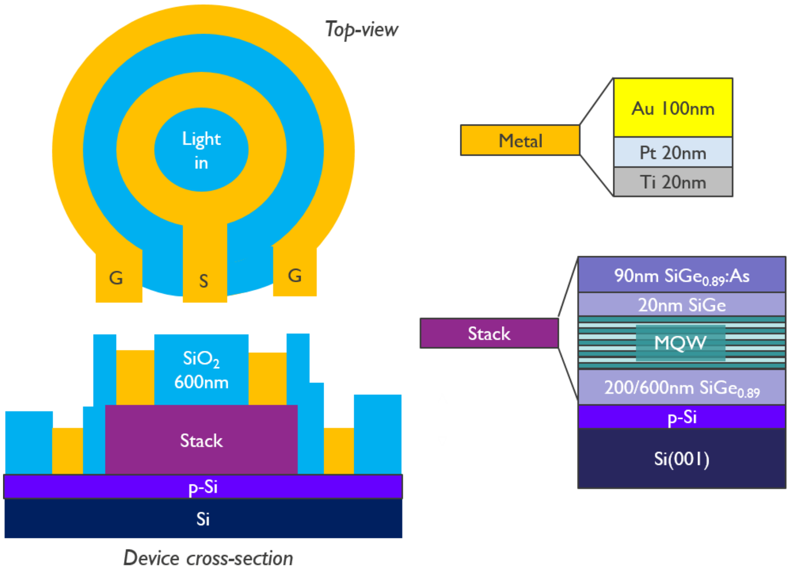

Figure 6.31: Schematic of the device geometry used for the demonstration of the quantum confined stark effect using a photocurrent measurement. The multi-quantumwell section of the stack can be seen in Fig. 6.26.

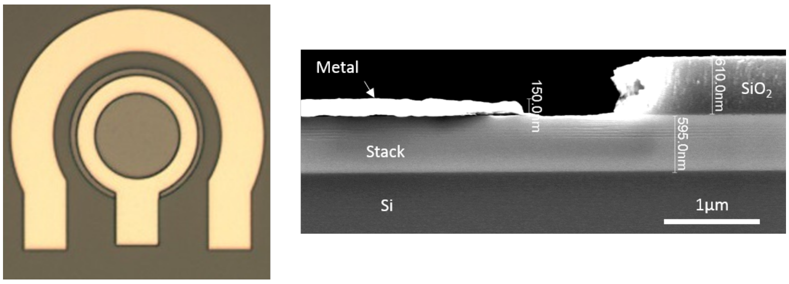

Figure 6.32: Microscope image and scanning electron micrograph of a fabricated device. The quantum well layers can be seen in the SEM image along with the 200 nm thick buffer layer, the oxide for electrical isolation and the metal contact layers.

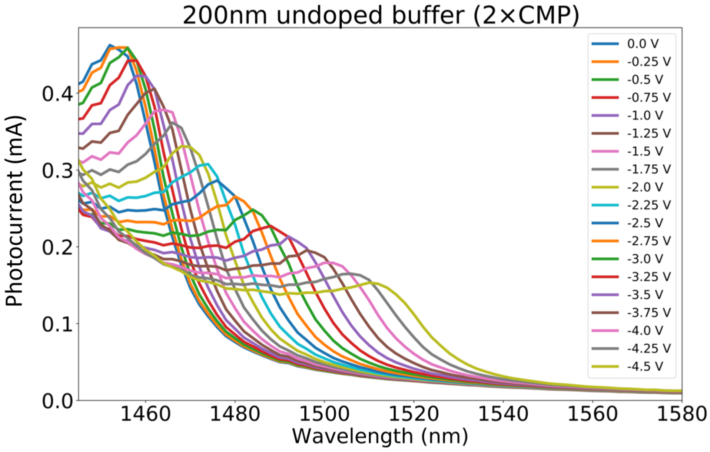

Figure 6.33: Measured photocurrent from vertically illuminated multi-quantum well stack with device schematic shown in Fig. 6.31. Quantum wells were grown on 200 nm thick buffer layer. These measurements were performed at 75° C.

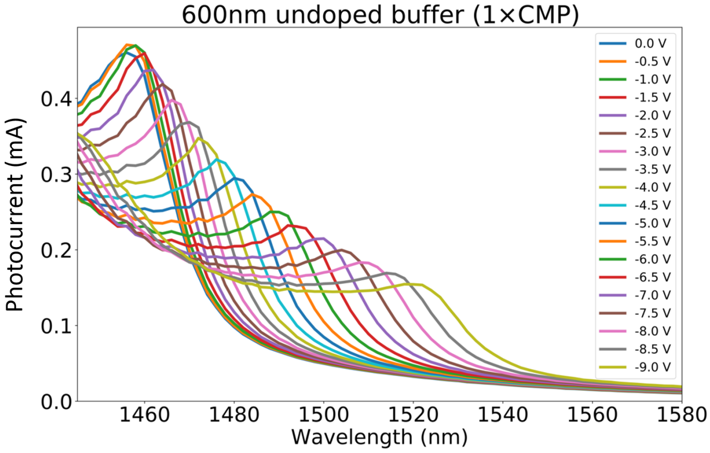

Figure 6.34: Measured photocurrent from vertically illuminated multi-quantum well stack with device schematic shown in Fig. 6.31. Quantum wells were grown on 600 nm thick buffer layer. These measurements were performed at 75° C.

trum blue-shifts by $\sim$38 nm and matches the absorption spectrum shown in Fig. 6.30. When the reverse DC bias was increased in the diode, the electric field in the MQW region also increased resulting in a red shift of the absorption spectrum. Moreover, the exciton absorption peak intensity drops with increase in applied bias due to the decrease in overlap of the electron and hole wave functions as can be seen in Fig. 2.10. For a fixed voltage swing, say from 0-1 V or 1 Vpp, the E-field difference for the MQW stack with 200 nm and 600 nm of undoped buffer was estimated to be 21.4 kV/cm and 11.5 kV/cm. Therefore, the voltage swing applied over the diode does not efficiently translate to high electric fields. If these stacks were grown on doped buffers, then 1 Vpp would result in 42.4 kV/cm electric field. When Ge based FKE EAM is operated with 2 Vpp swing, the electric field difference obtained from a 0.6 μm wide WG was $\sim$46 kV/cm. This is comparable to 4 Vpp and 2 Vpp swing applied to the QCSE stacks with 600 nm and 200 nm of undoped buffer respectively. Therefore, 1 Vpp for the 200 nm buffer MQW stack corresponds to 1 Vpp in the Ge based FKE EAM and 1 Vpp for the 600 nm buffer MQW stack corresponds to 0.5 Vpp in the Ge based FKE EAM. The figure of merit (FOM=$\Delta\alpha/\alpha$) for 1 Vpp was extracted from these photocurrent responses for both the 200 nm and 600 nm undoped buffer stack as shown in Fig. 6.35 and Fig. 6.36. Due to the presence of sharp exciton resonances, a FOM of up to 1.75 was observed in the 200 nm undoped buffer stacks which is $>2\times$ better than observed for the Ge based FKE EAM with 1 Vpp. If these MQW stacks had a doped buffer, then we could extrapolate that the FOM for 1 Vpp in these doped buffer stacks would be $\sim4\times$ improved as compared to the Ge based FKE EAM. Such an improved static performance of these QCSE stacks can significantly reduce the link power penalty of the modulator and also reduce the operating voltage swing to 1 Volt, compatible with CMOS drivers. In addition, these devices can be adapted to operate within the O-band around 1310 nm with appropriate tuning of the stack. This shows that they could replace the Ge based FKE EAM in future optical links [19, 20].

6.2.3 Future work

In the previous section, we saw that Ge based quantum confined stark effect EAMs can reduce the link power penalty compared to Ge based FKE EAM. However, the conclusions were based on the demonstration of a simple stack operating at 1460-1520 nm at 75°C (1425-1485 nm at room temperature) with room for further development as listed below:

- Repeat photocurrent measurement with doped buffers - to increase the electric field for a given applied voltage.

- Integrate the device into imec's Si photonics platform and evaluate the FOM with Si WG integrated absorption measurements.

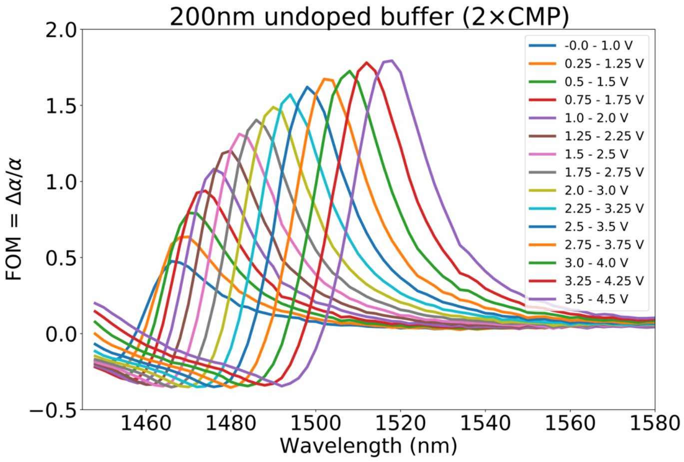

Figure 6.35: Figure of merit (FOM=$\Delta\alpha/\alpha$) extracted from Fig. 6.33. The diodes were operated in reverse bias.

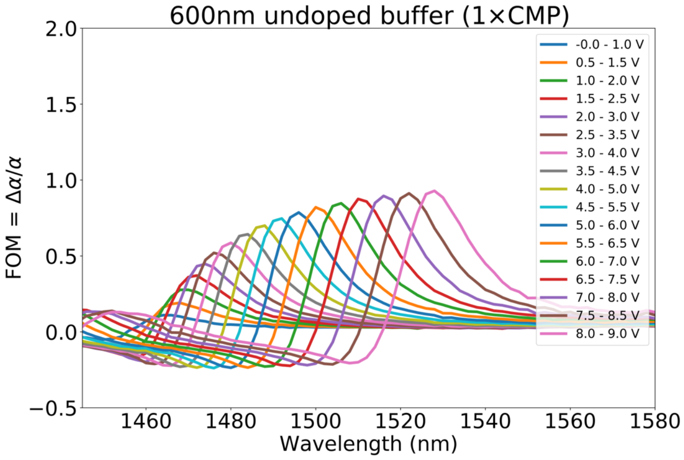

Figure 6.36: Figure of merit (FOM=$\Delta\alpha/\alpha$) extracted from Fig. 6.34. The diodes were operated in reverse bias.

- Optimize doping levels for >50 GHz operation.

6.3 Summary

In this chapter, we presented Ge based Franz-Keldysh effect electro absorption modulators operating at 1615 nm or at 1560 nm, depending on the active medium in the modulator. For 2 Vpp (from 0 to -2V), an extinction ratio of 4.6 dB and an insertion loss of 4.9 dB were measured. These devices have a compact footprint, low power consumption and can be operated at data-rates of >50 Gbps. This enabled the demonstration of a space division multiplexed transceiver at a data rate of 896 Gb/s through 16 physical channels. On the other hand, a single channel optical link transmitting at data rates of 100 Gb/s from Ge based FKE EAM to Ge based FKE EAM operated as a photodiode was also shown. However, this is possible only if the tranmitted electric signal is pre-emphazied in order to compensate for frequency roll-off and non-idealities in the optical link. It is important to note that these FKE EAMs suffer from a high link power penalty (9 dB for 2 Vpp swing), which reduces the link efficiency. However, the multi-quantum well based quantum confined stark effect that exploits the exciton resonance associated absorption peaks can improve the figure of merit (FOM) of the EAM by a factor >4× with respect to the FKE EAM. In addition to this, the operating wavelength of the device can be tuned to the O-band. Initial demonstrations in this thesis of a Ge based MQW QCSE EAM are promising and pave the way towards replacing the FKE EAM.

References

[1] Dazeng Feng, Wei Qian, Hong Liang, Cheng-Chih Kung, Zhou Zhou, Zhi Li, Jacob S Levy, Roshanak Shafiiha, Joan Fong, B Jonathan Luff, et al. *High-speed GeSi electroabsorption modulator on the SOI waveguide platform*. IEEE Journal of Selected Topics in Quantum Electronics, 19(6):64–73, 2013.

[2] Srinivasan Ashwyn Srinivasan, Marianna Pantouvaki, Shashank Gupta, Hong Tao Chen, Peter Verheyen, Guy Lepage, Gunther Roelkens, Krishna Saraswat, Dries Van Thourhout, Philippe Absil, et al. *56 Gb/s germanium waveguide electro-absorption modulator*. Journal of Lightwave Technology, 34(2):419–424, 2016.

[3] SA Srinivasan, Peter Verheyen, Roger Loo, Ingrid De Wolf, Marianna Pantouvaki, Guy Lepage, Sadhishkumar Balakrishnan, Wendy Vanherle, Philippe Absil, and Joris Van Campenhout. *50Gb/s C-band GeSi waveguide*

electro-absorption modulator. In Optical Fiber Communications Conference and Exhibition (OFC), 2016, pages 1–3. IEEE, 2016.

[4] Shun Lien Chuang. *Physics of photonic devices*, volume 80. John Wiley & Sons, 2012.

[5] L Alloatti, SA Srinivasan, JS Orcutt, and RJ Ram. *Waveguide-coupled detector in zero-change complementary metal–oxide–semiconductor*. Applied Physics Letters, 107(4):041104, 2015.

[6] RK Schaevitz, DS Ly-Gagnon, JE Roth, EH Edwards, and DAB Miller. *Indirect absorption in germanium quantum wells*. AIP Advances, 1(3):032164, 2011.

[7] Philippe P Absil, Peter Verheyen, Peter De Heyn, Marianna Pantouvaki, Guy Lepage, Jeroen De Coster, and Joris Van Campenhout. *Silicon photonics integrated circuits: a manufacturing platform for high density, low power optical I/Os*. Optics express, 23(7):9369–9378, 2015.

[8] Yatendra Pal Varshni. *Temperature dependence of the energy gap in semiconductors*. physica, 34(1):149–154, 1967.

[9] JF Lampin, L Desplanque, and F Mollot. *Detection of picosecond electrical pulses using the intrinsic Franz–Keldysh effect*. Applied Physics Letters, 78(26):4103–4105, 2001.

[10] David AB Miller. *Energy consumption in optical modulators for interconnects*. Optics express, 20(102):A293–A308, 2012.

[11] M Pantouvaki, SA Srinivasan, Y Ban, P De Heyn, P Verheyen, G Lepage, H Chen, J De Coster, N Golshani, S Balakrishnan, et al. *Active Components for 50 Gb/s NRZ-OOK Optical Interconnects in a Silicon Photonics Platform*. Journal of Lightwave Technology, 35(4):631–638, 2017.

[12] Yongbo Tang, Jonathan D Peters, and John E Bowers. *Over 67 GHz bandwidth hybrid silicon electroabsorption modulator with asymmetric segmented electrode for 1.3 μm transmission*. Optics Express, 20(10):11529–11535, 2012.

[13] Papichaya Chaisakul, Delphine Marris-Morini, Mohamed-Said Rouifed, Jacopo Frigerio, Daniel Chrastina, Jean-René Coudevylle, Xavier Le Roux, Samson Edmond, Giovanni Isella, and Laurent Vivien. *Recent progress in GeSi electro-absorption modulators*. Science and technology of advanced materials, 15(1):014601, 2013.

[14] Peter De Heyn, Victor I Kopp, SA Srinivasan, Peter Verheyen, J Park, MS Wlodawski, J Singer, D Neugroschl, B Snyder, S Balakrishnan, et al. *Ultra-dense 16× 56Gb/s NRZ GeSi EAM-PD arrays coupled to multicore fiber for short-reach 896Gb/s optical links*. In Optical Fiber Communications Conference and Exhibition (OFC), 2017, pages 1–3. IEEE, 2017.

[15] Jochem Verbist, Michiel Verplaetse, SA Srivinasan, Peter De Heyn, Timothy De Keulenaer, Ramses Pierco, Renato Vaernewyck, Arno Vyncke, Philippe Absil, Guy Torfs, et al. *First real-time 100-Gb/s NRZ-OOK transmission over 2 km with a silicon photonic electro-absorption modulator*. In Optical Fiber Communications Conference and Exhibition (OFC), 2017, pages 1–3. IEEE, 2017.

[16] Jochem Verbist, Michiel Verplaetse, Srinivasan Ashwyn Srinivasan, Joris Van Kerrebrouck, Peter De Heyn, Philippe Absil, Timothy De Keulenaer, Ramses Pierco, Arno Vyncke, Guy Torfs, et al. *Real-Time 100 Gb/s NRZ and EDB Transmission with a GeSi Electro-Absorption Modulator for Short-Reach Optical Interconnects*. Journal of Lightwave Technology, 2017.

[17] Elizabeth H Edwards, Leon Lever, Edward T Fei, Theodore I Kamins, Zoran Ikonic, James S Harris, Robert W Kelsall, and David AB Miller. *Low-voltage broad-band electroabsorption from thin Ge/SiGe quantum wells epitaxially grown on silicon*. Optics express, 21(1):867–876, 2013.

[18] Yu-Hsuan Kuo, Yong Kyu Lee, Yangsi Ge, Shen Ren, Jonathan E Roth, Theodore I Kamins, David AB Miller, and James S Harris. *Strong quantum-confined Stark effect in germanium quantum-well structures on silicon*. Nature, 437(7063):1334–1336, 2005.

[19] Mohamed Said Rouifed, Papichaya Chaisakul, Delphine Marris-Morini, Jacopo Frigerio, Giovanni Isella, Daniel Chrastina, Samson Edmond, Xavier Le Roux, Jean-René Coudevylle, and Laurent Vivien. *Quantum-confined Stark effect at 1.3 μm in Ge/Si 0.35 Ge 0.65 quantum-well structure*. Optics letters, 37(19):3960–3962, 2012.

[20] Mohamed-Said Rouifed, Delphine Marris-Morini, Papichaya Chaisakul, Jacopo Frigerio, Giovanni Isella, Daniel Chrastina, Samson Edmond, Xavier Le Roux, Jean-Rene Coudevylle, David Bouville, et al. *Advances toward Ge/SiGe quantum-well waveguide modulators at 1.3 μm*. IEEE Journal of Selected Topics in Quantum Electronics, 20(4):33–39, 2014.

7
Conclusion

Optical interconnects realized on silicon photonics platforms have been identified as a suitable candidate to replace the electrical counterpart and tackle the bandwidth versus power consumption bottleneck in short reach interconnect applications such as intra data center communication. Within such an optical transceiver, various components such multiplexers/demultiplexers, filters, grating couplers and electro optic modulators have been realized using Si as the main active material. However, III-V semiconductors have been the conventional choice of material for electro absorption modulators and laser sources due to the direct band gap behaviour of these materials. Their integration into existing Si photonics platform have a few challenges such as processing complexity, processing cost, lack of scalability and/or difficulty in coupling light between the III-V device and the SOI wafer. Ge on the other hand has been considered as an alternative solution to III-V materials, therefore, in this thesis we validated the performance of Ge based devices such as laser sources and electro absorption modulators for future optical interconnects.

7.1 Ge laser on Si

Germanium is intrinsically an indirect bandgap material. Nevertheless, it can become an efficient light source when is converted to a pseudo direct band gap or direct band gap material via 1) the introduction of uniaxial/biaxial tensile strain, 2) doping with n-type dopants and/or 3) alloying with Sn. For optical interconnect applications and compatibility with commercially available standard single mode fibers, a highly n-type doped Ge based approach was identified as the most appropriate route to fabricate an electrically pumped laser emitting at wavelength <1700 nm and an initial threshold current density of 10 kA/cm^2. These specifications are a 30-fold improvement from previously demonstrated electrically pumped Ge laser, but is higher than state of the art III-V laser. Such a Ge laser can be feasible if the active medium is doped with P-atoms up to a doping level of 1×10^{20} cm^{-3} and has a Shockley Read Hall recombination mediated carrier lifetime $>$ 10 ns. In this thesis, we investigated these requirements by studying the carrier lifetime in Ge based material systems, understanding the impact of P-atoms on pseudo direct band gap behaviour of Ge and by performing absorption spectroscopy to quantify the gain coefficient that can be extracted from P-doped Ge.

Undoped Ge films on Si material systems were first investigated to understand the carrier lifetime dynamics in Ge. For this purpose, pump-probe spectroscopy on Ge-on-Si WGs of varying thickness and widths integrated in imec's Si photonics platform was performed. These measurements allow to extract carrier lifetime in these WGs and a dependence on the cross-sectional dimensions of the WG was observed. For a 1 μm wide $\times$ 0.375 μm thick Ge WG, a carrier lifetime of 1.15 ns was extracted. This result is one order of magnitude more than the targeted 10 ns as it was limited by the Ge/Si and Ge/SiO$_2$ interface. The very poor Ge/SiO$_2$ interface was improved by exploring various schemes that use Si or GeO$_x$. For a 0.6 μm thick undoped Ge layer on Si, the longest carrier lifetime that could be extracted was 4.3 ns, where the defects at the Ge/Si interface were dominant. Therefore, a carrier lifetime of $>$ 10 ns in doped Ge layers is far from reality.

In parallel, material development for highly n-type doped Ge layers were initiated on 1 μm thick Ge virtual substrates grown on 300 mm Si wafer (001). The doping mechanism was based on in-situ doping with Phosphorus as the dopant due to its high solubility limit in Ge. The epitaxy was done using a Chemical Vapour Deposition reactor with PH$_3$ and Ge$_2$H$_6$ as the precursor at 320°C. P atoms up to a concentration of 4×10^{20} cm^{-3} were incorporated in Ge, but the surface roughness increased dramatically when the concentration exceeded 7×10^{19} cm^{-3}. As a result, a maximum active P concentration of 6.2×10^{19} cm^{-3} was observed without any annealing step. Photoluminescence spectroscopy (PL) measurements showed that the intensity of light emitted from doped layers was linked to the active P concentration and degree of activation. As the doping level increased (with full activation) the PL intensity also increased. However, as the degree of activation decreased, the PL intensity dropped due to increased point defects. Rapid thermal annealing helped in reducing the amount of such point defects and thus increase the PL intensity. However, the highest active doping level that could be measured was around 5×10^{19} cm^{-3}.

Once the epitaxy study was thoroughly investigated, P-doped Ge layers with a doping level up to 5.35×10^{19} cm^{-3} were grown on Si. In these layers, P-atoms were uniformly distributed P-atoms across the entire Ge stack. For all doped Ge layers, including those grown on 1 μm thick Ge virtual substrates, the full width at half maximum of the PL spectra were significantly larger than for undoped Ge. This arises due to carrier scattering induced linewidth broadening effects in Ge due to ionized P dopants. Such ionized P atoms are responsible for carrier scattering that broadens the recombination and absorption/gain spectrum of the material. The presence of these linewidth broadening effects was further verified by performing transient absorption spectroscopy. Here, the optical bleaching spectra from all doped layers were broadened and suppressed. The extent of this broadening was quantified by fitting both the PL spectrum and the optical bleaching effect spectrum with a modified joint density of states. A broadening parameter $\Gamma_{\text{opt}} \geq 45$ meV for doped Ge and Γ_{opt} = 8 meV for undoped Ge were extracted. Such high broadening effects exists and reduce the pumping/injection efficiency to reach transparency and gain by a factor > 4. Additionally, the carrier lifetime dropped from 3 ns in undoped Ge (also unpassivated) to <0.3 ns in P-doped Ge. Here the lifetime is not limited by the Ge/Si interface, but by the presence of point defects due to dopants. All these experiments reveal that even though P dopants are necessary to make Ge an efficient light source, they introduce detrimental scattering effects that can significantly increase the threshold current density by a factor >40. Under such conditions, achieving a laser with sub 10 kA/cm^2 is practically extremely difficult. As a result, P-doped Ge cannot be seen as a potential gain material for optical interconnect applications where power consumption is a stringent criteria.

7.2 Ge based electro absorption modulator

The direct band gap of undoped and unstrained Ge is located 0.8 eV which corresponds to 1550 nm wavelength. The presence of this band gap makes Ge an interesting material to realize an electro absorption modulator for optical interconnect applications with strict channel scaling requirements due its attractive properties such as compact footprint and high bandwidth. As a result, Ge-on-Si or $\text{Ge}_{0.992}\text{Si}_{0.008}$-on-Si material enabled Franz-Keldysh effect electro absorption modulators operating at 1615 nm and 1560 nm respectively. These modulators are 0.6 μm wide, 0.375 μm thick and 40 μm long with a p-i-n diode designed in lateral configuration. An extinction ratio of 4.2 dB and 4.9 dB for 2 Vpp swing and an insertion loss of 4.4 dB and 5.8 dB (with FOM <1 for 2 Vpp swing) were extracted from GeSi and Ge FKE EAM respectively. This resulted in a link power penalty of 9 dB. However, due to its compact geometry and optimized doping profile, 1 dB bandwidth of these devices were >50 GHz that enabled NRZ-OOK modulation at 56 Gbps with dynamic power consumption of 12.8 fJ/bit and static power consumption of 1.2 mW. These performances makes this device one of the fastest modulator monolithically integrated on Si.

The 9 dB link power penalty in Ge based FKE EAM is actually 6 dB higher than that of an ideal modulator. This difference can be reduced by using Ge based multi-quantum well (MQW) quantum confined stark effect (QCSE) electro absorption modulator (EAM). Such a modulator exploits the exciton resonance feature in the absorption spectra and modulates the wavelength location of this resonance with applied bias using the stark effect. Exploiting such a phenomenon a 1425 nm MQW stack with FOM = 1.75 for 1 Vpp swing was demonstrated using photocurrent based absorption measurements. These initial results are very promising as the FOM in such a stack is 3× larger than Ge based FKE EAM and has the potential to drop the link power penalty of the individual device. Moreover, the device can be made to operate at a wavelength of 1310 nm with appropriate stack tuning so that it can used for intra data center optical links, where silicon photonics based optical transceivers have the highest impact. In order to realize such devices, the following developments must be considered for future work:

- Repeat photocurrent measurement with doped buffers - to increase the electric field for a given applied voltage.
- Integrate the device into imec's silicon photonics platform and evaluate the FOM with Si WG integrated absorption measurements.
- Optimize doping levels for >50 GHz operation.